



UNIVERSITÄT  
DES  
SAARLANDES

## **Oxide formation on pure titanium by laser interference patterning to achieve photocatalytic properties**

**Proyecto final para optar al grado de Ingeniero en Materiales por**

**Francisco Cortés**

DNI 40831418

N° Legajo 11979

Email: [ing.cortes.francisco@gmail.com](mailto:ing.cortes.francisco@gmail.com)

Mar del Plata, 16 de agosto de 2022

Director: Dra. Silvia Simison  
Co-Director: M.Sc. Tobias Fox



RINFI se desarrolla en forma conjunta entre el INTEMA y la Biblioteca de la Facultad de Ingeniería de la Universidad Nacional de Mar del Plata.

Tiene como objetivo recopilar, organizar, gestionar, difundir y preservar documentos digitales en Ingeniería, Ciencia y Tecnología de Materiales y Ciencias Afines.

A través del Acceso Abierto, se pretende aumentar la visibilidad y el impacto de los resultados de la investigación, asumiendo las políticas y cumpliendo con los protocolos y estándares internacionales para la interoperabilidad entre repositorios



Esta obra está bajo una [Licencia Creative Commons Atribución-  
NoComercial-CompartirIgual 4.0 Internacional](https://creativecommons.org/licenses/by-nc-sa/4.0/).



UNIVERSITÄT  
DES  
SAARLANDES

## **Oxide formation on pure titanium by laser interference patterning to achieve photocatalytic properties**

**Proyecto final para optar al grado de Ingeniero en Materiales por**

**Francisco Cortés**

DNI 40831418

N° Legajo 11979

Email: [ing.cortes.francisco@gmail.com](mailto:ing.cortes.francisco@gmail.com)

Mar del Plata, 16 de agosto de 2022

Director: Dra. Silvia Simison  
Co-Director: M.Sc. Tobias Fox

## Acknowledgments

There are many people who were part of this project and maybe not all of them will be mentioned here, but I will always be thankful to everyone who helped me and supported me during the course of this work. This thesis would have not been possible without them.

In the first place, I want to thank Prof. Frank Mücklich for giving me the opportunity to develop this research work at his Institute of Functional Materials at the Saarland University and thereby providing the scientific equipment and environment necessary to complete this work.

Especially greetings to the IDEAR exchange program founded by CUA-DAHZ, supported by DAAD, and the coordinators of the program Dra. Silvia Simison and Dr. Flavio Soldera. Their dedication and perseverance give the possibility to many students to study abroad and develop their professional careers. I also want to thank the whole team of EUSMAT for the organization of the different exchange programs and their support to all students.

This thesis would not have been possible without the appreciated feedback and guidance of my supervisor Tobias Fox and I am grateful for all the hours he spent guiding and helping me, transmitting to me the knowledge and passion for this field of research.

I am grateful to all the staff of the Chair of Functional Materials for the constant support and help while using the equipment necessary for this project, especially to Dr. Christoph Pauly and Lucía Campo for SEM/FIB measurements, Michael Kasper for the support at CLSM and Sebastian Slawik for the support and help with XRD measurements.

Finally, all my gratitude goes to my family, my friends and my girlfriend, who always supported me and gave words of encouragement, regardless of the distance. They all make this experience memorable and they are responsible for this important step in my life.

## Abstract

Materials with photocatalytic properties are used for different applications, especially in the fields of power generation, environmental sanitation and biomaterials. Photocatalytic active materials present an important advantage due to their high capacity for generating complex chemical reactions without the need for large reactors, without the use of chemical agents and using simple configurations or set-ups. One of the most interesting materials used in this field is titanium dioxide (TiO<sub>2</sub>). It shows excellent photocatalytic activity, anti-reflection, self-cleaning ability, can produce hydrophilicity, possesses long-term chemical stability and high photo-reactivity, along with lower toxicity and costs than other semiconductors.

Many techniques are used for surface laser treatment of materials, where different advantages and disadvantages can be found for each technique. The requirement of fast, precise and efficient methods for surface modification motivates the search of new and improved laser technologies to fulfill the needs in this field. The variation of processing parameters of laser treatment can produce changes in the chemistry, topography and morphology of the material surface, and great improvements in properties and new applications can be developed, such as tribology, wetting, hardness, reactivity, chemical compatibility, etc. The use of laser pulses with an ultra-short pulse duration ( $10^{-12}$  to  $10^{-14}$  s) can produce laser ablation and chemical transformation of the surface, with minimal damage or modification of the sample bulk.

In this work, patterned titanium samples were studied with the aim of achieving surface oxidation and thereby, photocatalytic activity of the samples. The use of ultra-short pulses, in combination with direct laser interference patterning (DLIP), can generate periodic surface structures with controlled oxidation of the surface and slightly modification of the bulk properties. A picosecond laser was used for patterning pure titanium samples with DLIP technology and oxidized samples with 10  $\mu\text{m}$  periodicity pattern were produced. The variation of the laser processing parameters was correlated with the resulting chemical, topographic and morphological properties. Different structures were produced (line-like patterns and cross-like patterns) and the accumulated fluence (from 100 to 1000 J/cm<sup>2</sup>) and the number of pulses per point (from 330 to 7000) was varied for different samples to study their influence. The correlation between surface topography, chemistry and photocatalytic activity was discussed and compared with previous work.

## Resumen

Los materiales con propiedades fotocatalíticas se utilizan para diferentes aplicaciones, especialmente en los campos de la generación de energía, el saneamiento ambiental y los biomateriales. Los materiales con actividad fotocatalítica presentan una importante ventaja debido a su alta capacidad para generar reacciones químicas complejas sin necesidad de grandes reactores, sin el uso de agentes químicos y utilizando configuraciones o configuraciones simples. Uno de los materiales más interesantes utilizados en este campo es el dióxido de titanio ( $\text{TiO}_2$ ). Muestra una excelente actividad fotocatalítica, antirreflectante, capacidad de autolimpieza, puede producir hidrofiliidad, posee estabilidad química a largo plazo y alta fotorreactividad, junto con menor toxicidad y costos que otros semiconductores.

Se utilizan muchas técnicas para el tratamiento con láser superficial de materiales, donde se pueden encontrar diferentes ventajas y desventajas para cada técnica. El requisito de métodos rápidos, precisos y eficientes para la modificación de superficies motiva la búsqueda de tecnologías láser nuevas y mejoradas para satisfacer las necesidades en este campo. La variación de los parámetros de procesamiento del tratamiento con láser puede producir cambios en la química, topografía y morfología de la superficie del material, y se pueden desarrollar grandes mejoras en las propiedades y nuevas aplicaciones, como la tribología, la humectación, la dureza, la reactividad, la compatibilidad química, etc. El uso de pulsos láser con una duración de pulso ultracorta ( $10^{-12}$  a  $10^{-14}$  s) puede producir ablación láser y transformación química de la superficie, con un daño o modificación mínimo del bulk de la muestra.

En este trabajo se estudiaron muestras de titanio tratadas con láser con el objetivo de conseguir oxidación superficial y, por tanto, actividad fotocatalítica en las muestras. El uso de pulsos ultracortos, en combinación con el patrón de interferencia láser directa (DLIP), puede generar estructuras superficiales periódicas con oxidación controlada de la superficie y ligera modificación de las propiedades del bulk. Se utilizó un láser de picosegundos para irradiar muestras de titanio puro con tecnología DLIP y se produjeron muestras oxidadas con un patrón de periodicidad de  $10\ \mu\text{m}$ . La variación de los parámetros de procesamiento láser se correlacionó con las propiedades químicas, topográficas y morfológicas resultantes. Se produjeron diferentes estructuras (patrones en forma de línea y patrones de forma cruzada) y se estudió la influencia de la fluencia acumulada (de  $100$  a  $1000\ \text{J}/\text{cm}^2$ ) y el número de pulsos por punto (de  $330$  a  $7000$ ) en diferentes muestras. La correlación entre la topografía superficial, la composición química y la actividad fotocatalítica fue discutida y comparada con trabajos anteriores.

## Acronyms and symbols

C	Solution concentration
$C_0$	Solution reference concentration
CLSM	Confocal laser scanning microscope
d	Spot diameter
DLIP	Direct laser interference patterning
DOE	Diffractive optical element
$e^-$	Electron
$E_g$	Band gap energy
$E_p$	Energy per pulse
$E_{total}$	Total energy
$f$	Repetition rate or frequency of pulses
$F_{acc}$	Accumulated fluence
FIB	Focused ion beam
$F_p$	Fluence per pulse
fs	Femtosecond
GC/MS	Gas chromatography–mass spectrometry
GI-XRD	Grazing incidence X-ray diffraction
$h^+$	Proton hole
HSFL	High spatial frequency LIPSS
LC/MS	Liquid chromatography–mass spectrometry
LIPSS	Laser induced periodic surface structures
LSFL	Low spatial frequency LIPSS
MB	Methylene blue
$n_{acc}$	Number of pulses per point
ns	Nanosecond
p	Periodicity
P	Laser operating power
ps	Picosecond
$R_c$	Roughness mean height
S-ratio	Roughness ratio
$S_a$	Arithmetical mean height
SEM	Scanning electron microscope
USP	Ultra-short pulse
UV	Ultraviolet
$v_x$	Stage speed in x-direction
XRD	X-ray diffraction
$\Delta\nu$	Frequency bandwidth
$\Delta x/\Delta y$	Translation in the x/y-direction
$\tau$	Pulse duration
$\lambda$	Wavelength
$\theta$	Angle between beam and surface

## Table of Contents

Acknowledgments .....	i
Abstract.....	ii
Acronyms and symbols .....	iv
1. Introduction .....	1
2. Theoretical Background.....	2
2.1. Laser structuring .....	2
2.1.1. Basics of light-matter interaction .....	2
2.1.2. Photo-thermal and photo-chemical interaction .....	2
2.1.3. Generation of ultrashort laser pulses.....	3
2.1.4. Comparison of USP laser with continuous laser .....	4
2.1.5. Laser-induced periodic surface structures - LIPSS .....	6
2.1.6. Direct laser interference patterning (DLIP) .....	7
2.2. Titanium oxides.....	9
2.2.1. Phases and properties.....	9
2.2.2. Surface treatment of titanium for biomaterial applications .....	11
2.2.3. Applications of TiO <sub>2</sub> .....	12
2.3. Heterogeneous photocatalysis .....	13
2.3.1. Mechanism and reactions.....	13
2.3.2. Methylene blue degradation as a technique to measure the photocatalytic activity .....	15
2.3.3. Strategies for improving photocatalytic activity .....	17
2.3.4. Applications .....	18
3. Materials and methods .....	19
3.1. Sample preparation .....	19
3.2. Laser structuring .....	19
3.2.1. Picosecond laser .....	19
3.2.2. Surface patterning .....	21
3.2.3. Parameters used .....	22
3.3. Characterization.....	24
3.3.1. Confocal laser scanning microscopy (CLSM) .....	24
3.3.2. Methylene blue degradation .....	25
3.3.3. Scanning electron microscopy (SEM) .....	25
3.3.4. Focused ion beam (FIB) .....	26
3.3.5. Grazing incidence X-ray diffraction (GI-XRD) .....	26
4. Results and analysis.....	27
4.1. Topography and morphology characterization .....	27
4.1.1. Correlation between laser power and spot diameter.....	27
4.1.2. SEM images .....	28
4.1.3. FIB transversal images.....	32



4.1.4. Roughness parameters .....	34
4.2. Methylene blue degradation .....	36
4.3. Grazing incidence X-ray diffraction (GI-XRD) .....	39
5. Conclusions .....	45
Bibliography .....	48
List of Figures .....	57
Appendix.....	58

# 1. Introduction

The surface properties of materials have become increasingly important in relevant fields such as electronics [1–3], medicine [4–6], aerospace [7–9], tribology [10–12], reactors [13–15], etc. The correct use of both bulk and surface properties has made it possible to achieve great advances in science and industrial development. It is for this reason, that several diverse methods of surface treatment have been researched, tested and even developed on a small and large scale. These methods have their advantages and disadvantages, depending on the application, but laser surface treatment has aroused great interest due to the versatility of this method, in addition to its robustness, repeatability, speed and cleanliness [16–18].

In the area of medicine and biomaterials, it is well known that the focus of study of the interaction of different implants with biological systems is on the surface of materials. Biomaterials (materials that interact with biological systems) must present specific properties on their surface to allow them to fulfill their function (cell growth, bone growth, elimination of bacteria, mechanical resistance, reduction of wear and friction, etc.). In the case of dental implants, titanium screws are widely used as one of the best alternatives for dental repairs [19–21]. One advantage of titanium is its ability to attach to bone and allow it to grow into the implant as it heals (a process known as osseointegration). The material is also known for its durability so that the implant can last for years - or even permanently. Titanium implant fractures are also considered rare. Ceramic implants are also used, although they are more fragile and less capable of osseointegration. Instead, they are mainly used for aesthetic reasons and because they are free of metals that can generate allergic reactions or infections. [22]

One of the main problems of titanium implants is the adherence of bacteria to the surface in the form of biofilms, especially in dental implants where the oral cavity presents an ideal chemical medium for their generation and growth. To achieve antibacterial properties on this surface, this work investigates a laser treatment of the titanium surface that aims to form layers of titanium oxides, seeking the formation of  $\text{TiO}_2$  phases that present photocatalytic properties. These phases, especially rutile and anatase, can cause photocatalytic reactions when exposed to irradiation of light of specific ultraviolet wavelengths. The interaction of photons with matter generates pairs of holes and electrons and generates antibacterial properties on the surface of the sample. Titanium oxide surfaces were also studied in different applications due to their photocatalytic properties. Some examples are photoelectrochemical solar energy conversion, self-cleaning materials, air cleaning, water purification, antitumor activity, self-sterilizing surfaces, etc. Due to the multiple applications of surfaces with photocatalytic properties and the importance of their use, developing an efficient technique for the processing of titanium oxide is of great interest. Despite the great properties of titanium oxides (owing to their strong oxidizing power, abundance, low cost, high chemical inertness and photostability), it still suffers from low efficiency and a narrow light response range if it is used alone. Many efforts have been made by forming composites or hybridizing  $\text{TiO}_2$  with other materials to overcome these drawbacks, such as combining the photocatalytic activity of  $\text{TiO}_2$  with the absorptivity of porous carbons [23–25], reducing electron-hole recombination rate [24] and doping to achieve a narrow band gap [26–30].

This work presents the implementation of an Ultrashort Laser Pulse (USP) laser with a pulse duration of the order of picoseconds (picosecond laser), combined with the Direct Laser Interference Patterning (DLIP) technique. The formation of intensity patterns due to the interaction of coherent laser beams allows the formation of structures with surface topographies in the order of microns and submicrons [31]. This technique allows treatment of the surface of the material both topologically and chemically, in addition to being a fast, versatile and clean technique, with the possibility of applying it on an industrial scale for the biomaterials industry.

The aim of this thesis is to study the influence of the surface modification of pure titanium by direct laser interference patterning into the photocatalytic activity. Despite the existence of other works where DLIP was used, very little research has been carried out with the use of picosecond lasers. The influence of the experimental factors that control the structuring process is the focus of interest of this study. The morphology and chemistry of the surface structure as well as the photocatalytic activity are studied.

## 2. Theoretical Background

### 2.1. Laser structuring

In this section, the basic concepts of the generation of ultrashort laser pulses and their interaction with matter will be briefly explained. The interaction of light with the surface of the material, the different chemical and thermal phenomena, the characteristics of an ultrashort pulse laser and the results of its interaction with matter and the generation of structures and topographies on the surface (such as laser-induced periodic surface structures), are some of the topics to be explained and that will be very useful in the discussions of the next chapters. In addition, direct laser interference patterning (DLIP) will be briefly explained due to its advantages when used together with ultrashort pulses.

#### 2.1.1. Basics of light-matter interaction

To generate any permanent effect on a material surface, light from a laser source must first be absorbed. The absorption coefficient and the optical reflectance of the material describe how the energy of the laser is absorbed. The light that strikes the surface of the material will be separated into reflected, absorbed and transmitted light. The percentage of reflected light depends on the polarization and the incidence angle of the beam, the surface roughness, and the refractive indexes of the material and the atmosphere (this discontinuity at the interface in the real index of refraction is responsible for the reflection of the beam).

The frequency of the light source (through the dispersion relation of its refraction index) and the temperature of the material (through changes in the permittivity, band structure, plasma oscillations, or the phase) will also affect the reflectivity. Other optical resonances, like bulk plasmon and polaritons and photon-electron interactions, are possible in small scale or structured materials, but will not be explored in more detail here. [32]

Within the material, a reduction of the light intensity will be caused by the absorption as it travels deeper into the material. The material's absorption coefficient  $\alpha$  determines the rate at which it decays. The Beer-Lambert law describes this change in the intensity:

$$I(z) = I_0 e^{-\alpha z} \quad (1)$$

Where  $z$  represents the depth and  $I_0$  the intensity just inside the surface after the reflection loss. The inverse of the absorption coefficient is known as absorption depth and describes the depth at which the transmitted intensity considerably drops (to about 36% or more precisely  $1/e$ ) of its initial value. This depth in materials is a function of the wavelength. Thus, a short absorption depth can be chosen at a specific wavelength when a local modification of the surface is desired. In the case of metals, the absorption depth (or penetration depth) is very limited, in the range of several nm (according to [33], 15-45 nm depth, for titanium layers from 12 to 1470 nm).

#### 2.1.2. Photo-thermal and photo-chemical interaction

Laser interaction with matter can be described based on photo-thermal and photo-chemical models. The interaction of laser light with materials starts with single-photon material excitation. If the excitation energy is instantaneously transformed into heat, the increase in temperature changes the optical properties of the material and thereby the absorbed laser power. [34] It should be noticed that in many cases, a unique classification into chemical and non-chemical laser processing is difficult or impossible but often one of them dominates during the process.

The simplest example of a photo-thermal mechanism is laser melting. This is the case when the laser energy density is not high enough to induce the direct laser ablation, and this mainly concerns metals, semiconductors, and some ceramics. In the photo-thermal process, the thermalization of the excitation dominates over other initial processing steps, i.e., desorption of species from the surface, structural rearrangements of atoms or molecules, or initial steps in a chemical reaction. The detailed excitation mechanisms become therefore irrelevant, and the laser can be considered simply as a heating source. The temperature rise can also result in material ablation (vaporization) with or without surface melting.

If the photo energy is high enough, laser light excitation can result in direct bond breaking. As a consequence, single atoms, molecules, clusters or fragments are desorbed from the surface. The photo-chemically dissociated bonds can build up stresses which result in ablation, without any change in surface temperature. For this reason, this process is called photo-chemical ablation.

The process in which both thermal and non-thermal mechanisms contribute to the overall ablation rate is called photo-physical ablation. An example would be a system in which the lifetime of electronically excited species or broken bonds is so long that the species desorbs from the surface before the total excitation energy is dissipated into heat. This desorption of excited species is enhanced by the temperature rise. Similarly, thermally and non-thermally generated defects, stresses, and volume changes may again influence the overall process. The above defined photo-thermal and photo-chemical ablations can be considered as limiting cases of the photo-physical ablation mechanism. [34]

### 2.1.3. Generation of ultrashort laser pulses

Many fundamental processes in nature, such as chemical and biochemical reactions and phase transitions, involve changes in the structure of matter, i.e. the rearrangement of the constituent atoms and molecules, occurring transiently on time-scales comparable with the natural oscillation periods of atoms and molecules, that is femtoseconds to picoseconds. The ultra-short pulsed lasers are laser systems with high peak power that use laser pulses shorter than 10 picoseconds down to several femtoseconds (ps- and fs-pulses), in contrast to longer pulses (i.e., nanoseconds) or even the continuous wave (CW) lasers where the power is constant with time. Compared with longer pulse widths, ultrafast pulses are unique in that they are characterized by relatively high peak intensities and can interact with materials on a timescale faster than lattice disorder and heat diffusion do. These two features allow ultrafast lasers to very precisely control and manipulate chemical and physical changes on the surface. Atomic and molecular reactions, such as the relaxation of energetically excited electrons, occur within this time scale ( $10^{-13}$  -  $10^{-11}$  s) [35].

The necessary condition to generate pulse duration of this magnitude implies a sufficient spectral bandwidth of the laser medium. According to the Fourier transform, the pulse duration is thus limited by the frequency bandwidth of the laser:

$$\tau = \frac{1}{\Delta\nu} \quad (2)$$

where  $\tau$  is the pulse duration and  $\Delta\nu$  is the frequency bandwidth. In the case of ultra short pulses, that implies lasing over a considerable bandwidth, quite contrary to the very narrow bandwidths typical for continuous lasers.

To induce these short pulse durations, a fixed phase relationship between the longitudinal modes of the laser's resonant cavity should be induced. This resonant cavity consists of two mirrors containing standing electromagnetic waves reflecting back and forth between the cavity's walls. Lasers produce radiation over some natural bandwidth or range of frequencies based on the spectral bandwidth of the electromagnetic frequencies emitted by the active medium. Since light is a wave, when bouncing between the mirrors of the cavity, the light will constructively and destructively interfere with itself, leading to the formation of standing waves or modes between the mirrors. These standing waves form a discrete set of frequencies, known as the longitudinal modes of the cavity. These modes are the only

frequencies of light that are self-regenerating and allowed to oscillate by the resonant cavity; all other frequencies of light are suppressed. This constructive interference between these modes can cause the laser light to be produced as a train of pulses. The laser is then said to be "phase-locked" or "mode-locked" and this technique is known as mode-locking. So, for a given resonator length, the allowed modes are those for which the separation distance of the mirrors  $L$  is an exact multiple of half the wavelength of the light  $\lambda$ :

$$L = N \frac{\lambda}{2} \quad (3)$$

Being  $N$  a natural number. The frequency difference between any two adjacent modes  $N$  and  $N+1$  is given by:

$$\Delta\nu = \frac{c}{2L} \quad (4)$$

Where  $c$  is the speed of light.

Methods for producing mode-locking in a laser may be classified as either "active" or "passive". Active methods typically involve using an external signal to induce a modulation of the intracavity light. Passive methods do not use an external signal (such as the driving signal of a modulator) but rely on placing some element into the laser cavity which causes self-modulation of the light. A commonly used device to achieve this is a saturable absorber.

A saturable absorber is an optical device that exhibits an intensity-dependent transmission, meaning that the device behaves differently depending on the intensity of the light passing through it. For passive mode-locking, ideally a saturable absorber selectively absorbs low-intensity light, but transmits light of sufficiently high intensity. When placed in a laser cavity, a saturable absorber attenuates low-intensity constant-wave light (pulse wings). However, because of the somewhat random intensity fluctuations experienced by an un-mode-locked laser, any random, intense spike is transmitted preferentially by the saturable absorber. As the light in the cavity oscillates, this process repeats, leading to the selective amplification of the high-intensity spikes and the absorption of the low-intensity light. After many round trips, this leads to a train of pulses and mode-locking of the laser. [34]

Saturable absorbers are commonly liquid organic dyes, but they can also be made from doped crystals and semiconductors. Semiconductor absorbers tend to exhibit very fast response times ( $\sim 100$  fs), which is one of the factors that determine the final duration of the pulses in a passively mode-locked laser. In a colliding-pulse mode-locked laser, the absorber steepens the leading edge, while the lasing medium steepens the trailing edge of the pulse.

There are also passive mode-locking schemes that do not rely on materials that directly display an intensity-dependent absorption. In these methods, nonlinear optical effects in intracavity components are used to provide a method of selectively amplifying high-intensity light in the cavity and attenuation of low-intensity light. One of the most successful schemes is called Kerr-lens mode-locking (KLM), also sometimes called "self-mode-locking". This uses a nonlinear optical process, the optical Kerr effect, which results in high-intensity light being focused differently from low-intensity light. By careful arrangement of an aperture in the laser cavity, this effect can be exploited to produce the equivalent of an ultra-fast response-time saturable absorber. [34]

#### 2.1.4. Comparison of USP laser with continuous laser

The interaction of USP with materials depends on many factors but specially on the lattice organization and structure. That is why the results of interaction between these pulses and metals, is different for other materials like polymers and ceramics (dielectrics, semiconductors, etc.). In the case of polymers and ceramics, it is assumed that most of the absorption for USP pulses is due to multi-photon interactions, in comparison with nanosecond or larger laser pulse durations. For the case of pico- and

femtoseconds lasers, the extremely high intensities activate optical breakdown and multiphoton absorption which can decrease the absorption rates. During the interaction, bonds between electrons in the irradiated sample are directly broken. This is a nonthermal process with no or minimal heating of the sample. Multiphoton absorption facilitates absorption in materials with low linear, optical absorption (i.e., wide bandgap semiconductors) that are difficult to machine with traditional ns lasers [36].

For the case of metals, the absorption of laser radiation results in transient nonequilibrium of the electron gas with the lattice near a metal surface. Since the heat capacity of degenerate electron gas is small, the electron temperature follows, practically with no delay, the shape of the laser pulse. Heating of the lattice proceeds rather slowly due to the great difference between electron and ion mass (or, what is the same, due to the difference between the sound speed and electron Fermi velocity). The characteristic time of lattice heating for different metals lies in the range 1 to 100 ps. [37] This means that, during a ultrashort laser pulse, the laser energy absorbed is stored in the electron subsystem, whereas the lattice remains at its considerably lower temperature. Due to the small specific heat of degenerate electron gas, its temperature is much higher than in the case of electron-lattice equilibrium.

When the sample surface is exposed to the laser source, the front part of the USP-laser pulse is absorbed and the extreme electronic excitation creates a dense electron-hole plasma, which is responsible for the absorption and partial reflection of the remaining pulse. The plasma then delivers energy to the lattice, surface interatomic bonds are weakened due to the high degree of electronic excitation and the lattice is disordered through cold atomic motion. The sample enters an extreme nonequilibrium state with several thousand kelvin electron gas inside a room-temperature lattice. What happens post-absorption can vary dramatically, depending on the target material's relationship with pulse wavelength and energy [38]. Three resulting regimes are possible: nonthermal melting through an ultrafast phase transition, thermal phase melting, and ablation.

Nonthermal melting is achieved using fluences twice the melting threshold or greater and exhibiting a significantly faster (picoseconds) change of the linear optical properties at the surface, with reflectivity reaching, in a few hundred femtoseconds, values equal to that of the conventional liquid phase [39]. Ablation for USP-laser is described by a two-temperatures model, where the lattice and the electrons can achieve different temperatures, as it was already explained. Here, the extreme pressures, densities and temperatures build up and accelerate the ionized material to enormous velocities (phase explosion) and due to the short interaction time, the material cannot evaporate continuously but is transferred into a state of overheated liquid (this merges into a high-pressure mixture of liquid droplets and vapor expanding rapidly) [40].

On the other hand, nanosecond pulses excite electrons in a distinctly different process as compared to the USP-excitation (like pico- or femtosecond lasers). When a ns-pulse delivers energy to a material, excited electrons transfer energy to the lattice during the time of the electron excitation [41]. Electrons and the lattice thus remain in equilibrium throughout the excitation process. The ns laser heats the solid to its melting temperature during the length of the laser pulse. The ns-absorption processes are linear with a much larger absorption length than fs absorption. Linear absorption can lead to deeper melt depths. Compared to the fs-laser case, the ns-induced temperature gradient between the molten layer and the solid substrate is smaller and distributed over a longer distance. Consequently, the melt duration is longer, and the resolidification-front speed is slower. If the laser wavelength is transparent to the material, absorption is induced by multiphoton absorption for both ultrafast and ns-lasers. Then the ns-laser will have a longer penetration depth due to a smaller absorption cross section as compared with an ultrafast laser. In contrast, for the opaque materials, the penetration depth is determined by the absorption coefficient due to single-photon absorption for both lasers. In the case of a small absorption coefficient, a shorter penetration depth of the ultrafast laser may be obtained due to a combination of linear and nonlinear absorption [41].

The longer ns-pulse widths translate to lower peak powers compared to fs lasers. Operating at lower peak powers, ns lasers ablate materials by a thermal process. This thermal ablation causes a large heat-affected zone that may induce melt redeposition and shockwaves, leaving behind thermally induced defects such as cracks and chipping. In machining or surgery applications, the thermal effects in ns ablation can lead to a larger heat-affected zone, more collateral damage, and less precise machining compared to fs ablation.

Although picosecond lasers are considered USP lasers, they have denoted differences with respect to femtosecond lasers, because the limit value of this regimen depends on the properties of the material (fluence threshold). For this reason, the picosecond laser can be considered as a technology that contains characteristics of the continuous regime (or long duration pulses) and characteristics of the ultrashort pulse regime. The resulting ablation of both cases was also observed for picosecond laser pulses in previous work [42].

USP pulses applications are consequently related to many areas of physics and chemistry as well as in biology. Engineering applications now range from picosecond or femtosecond electronics to laser fusion. USP pulses have two primary properties that make them particularly useful: ultrashort duration and, when needed, very high power. They are used for many applications in different topics: solar cells films processing [43], dermatology [44], drilling of hard ceramics [45], removal of hard dental substances [46], laser spectrometry [47], etc.

### **2.1.5. Laser-induced periodic surface structures - LIPSS**

The semi-periodic nanometer- and micrometer-scale structures, generated on almost any material by irradiation with polarized radiation, are called LIPSS (laser-induced periodic surface structures). They exhibit a wide range of feature sizes and shapes (see Figure 1) and are independent of the crystal orientation. The formation of LIPSS in the shape of ripples occurs when surface waves in the surface develop as the incoming light interferes with the scattered light off of the material. Self-focusing occurs in the valleys, as more pulses impinge on the ripples, and can result in larger structures that go deeper into the material. The orientation of the ripples is approximately perpendicular to the polarization and the periodicity is in the size range of the laser wavelength. The LIPSS created are therefore dependent on the wavelength and polarization of the incoming ultrashort laser pulse and the index of refraction of the material processed [48].

Upon irradiation with linearly polarized femtosecond laser pulses, typically two different types of fs-LIPSS are observed. LIPSS with a periodicity close to the irradiation wavelength  $\lambda$  are called *low spatial frequency LIPSS* (LSFL), while structures with periods significantly smaller than  $\lambda$  are referred to as *high spatial frequency LIPSS* (HSFL) [49]. LSFL on titanium upon IR fs-laser pulse irradiation at 800 nm (IR-LSFL) are always orientated perpendicular to the polarization of the incident fs-laser radiation and exhibit a sub-wavelength periodicity that, for the used wavelength, ranges between 500 nm and 800 nm. Upon UV fs-laser pulse irradiation at 400 nm wavelength, LSFL with periods of 390 – 480 nm and HSFL with periods of 200 – 320 nm can be detected [49]. As for the IR irradiation case, the UV-LSFL orientation is perpendicular to the polarization direction while the UV-HSFL are oriented parallel to it (the morphological LIPSS characteristics are summarized in Figure 1). The time delay between the two pulses controlled the morphology of the LIPSS and a variation of this parameter can involve the production of varying IR-LSFL and UV-LSFL structures. For this work, this time delay is not relevant, as the pulse frequency is not high enough to reach such influences.





Wavelength $\lambda$	LIPSS type & Orientation	Period $\Lambda$	SEM micrograph
IR: 800 nm	LSFL $\perp$	500 - 800 nm	
			
UV: 400 nm	HSFL $\parallel$	65 - 150 nm	
	LSFL $\perp$	390 - 480 nm	
	HSFL* $\parallel$	200 - 320 nm	

Figure 1 - Morphological characteristics of different types of LIPSS (LSFL & HSFL) on titanium after irradiation by ultrashort laser pulses ( $\tau = 50$  fs) at 800 nm (IR) and 400 nm (UV) wavelengths [49].

LIPSS provide a simple way of surface nanostructuring toward a control of optical, mechanical, or chemical surface properties for functionalization. The size, morphology and orientation of the LIPSS can change some surface properties, like the wetting properties or the cellular reactions with biological environments [49].

### 2.1.6. Direct laser interference patterning (DLIP)

Direct Laser Interference Patterning (DLIP) is a method that implements physical interference phenomena to produce periodic structures on surfaces by transferring the shape of the pattern directly to the material by selective laser ablation or melting. In general, interference patterns can be obtained by splitting a coherent laser beam (e.g., by using beam splitters) into two or more sub-beams which are later overlapped at the workpiece. [50]

The interference of two, three and four laser beams (see Figure 2.d, Figure 2.e and Figure 2.f, respectively) leads to an effective modulation of the laser intensity profile (line-like: Figure 2.a; dot-like: Figure 2.b and Figure 2.c). The patterns can be directly transferred to any material which absorbs the energy of the laser at the selected wavelength. The structuring process is based on photothermal, photophysical, or photochemical mechanisms, depending on the type of material. In general, polymers and ceramics are processed with UV laser radiation, whereas green or IR lasers are applied to treat metals and polymeric coatings. In the case of metals, the DLIP process is dominated by the photothermal interaction that involves local melting and/or selective ablation at the interference maxima positions.



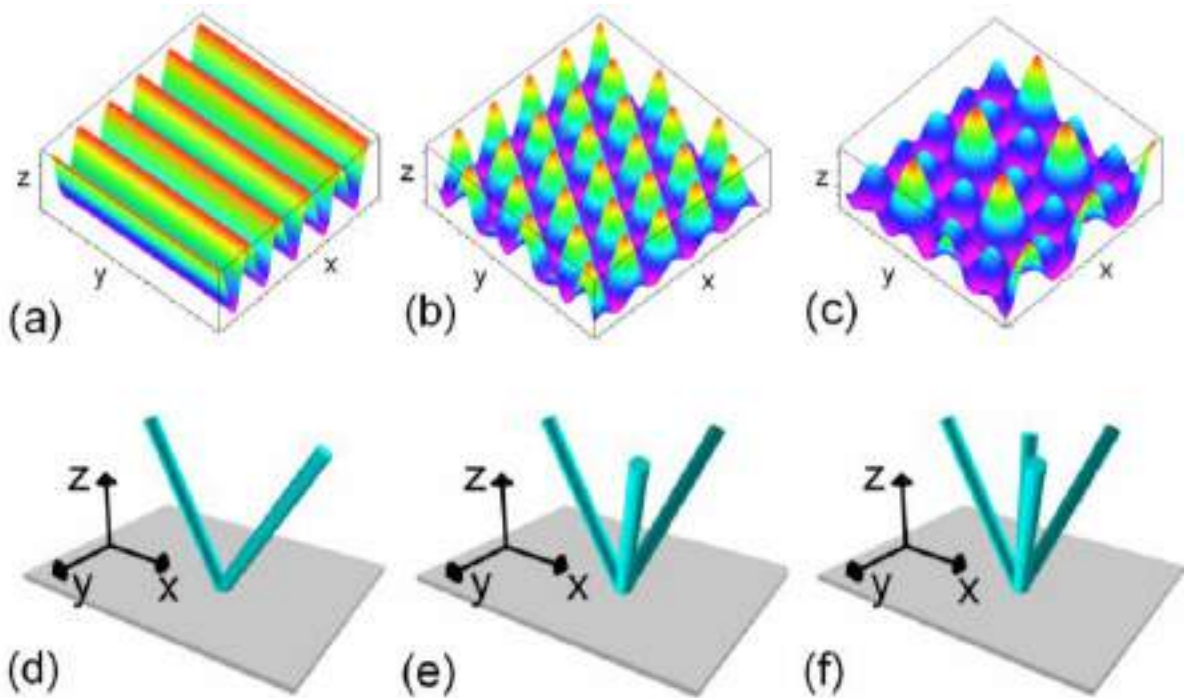


Figure 2 - Calculated intensity distribution for (a) two-beam interference (d), (b) three-beam interference assuming symmetrical configuration (e), and (c) four-beam interference under the conditions shown in (f) [51]

For nanosecond laser pulses, the primary material removal mechanism is ablation but also substantial melting occurs. The minimum achievable spatial period is therefore limited by the thermal diffusion length (e.g., 1  $\mu\text{m}$  for stainless steel and titanium for 10 ns pulses). By using ultra-short pulsed lasers (ps and fs laser systems), minor thermal damage is observed and spatial periods below 1  $\mu\text{m}$  are feasible. [50]

An industrial application of the DLIP technology will only be possible if compact optical-head solutions are available and the applicability of the technology is demonstrated in an operational environment. The technological advances in the field of DLIP can be summarized on an industrial scale from 1st Generation (laboratory setup) to 4th Generation (high resolution and flexibility) [51]. The development level of this alternatives for industrial applications is quantitatively rated with Technology Readiness Levels (TRL), a type of measurement system used to assess the maturity level of a particular technology. Some results of experimental works with DLIP technology: fabrication speeds up to 0.7  $\text{m}^2/\text{min}$  have been already experimentally proven using 180 W IR pulse laser; fabrication speeds up to several  $\text{m}^2/\text{min}$  are possible if laser systems with high power (e.g., 600 W) are used and processing cost between 1 and 3  $\text{€}/\text{m}^2$  are achievable, even considering amortization of equipment after 3 years (2nd and 3rd generation) [51].

DLIP technology can be combined with USP laser to create and/or study periodic surface topographies. These structures can be produced to understand the thermal interactions of this process with different kinds of materials. For example, it was found that the processability of materials showing low absorptivity at the wavelength can be attributed to the altered laser-material interaction during USP irradiation. On insulating materials, ablation is strongly related to the critical threshold fluence inducing multiphoton absorption. In the case of metals, an alteration of the occurring ablation mechanism related to material specific threshold fluences was taken into account [31].

Some examples of applications of this technology are: film adhesion in lithium-ion batteries [52], wettability control of polycarbonate [53] and Ti-6Al-4V [54] substrates, decreased bacterial attachment on polymeric materials (polyimide, polystyrene) [55], etc.

## 2.2. Titanium oxides

Titanium oxides are among the most abundant materials in the Earth's crust. Because of the multiple valence states of Ti ions, titanium oxides include titanium monoxide ( $\text{Ti}^{2+}\text{O}$ ), titanium sesquioxide ( $\text{Ti}^{3+}_2\text{O}_3$ ), the Magneli phases ( $\text{Ti}_n\text{O}_{2n-1}$ , where  $n = 3, 4, 5$ , etc.), and titanium dioxide ( $\text{Ti}^{4+}\text{O}_2$ ). In the family,  $\text{TiO}_2$  is the most famous member because of its great importance in fundamental research and practical applications.

### 2.2.1. Phases and properties

Depending on the conditions (mostly temperature and pressure), titanium oxide has many polymorphs, including stable and metastable phases. Thermodynamically, the most stable oxide is titanium dioxide (titania), which occurs naturally in the form of rutile, anatase and brookite. There are other metastable and high-pressure forms with tetragonal, monoclinic, cubic and orthorhombic crystallographic structures. Among these polymorphs, only rutile and anatase show a meaningful photocatalytic effect (other phases, that may have photocatalytic properties, will be mentioned in the next chapters) and both of them are inexpensive, chemically stable and harmless as bulk material. The crystallographic structure of rutile and anatase is usually represented by the distorted  $\text{TiO}_6$  octahedron building blocks (Figure 3). The rutile shares the corners of the  $\text{TiO}_6$  octahedra and anatase the edges with the neighbor cell.

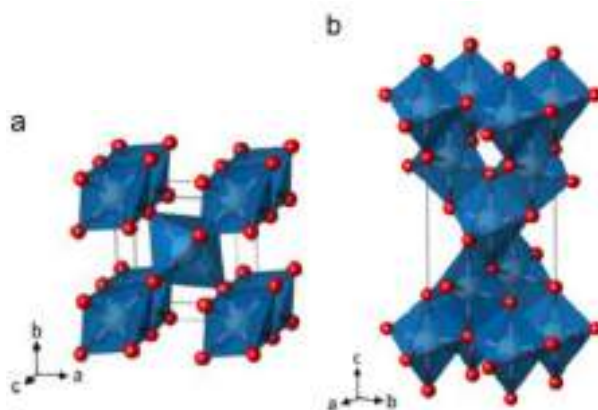


Figure 3 - Crystallographic structure of (a) rutile and (b) anatase. Titanium atoms (white) and oxygen atoms (red) form  $\text{TiO}_6$  polyhedra in the lattices [56].

Anatase possesses an energy band gap of 3.2 eV with an absorption edge at 386 nm which lies in the near UV range. On the other hand, rutile has a narrower energy band gap of 3.02 eV with an absorption edge in the visible spectrum at 416 nm. During the photoexcitation, the light will be absorbed and an electron is elevated from the valence band to the conduction band of  $\text{TiO}_2$ , leaving behind a hole in the valence band.

Being the thermodynamically most stable phase with a very high calcination temperature, rutile possesses relatively low specific surface area and poor surface-textural properties. In contrast, the metastable anatase crystallizes at very low to intermediate temperature thus restraining the high surface area that is vital for pollutant adsorption and incident photon absorption [57], which results in anatase having a higher photocatalytic ability than rutile despite it showing a higher bandgap energy.

Many other phases of titanium oxides have been studied theoretically and experimentally. Several authors worked and studied the titanium-oxygen system and the different thermodynamically stable phases of the binary system [58–62]. Among these works, the one of *Cancarovic et. al.* [62] stands out, who used a theoretical model and an extensive database of different bibliographic sources, to build the Ti-O binary system at 1 bar pressure.

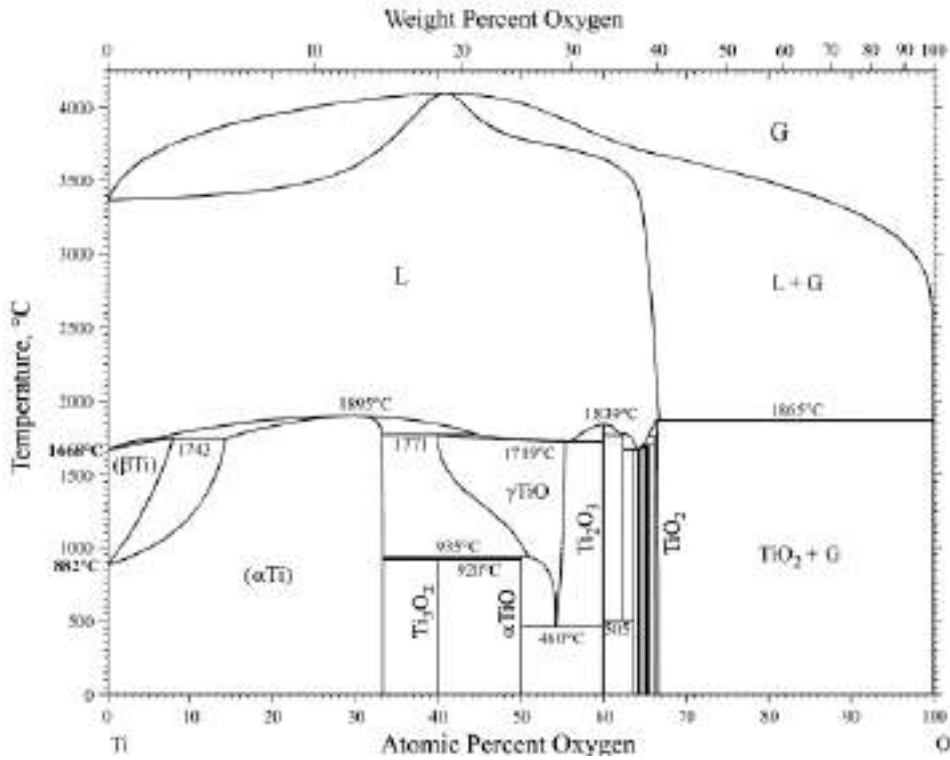


Figure 4 - Ti-O phase diagram calculated by Canceravic et. al. [62]

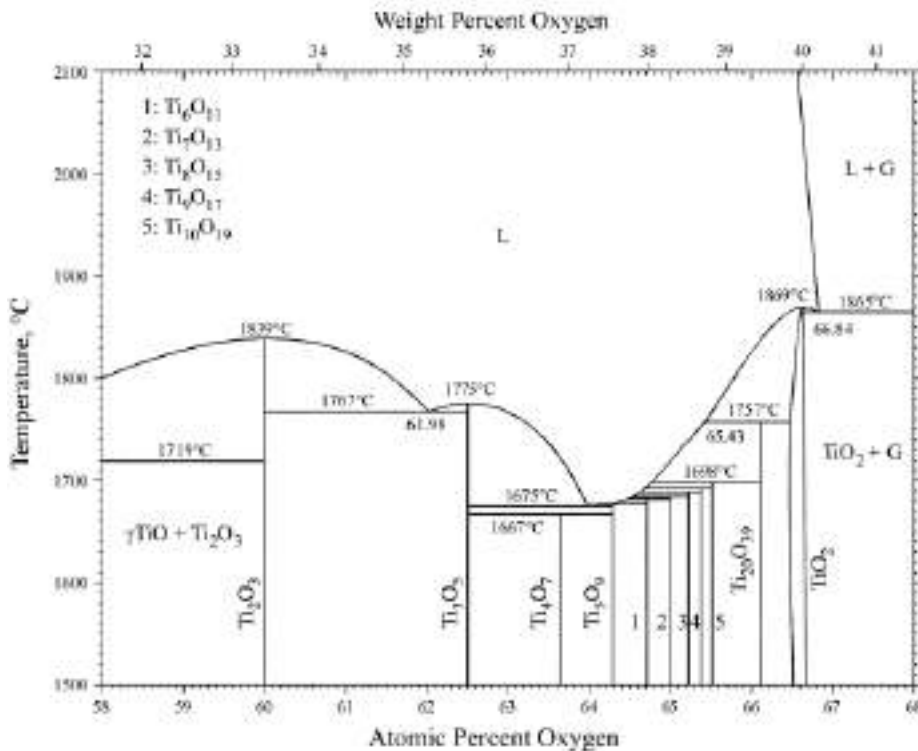


Figure 5 - Enlargement of Figure 4 from 58 to 68 at %O

Among all these phases, some arouse greater interest and have been studied by different authors, as is the case of titanium monoxide TiO (mineral name: hongquite) and corundum Ti<sub>2</sub>O<sub>3</sub> (mineral name: tistarite).

In contrast to  $Ti^{4+}$  containing titanium dioxide ( $TiO_2$ ), which has a wide bandgap ( $\sim 3.0$  eV) and has been widely explored for catalysis and energy applications, titanium sesquioxide ( $Ti_2O_3$ ) with an intermediate valence state ( $Ti^{3+}$ ) possesses an ultranarrow bandgap ( $\sim 0.1$  eV) and has been much less investigated. Although the importance of  $Ti^{3+}$  to the applications of  $TiO_2$  is widely recognized, the connection between  $TiO_2$  and  $Ti_2O_3$  and the transformation pathway remain unknown [63].

Titanium monoxide ( $TiO_{0.80}$  to  $TiO_{1.25}$ ) is non-stoichiometric and this is caused by vacancies of either Ti or O in the defect rock salt structure. Contains a high equilibrium concentration of randomly distributed vacancies in the titanium and oxygen sublattices and has a broad region of chemical and structural homogeneity. It has high electrical conductivity and semiconducting behavior, high melting point and hardness and strength at elevated temperatures [64–66].

## 2.2.2. Surface treatment of titanium for biomaterial applications

Biomaterial applications make use of all classes of materials: metals, ceramics, polymers and composites. These are divided roughly into three user types: (a) inert or relatively inert with minimal host response; (b) bioactive, which stimulates bonding to the surrounding tissue (for example dental implants); and (c) biodegradable, which resorb in the body over some time. Events leading to the integration of an implant into bone, which in turn determine the performance of the device, take place largely at the tissue–implant interface. The main requirements for a biomaterial to function properly in an osseous site include good biocompatibility favoring bone apposition, adequate mechanical properties and the ability to ensure skeletal functions [67].

Bioactivity and bio integration are the two essential aspects of these interactions. Bioactivity and the maintenance of skeletal functions are usually attributed to the ability to induce a hydroxyapatite (HA) layer on a material's surface in physiological conditions. The close apposition between bone and an implant surface, or osseointegration, presented as the ability to promote bone cells anchorage, attachment, spreading, growth and differentiation, is another key factor for successful implantation of a biomaterial for dental and orthopaedic applications [68–70].

The bulk properties of biomaterials, such as non-toxicity, corrosion resistance or controlled degradability, modulus of elasticity, and fatigue strength have long been recognized to be highly relevant in terms of the selection of the right biomaterials for a specific biomedical application. The events after implantation include interactions between the biological environment and artificial material surfaces, the onset of biological reactions, as well as the particular response paths chosen by the body. The material surface plays an extremely important role in the response of the biological environment to artificial medical devices.

Titanium and titanium alloys are widely used in biomedical devices and components, especially as hard tissue replacements as well as in cardiac and cardiovascular applications, because of their desirable properties, such as relatively low modulus, good fatigue strength, formability, machinability, corrosion resistance, and biocompatibility. However, titanium and its alloys cannot meet all of the clinical requirements. Therefore, to improve the biological, chemical, and mechanical properties, surface modification is often performed [71].

In implants made of titanium, the initial manufacturing steps usually lead to an oxidized, contaminated surface layer that is often stressed and plastically deformed, non-uniform and rather poorly defined. Such “native” surfaces are not appropriate for biomedical applications and some surface treatment must be performed. Another important reason for conducting surface modification to titanium medical devices is that specific surface properties, that are different from those in the bulk, are often required. For example, to accomplish biological integration, it is necessary to have good bone formability. In blood-contacting devices, such as artificial heart valves, blood compatibility is crucial. In other applications, good wear and corrosion resistance are also required. The proper surface modification techniques not only retain the excellent bulk attributes of titanium and its alloys, such as relatively low modulus, good fatigue strength, formability and machinability, but also improve specific surface properties required by different clinical applications.

Plasma sprayed coatings (titanium, hydroxyapatite, dicalcium silicate/ZnO<sub>2</sub>, YSZ), blasting (sand, ZnO<sub>2</sub>) and acid etching of the surface, are some of the surface treatments used to enhance the surface properties of titanium implants. The results of these treatments are the improvement of osseointegration, cell growth, biocompatibility with no cytotoxic and adhesion to the bone [20,72]. Also, a large number of structures and morphologies on the surface of implants can be obtained by laser treatments with [73] and without [74] surface oxidation, to enhance osteogenic activity and *in vivo* osseointegration. All these techniques can be combined with heat treatments to control, for example, the proportion of rutile and anatase in the samples (in the case of oxidized surfaces). This can lead to an increase in osteogenic ability both *in vitro* and *in vivo*, as the mixture of rutile and anatase might be responsible for enhancing the osteogenic properties of this biomaterial [73]. Anatase film can attract calcium and phosphate ions from the physiological environment to form an apatite coating. In contrast, the rutile film on titanium was associated not only with basic hydroxyl groups on the surface but also with acidic hydroxyl groups and surface energy. The existence of both anatase and rutile could help improve the osteogenic activity of titanium.

The biological responses to biomaterials and devices are largely controlled by their surface chemistry and structure. That is to say, the surface characteristics play a role in the functioning of biomaterial. In the case of medical implants, the importance of surface science is quite obvious. It has been hypothesized that tissue–biomaterial interactions are governed by surface properties and that the important interactions occur within around 1 nm of the biomaterial surface. Natural biological structures appear to be able to interact selectively with relevant biomolecules while resisting nonspecific interactions. Furthermore, biological interfaces are highly dynamic.

Ultrashort pulsed lasers have some unique properties for surface treatment. The electromagnetic radiation of a laser beam is absorbed within the first atomic layers for opaque materials, such as metals, and there are no associated hot gas jets, eddy currents or even radiation spillage outside the optically defined beam area. Thus, it is a true surface heater and a unique tool for surface engineering.

Some interesting applications of laser surface treatment in biomaterials are: improve corrosion resistance in NiTi shape memory alloys [75], enhance the corrosion and wear resistance of metallic biomaterials [76], improve the fatigue performance of Ti6Al4V [77], enhance human osteoblast cell adhesion and proliferation on 316 LS stainless steel [78] and much more.

Common advantages of laser surfacing compared to alternatives are [79]:

- chemical cleanliness;
- controlled thermal penetration and, therefore, distortion;
- controlled thermal profile and, therefore, shape and location of the heat affected region;
- less after-machining, if any, is required;
- remote noncontact processing is usually possible;
- relatively easy to automate.

### 2.2.3. Applications of TiO<sub>2</sub>

One of the most important characteristics of titanium dioxide is the interaction of the material surface with the surrounding environment. That is why it turns important to look for higher specific surfaces. For that reason, nanoparticles of TiO<sub>2</sub> are one of the most common forms of application in different fields. There are also TiO<sub>2</sub> films where the specific surface can be increased with surface treatments. Some applications of TiO<sub>2</sub> in different fields and morphologies are summarized in Table 1:

Application	Property	Morphology	Reference
Sustainable agriculture	Photocatalytic activity	Nanoparticles	[80]
Alcohol microsensor	Electrochemical	Nanosized thin films	[81]
Heat transfer	Thermal conductivity and viscosity	Nanofluids	[82]
Antibacterial effect	Photocatalytic activity	Colloidal suspension	[83]
Removal of pollutants from water	Photocatalytic activity	Nanoparticles	[84]
Electricity generation in solar cells	Photocatalytic activity	Nanotubes	[85]
Photodynamic therapy for cancer treatment	Photocatalytic activity	Nanoparticles	[86]
Biosensors	Electrochemical	Nanostructured	[87]

Table 1 - Titanium oxides applications and references

## 2.3. Heterogeneous photocatalysis

### 2.3.1. Mechanism and reactions

Catalysis is a term describing a process in which the rate of a chemical reaction is influenced by the presence of a substance (the catalyst) that is not consumed during the reaction and that is subsequently removed if it is not to constitute an impurity in the final product [88]. Photocatalysis is a type of catalysis that results in the modification of the rate of a photoreaction - a chemical reaction that involves the absorption of light by one or more reacting species - by adding substances (catalysts) that participate in the chemical reaction without being consumed [89]. Photocatalysis includes reactions that take place by utilizing light and a semiconductor. The substrate that absorbs light and acts as a catalyst for chemical reactions is known as a photocatalyst. All the photocatalysts are basically semiconductors, as photocatalysis is a phenomenon, in which an electron-hole pair is generated on exposure of a semiconducting material to light.

The photocatalytic reactions can be categorized into two types based on the appearance of the physical state of reactants.

- Homogeneous photocatalysis: When both the semiconductor and reactant are in the same phase, i.e., gas, solid, or liquid.
- Heterogeneous photocatalysis: When both the semiconductor and reactant are in different phases.

The energy difference between the valence band and the conduction band is known as the band gap ( $E_g$ ). When a photocatalyst is exposed to light of the desired wavelength (sufficient energy), the energy of photons is absorbed by an electron ( $e^-$ ) of the valence band and it is excited to the conduction band. In this process, a hole ( $h^+$ ) is created in the valence band. This process leads to the formation of a photo-excitation state, and an  $e^-$  and  $h^+$  pair is generated (Figure 6). If these electron-hole pairs are somehow trapped for some time on the semiconductor surface and their recombination is prevented, reactions between the excited electrons with oxidants produce reduced products, and/or reactions between the generated holes with reductants generate oxidized products. The importance of photocatalysis lies in the fact that a photocatalyst provides both an oxidation as well as a reduction environment, simultaneously [90].

The excited electrons and holes in the absence of suitable electron and hole scavengers tend to recombine very quickly, dissipating the energy as heat. Photocatalytic activity, therefore, is strongly dependent on the competition between the surface transfer of charge carriers and electron-hole recombination.

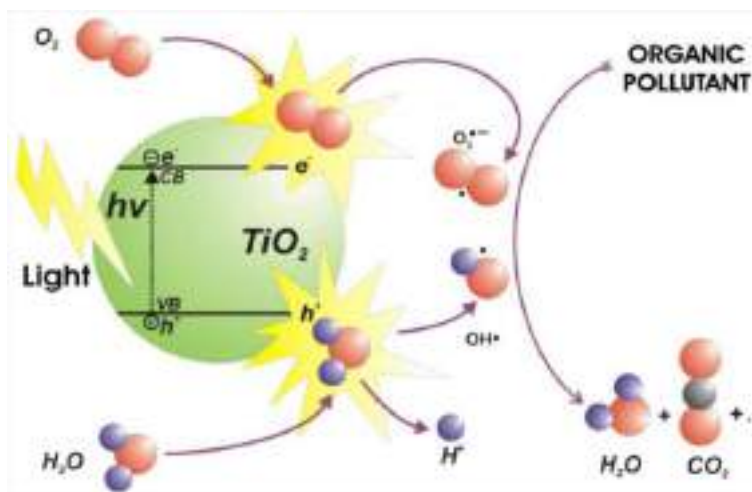


Figure 6 - Schematic illustration of the general mechanism of the heterogeneous photocatalytic process

Heterogeneous photocatalysis can be carried out in various media: gas phase, pure organic liquid phases or aqueous solutions. This last case is the most common, as water is considered the best solvent or reaction medium, because of its properties and the advantages of its use. It is an excellent solvent (because of its polarity and ability to form hydrogen bonds), it is very cheap and easy to get, and its post-treatment and cleaning are easy compared to organic solvents, thus becoming the most sustainable option.

As for classical heterogeneous catalysis, the overall process can be decomposed into five independent steps [91]:

1. Transfer of the reactants in the fluid phase to the surface.
2. Adsorption of at least one of the reactants.
3. Reaction in the adsorbed phase.
4. Desorption of the product(s).
5. Removal of the products from the interface region.

Step 3 (reaction in the adsorbed phase) contains all the photoelectronic processes and can be decomposed as follows:

- 3.1. Absorption of the photons by the solid and not by reactants. There is no photochemistry in the adsorbed phase.
- 3.2. Creation of electron-hole pairs which dissociate into photoelectrons and positive photo-holes (electron vacancies).
- 3.3. Electron transfer reactions such as ion sorption (case of  $O_2$ ,  $NO$ , etc.), charge neutralization, radical formation, surface reactions...

In the presence of a fluid phase (gas or liquid), a spontaneous adsorption occurs and according to the redox potential (or energy level) of each adsorbate, an electron transfer proceeds towards acceptor molecules, whereas a positive photohole is transferred to a donor molecule (actually the hole transfer corresponds to the cession of an electron by the donor to the solid):

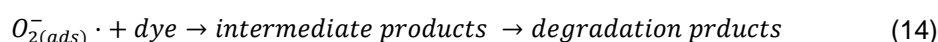
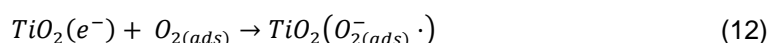
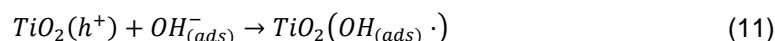
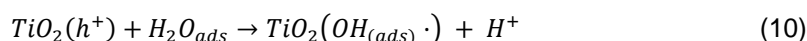


Then, each ion formed reacts to form the intermediates and final products. That is why the photonic excitation of the catalyst appears as the initial step of the activation of the whole catalytic system. Several authors ([92–95]) studied the influence of various parameters that affect the photocatalysis process and, in general, the most influential parameters for the reaction rate turned out to be the mass of the catalyst, the wavelength of the incident wave, the initial concentration, the temperature, the radiant flux, the quantum yield and in some cases the oxygen pressure.

### 2.3.2. Methylene blue degradation as a technique to measure the photocatalytic activity

Measuring the degradation rate of a dye dissolved in a solution allows the evaluation of the photocatalytic activity in an aqueous system. Methylene blue (MB) has been used as such a dye because it shows less absorption at the absorption band (~380-420 nm) of anatase and rutile TiO<sub>2</sub> and is relatively stable against UV irradiation [96]. However, MB has still been reported to be photobleached, demethylated, and photodegraded without any photocatalysts and under visible light irradiation. Similar reactions have been studied to occur in TiO<sub>2</sub> photocatalytic reactions under UV irradiation.

The mechanism and the different steps of this reaction were studied by different authors. When an aqueous solution is irradiated in the presence of TiO<sub>2</sub> photocatalyst, the adsorbed water molecules react with the holes in the valence band to form hydroxyl radicals and release hydrogen ions which attack the dye molecules. After this step, organic acids as the intermediate products are formed by the decomposition of the dye molecules. According to several studies, the adsorption of methylene blue onto the TiO<sub>2</sub> surface is considered the first step in the reaction mechanism. Hydroxyl and superoxide radicals are generated by the excitation of the oxide and decompose the adsorbed methylene blue. Therefore, the reaction steps of methylene blue decomposition can be summarized as follows [97]:



According to *Wu et.al.* [97], (8) represents the reversible adsorption step of the dye molecules onto the TiO<sub>2</sub> surface. (9) to (12) constitute the reaction network of the OH free radical and superoxide free radical formation. The OH free radical and the superoxide free radical will attack the preadsorbed dye compound as shown in (13) and (14), respectively.

Several authors analyzed the MB photodegradation process in the presence of TiO<sub>2</sub> and analyzed the reaction kinetics and the degradation values reached under different conditions. The effects of the initial concentration of methylene blue, the amount of catalyst and the pH of the solution, are the most important parameters on the decomposition efficiency of TiO<sub>2</sub> [98]. The illustration of the reaction mechanism from the initial step of adsorption involving the cationic functional group of MB molecule, until the formation of final products (CO<sub>2</sub>, SO<sub>4</sub><sup>2-</sup>, NH<sub>4</sub><sup>+</sup> and NO<sub>3</sub><sup>-</sup>), passing through several intermediate compounds (analyzed by GC/MS and LC/MS), can be observed in Figure 7 [99].

Changes in the concentration of MB are correlated with the color intensity of the solution, so the variations of the maximal absorption in UV-visible spectra at 660-670 nm are commonly used to describe the photodegradation effectiveness of the photocatalytic substance (maximum absorbance value of the spectrum at approximately 664 nm). From the measured absorbance values, the concentration can be estimated to know the degree of degradation obtained at the end of the process. For this, multiple models and equations are used, although due to the limitations of the predictive models, calibration curves that correlate the absorbance and concentration values are made in the working range.



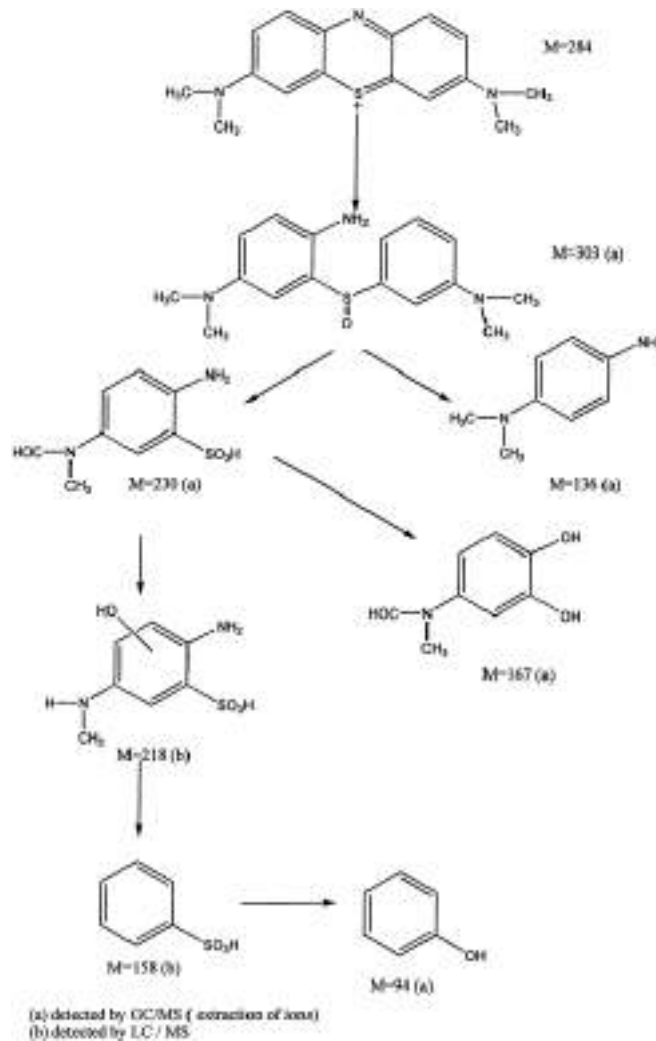


Figure 7 - Photocatalytic degradation pathway of MB [99]

The kinetic of the photocatalytic degradation of MB can be described by the Langmuir–Hinshelwood pseudo-first-order kinetics [100] defined by the equation:

$$-\frac{dC}{dt} = k' * C \quad (15)$$

Where C is the concentration of the dye, t is the time and k' the apparent kinetic constant. This model considers the degradation rate proportional to the concentration of the solution. After integrating the equation (15), the temporal evolution of the concentration (C<sub>t</sub>) is:

$$C_f = C_0 e^{-k't} \quad (16)$$

And the kinetic constant can be calculated with the expression:

$$k' = \frac{1}{t} \ln \left( \frac{C_0}{C_f} \right) \quad (17)$$

Methylene blue degradation presents a relatively simple technique that can give quantitative and qualitative results of the photocatalytic properties of semiconductors, using relatively simple equipment and without representing a destructive technique for the samples (in some cases, the effects of cycling and repetition of steps are studied).

### 2.3.3. Strategies for improving photocatalytic activity

Compared to pure phases, the mixed-phase TiO<sub>2</sub> materials have unique charge transfer and recombination dynamics, fast diffusion of charge carriers to the surface, or an interface that enhances the interfacial charge transfer processes [101–103]. Generally, a better photocatalytic performance is attributed to the anatase over the rutile phase. However experimental evidence supports the existence of a synergistic effect in the anatase-rutile bicrystalline phase, which exhibits higher photocatalytic activity compared to their respective pure phases [57,103–106].

The solid-solid interface between the two phases is a key structural feature that facilitates charge separation to suppress recombination [107] and the energetic alignment of the band edges of the rutile and anatase is an important aspect to understand the charge carrier dynamic of the polymorphs junction [105]. There is a longstanding controversy in the energetic alignment of the band edges of the rutile and anatase. Some authors proposed that after Fermi level alignment, the conduction band edge of rutile should be lower than that of anatase, resulting in favorable conditions for electron transfer from anatase to rutile. This is consistent with observations of reduction processes, such as Ag<sup>+</sup> photodeposition, occurring preferentially on rutile domains in mixed-phase TiO<sub>2</sub> photocatalysts [108,109]. For example, *Kawahara et al.* [108] show in Figure 8 a scanning electron microscopy image (a) for a patterned anatase-rutile interface after Ag photodeposition. The accompanying X-ray emission spectrum (b) shows that Ag was preferentially deposited on the rutile half of the interface.

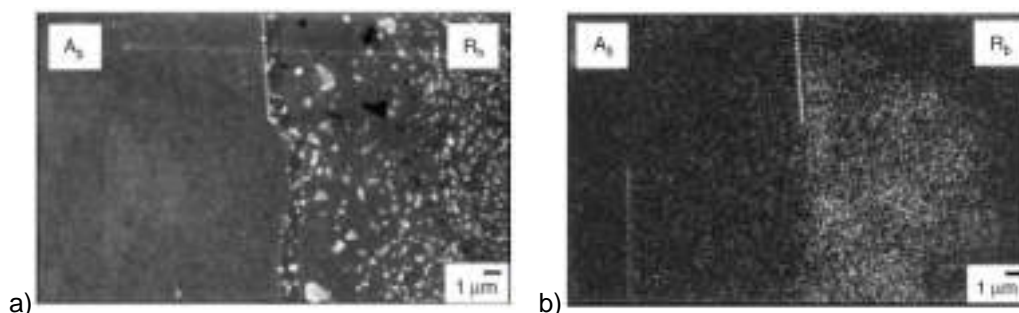


Figure 8 - a) SEM micrograph and b) X-ray emission image for Ag from the same boundary region between anatase and rutile after photoreductive deposition of Ag. The dashed line marks the boundary [108].

In contrast, other groups have proposed that electrons in the conduction band of rutile are transferred to anatase. It is proposed that the key issue is the energy of electron trap sites and not the positions of the band edges. The electron trap sites can be more stable on anatase, resulting in greater stabilization of electron transfer from rutile to anatase. These results may be in agreement with the band alignment of 0.4 eV existing between anatase and rutile with anatase possessing the higher electron affinity [105]. The interfacial region between anatase and rutile can also act as charge trapping sites, facilitating charge separation. Other groups have proposed that the interfacial region has slightly modified optical properties compared to those of the pure phases, enabling photoactivity with sub-bandgap light [106]. The nature of the atomic-level contact between anatase and rutile that facilitates enhanced charge separation is not still well understood [110–112].

The more extensively studied form of TiO<sub>2</sub> is that of a particle. However, there is no direct correlation between the surface quality of particles and activity due to the inherent difficulty to characterize particles from the surface because of the degree of heterogeneity. Particle shape and size are important variables to be considered. Some studies suggest that an activity–shape relationship translates into an activity–facet relationship. Specific surface facets exposed to the medium show higher photocatalytic activity. On the other hand, changes in particle size influence photoactivity through changes in surface area, light scattering and light absorptivity [106].

The degree of surface crystallinity has a significant influence on TiO<sub>2</sub> photocatalytic activity in materials such as nanoparticles, thin films, mesoporous networks, nanotubes and rods, and sol-gels. A higher degree of crystallinity implies an improvement in the photocatalytic activity. Purely amorphous TiO<sub>2</sub> is photo-inactive irrespective of its surface OH population or surface area. The improvement of

photocatalytic performance with increased crystallinity is generally attributed to the removal of dangling bonds and distorted lattice structures that act as charge trapping and/or recombination sites. [106].

Besides the thoroughly studied TiO<sub>2</sub> polymorphs rutile and anatase, some works explore the photocatalytic activity of other titania phases [113,114]. Ti<sub>2</sub>O<sub>3</sub> with a quasi-metallic phase is one of the most important Ti<sub>n</sub>O<sub>2n-1</sub> oxides with relatively large electronic conductivity and chemical stability compared to the typical TiO<sub>2</sub> owing to the absence of O atoms in every layer. An improvement in the photocatalytic activity of Ti<sub>2</sub>O<sub>3</sub>/TiO<sub>2</sub> heterophase junctions compare to the individual activity of Ti<sub>2</sub>O<sub>3</sub> and rutile TiO<sub>2</sub> is also possible by combination of these two phases [115]. This higher photoactivity could be attributed to the enhanced charge separation in the formed heterophase junctions in which Ti<sub>2</sub>O<sub>3</sub> with low work function acts as a sink to trap photoelectrons from TiO<sub>2</sub>.

To extend the spectral response of TiO<sub>2</sub> into the visible region and to enhance its photocatalytic activity, several strategies have been developed. Doping pure TiO<sub>2</sub> with either anions or cations is one way for sensitizing TiO<sub>2</sub> to visible light. This route makes it possible to use the main part of the solar spectrum and also to ensure the charge traps to keep electrons and holes separate [116]. However, the doped TiO<sub>2</sub> can undergo self-degradation with the course of photocatalytic reaction. In some cases, the oxygen vacancies created by doping, can also promote the electron–hole recombination process [117].

### 2.3.4. Applications

Photocatalysis applications are mainly focused on the areas of power generation and environmental sanitation, due to their high capacity for generating complex chemical reactions without the need for large reactors, without the use of chemical agents and using simple configurations or set-ups. The development of new materials, however, is strongly required to provide enhanced performances with respect to the photocatalytic properties and to find new uses for TiO<sub>2</sub> photocatalysis. Table 2 summarizes and categorizes the main applications of TiO<sub>2</sub> as a photocatalyst, according to the property involved:

Property	Category	Application
Self-cleaning	Materials for residential and office buildings	Exterior tiles, kitchen and bathroom components, interior furnishings, plastic surfaces, aluminium siding, building stone and curtains, paper window blinds.
	Indoor and outdoor lamps and related systems	Translucent paper for indoor lamp covers, coatings on fluorescent lamps and highway tunnel lamp cover glass
	Materials for roads	Tunnel wall, soundproofed wall, traffic signs and reflectors
	Others	Tent material, cloth for hospital garments and uniforms and spray coatings for cars
Air cleaning	Indoor air cleaners	Room air cleaner, photocatalyst-equipped air conditioners and interior air cleaner for factories
	Outdoor air purifiers	Concrete for highways, roadways and footpaths, tunnel walls, soundproof walls and building walls
Water purification	Drinking water	River water, ground water, lakes and water-storage tanks
	Others	Fish feeding tanks, drainage water and industrial wastewater
Antitumor activity	Cancer therapy	Endoscopic-like instruments
Self-sterelizing	Hospital	Tiles to cover the floor and walls of operating rooms, silicone rubber for medical catheters and hospital garments and uniforms
	Others	Public rest rooms, bathrooms and rat breeding rooms

Table 2 - Applications of photocatalysis [93]

Some other applications for photocatalysis materials (TiO<sub>2</sub> and others) are: polyphasic (solar) photoreactors [92], electrochemical photolysis of water [118], photoelectrocatalytic reduction of carbon dioxide [119] and removal of pollutants and bacteria [120–128].

### 3. Materials and methods

#### 3.1. Sample preparation

Titanium sheets of 1 mm thick and a 5x5 mm<sup>2</sup> surface area with 99.995% purity were used as samples. To achieve a proper homogeneous surface to irradiate with the laser source, the following procedure was carried out (see Table 3):

Step	Material	Specifications	Duration
Grinding*	SiC sandpaper #1200 grain size 15 µm	Force 6,8 N/cm <sup>2</sup> . Plate speed: 300 rpm Holder speed: same direction 150 rpm	5 min
Polishing	OP-S NonDry (Struers) + 2%V/V NH <sub>3</sub> (25%) + 2%V/V H <sub>2</sub> O <sub>2</sub> (100 volumes) Polishing pad: MD Chem Struers 250 mm	Force 6,8 N/cm <sup>2</sup> at 150 rpm Plate speed: 150 rpm Holder speed: same direction 150 rpm	8 min
Cleaning	Water with detergent in ultrasonic bath		5-10 min
Etching	Beraha I stock solution	The reaction is stopped by sample immersion in water	45 s
Polishing	Idem	Idem	8 min
Cleaning	Water with detergent in ultrasonic bath		5-10 min

\* The edges were also manually rounded with #1200 grinding paper

*Table 3 - Sample preparation procedure*

A TegraPol-21 from Struers was used for carrying out the grinding and polishing steps. The samples were rinsed with deionized water after the last cleaning step, then cleaned thoroughly with ethanol and dried with compressed air taking special care not to touch the polished side to avoid producing scratches. Plastic tweezers were used throughout the procedure for handling.

The objective of this procedure is to achieve a homogeneous surface with little surface plastic deformation to have a similar absorption of laser radiation over the entire surface.

#### 3.2. Laser structuring

##### 3.2.1. Picosecond laser

The laser generator relies on an Edgewave InnoSlab PX with a pulse FWHM (full width at half maximum) of 12 ps, a final wavelength of 532 nm and a maximum power of ca. 10 W. The active medium of the amplifier consists of a thin sheet of Nd:YAG crystal that is sandwiched between two copper coolers. The whole laser consists of a passively mode-locked seed laser that produces pulses with a repetition rate of 50 MHz. A pulse picker reduces this repetition rate to 100 kHz before the pulses reach the amplifier (see Figure 9). Behind the amplifier, another optoacoustic modulator functions as a gate and regulates the final pulse frequency and power. In a last step, a frequency converter converts the 1064 nm to green 532 nm radiation [129].

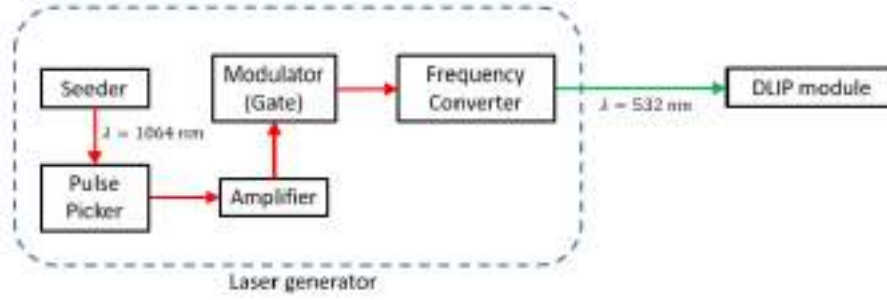


Figure 9 - Schematic structure of the Picosecond Laser generation [42]

To generate a line-like pattern, two superimposed coherent beams are overlapped on the surface. The laser setup used in this work is shown schematically in Figure 10:

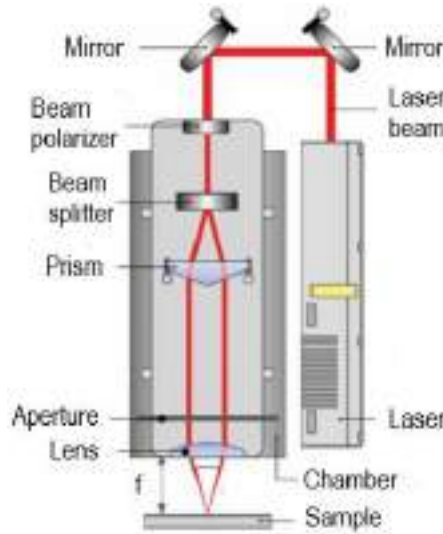


Figure 10 - DLIP laser beam setup [42]

The laser is guided from the generator by mirrors to the DLIP unit. After passing the polarizer (make polarization perpendicular to the pattern and the LIPSS therefore parallel), the beam is split into four equally intensive sub-beams by a diffractive beam splitter (DOE). Behind it, a prism is used to parallelize the sub-beams in the vertical direction. Depending on the position of the prism (distance from the splitter), the beams can be parallelized immediately after hitting the DOE resulting in a small distance between the beams or they can be parallelized much later leading to a high beam distance. Before the beams hit the lens, an aperture can be inserted to block unwanted beams. This way interference of only 2 or 3 beams can be achieved. As the beams are close to parallel when they hit the lens they are overlapped (focused) approximately at the focal length of the lens. Therefore, the interference angle is defined by the beam distance (given by the prism position) and the focal length of the used lens. The geometrical relation between the periodicity and the interference angle is given by:

$$P = \frac{\lambda}{2 \cdot \sin\theta} \quad (18)$$

Where  $\lambda$  is the wavelength and  $\theta$  is the glancing angle (angle formed between one beam and the surface normal) [51]. The used lens thereby defines a range of possible pattern periodicities where the smaller focal length (40 mm) can produce the smallest structures (<1  $\mu\text{m}$ ) and the 100 mm lens the biggest ones (up to 10  $\mu\text{m}$ ). In this work, the 100 mm focal length lens was used, and structures of 10  $\mu\text{m}$  periodicity were developed with different intensities of laser pulses, as will be explained in the next section.

As it was already explained, an aperture can be inserted to block unwanted beams on the path, right after the beams are split and before they hit the lens. Without any kind of obstacle, the original 4 beams

can interfere at the surface and make a points pattern (as it was explained in Section 2.1.6). In this work, line-like structures are desired, so a mask is installed to block the path of two opposite beams. In the next section, the interference phenomenon of two beams and the resulting line pattern will be illustrated. Is important to mention that this implementation results in the disadvantage of reducing half the laser power (have of the beams are not interacting with the surface).

### 3.2.2. Surface patterning

In this work, a device manufactured by Fraunhofer IWS with a laser and a DLIP module was used, as described above. A vacuum system was placed near the processing area during processing to avoid covering the lens with the ejected material. To produce a homogeneously patterned surface, it is necessary to overlap the rounded spots of each pulse in a convenient way. To do so the sample was translated using motorized linear stages in x and y directions and moved in a way that ensures the partial overlap of the single spots in both translational directions as shown in Figure 11.

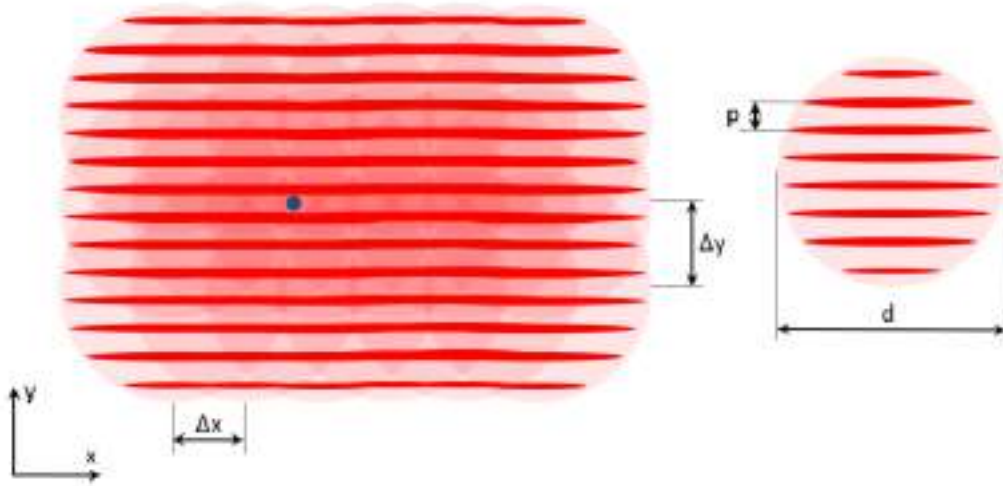


Figure 11 - Overlap of laser spots to achieve homogenous coverage. The total number of pulses that interact with the blue dot is defined by the spot diameter and the step sizes  $\Delta x$  and  $\Delta y$  [42].

The translation in the direction y ( $\Delta y$ ) should be a multiple of the periodicity, in this way the location of the maxima of the first line of shots matches with the maximums of the next line. The distance between spots in the x-direction ( $\Delta x$ ) is related to the repetition rate ( $f$ ) and the stage speed in the direction x ( $v_x$ ) as follows:

$$\Delta x = \frac{v_x}{f} \quad (19)$$

The energy  $E_p$  of each pulse for a given operating power  $P$  is:

$$E_p = \frac{P}{f} \quad (20)$$

The fluence per pulse ( $F_p$ ), meaning the energy delivered per unit of planar area, is the energy per pulse divided by the area of the spot, hence:

$$F_p = \frac{E_p}{\left(\frac{\pi \cdot d^2}{4}\right)} = \frac{4 \cdot P}{\pi \cdot d^2 \cdot f} \quad (21)$$

Where  $d$  is the spot diameter. Now if the surface to be processed is considered as a rectangle of  $x$  and  $y$  dimensions, the total energy applied to the whole surface is the sum of the individual contribution of each spot. If the dimensions  $x$  and  $y$  are much larger than the spot diameter, then the total energy  $E_{total}$  can be calculated as:

$$E_{total} = E_p \cdot n_{total} = E_p \frac{x}{\Delta x} \frac{y}{\Delta y} \quad (22)$$

Where  $n_{total}$  is the total amount of spots distributed on the entire surface. The specific energy applied per unit of area defined as accumulated fluence ( $F_{acc}$ ) is simply:

$$F_{acc} = \frac{E_{total}}{x \cdot y} = \frac{E_p}{\Delta x \cdot \Delta y} \quad (23)$$

It should be noted that this parameter does not depend on the diameter of the spot. The number of pulses per point ( $n_{acc}$ ), tells how many pulses interact with one fixed point on the surface. Figure 11 represents how many circles are overlapped in the blue dot. It thereby defines if the accumulated fluence is delivered by a few very strong pulses or many weak ones. This number is given by:

$$n_{acc} = \frac{F_{acc}}{F_p} \quad (24)$$

The laser parameters interesting for this work (the input parameters that can be set are distinguished from that output that are the response of the input) are:

- Periodicity: input parameter (DOE position can be set and thereby the periodicity can be controlled).
- Translation in the direction  $y$  ( $\Delta y$ ) and  $x$  ( $\Delta x$ ): input parameter.
- Operating power ( $P$ ) and pulse energy ( $E_p$ ): input parameter.
- Accumulated fluence ( $F_{acc}$ ) and pulse fluence ( $F_p$ ): output parameter.
- Number of pulses per point ( $n_{acc}$ ): output parameter.

In this work, the influence of the accumulated fluence ( $F_{acc}$ ) and the number of pulses per point ( $n_{acc}$ ) on the surface properties of the samples will be studied. This is based on previous work [42,130–133].

### 3.2.3. Parameters used

Two kinds of structures were patterned for this work: line-like structures (L) and cross-like structures (C). Line-like structures can be produced by the interaction of two beams, as it was explained in a previous section (Section 2.1.6). Cross-like structures are produced by the overlap of two line-like structures with a  $90^\circ$  rotation of the sample between each patterning step. As a defined value of  $F_{acc}$  and  $n_{acc}$  are desired, each patterning step (with a line-like structure) should involve half of this values. For example, for a sample with cross patterning, irradiated  $100 \text{ J/cm}^2$   $F_{acc}$  and  $330$   $n_{acc}$ , two patterning steps should be conducted, with a  $90^\circ$  rotation in between, with an accumulated fluence value of  $50 \text{ J/cm}^2$  and  $165$  pulses per point. This cross-like patterns have the deepest point in the intersections of the perpendicular lines.

Table 4 shows the sample parameters used for this work, giving information about the morphology, pulse energy, accumulated fluence, number of pulses per point and the reference name. The nomenclature used to name each sample is composed of a letter that describes if it is a line-like pattern (L) or a cross-like pattern (C). Then the value of the accumulated fluence ( $F_{acc}$ ) is given in  $\text{J/cm}^2$  and finally the number of pulses ( $n_{acc}$ ). For example, C-500-3500 is a cross-structured sample with an accumulated fluence of  $500 \text{ J/cm}^2$  and an amount of  $3500$  pulses per point.

Morphology	Pulse energy ( $\mu\text{J}$ )	Accumulated fluence ( $\text{J}/\text{cm}^2$ )	Number of pulses per point	Name
Line-structure	10	100	700	L-100-700
		500	3500	L-500-3500
		750	5250	L-750-5250
		1000	7000	L-1000-7000
	30	100	330	L-100-330
		500	1650	L-500-1650
		750	2475	L-750-2475
		1000	3300	L-1000-3300
Cross-structure	10	100 (50 + 50)	700	C-100-700
		500 (250 + 250)	3500	C-500-3500
		750 (375 + 375)	5250	C-750-5250
		1000 (500 + 500)	7000	C-1000-7000
	30	100 (50 + 50)	330	C-100-330
		500 (250 + 250)	1650	C-500-1650
		750 (375 + 375)	2475	C-750-2475
		1000 (500 + 500)	3300	C-1000-3300

Table 4 - Laser parameters and reference name.

It is important to mention that three of the line structures with a pulse energy of  $10 \mu\text{J}$  (structures with many weak pulses) are highlighted in red, because they could not be completely characterized. The samples were first produced and studied in the same conditions as the other samples, but after some analysis of the results, an unexpected behavior of the surface was observed. An increase of the accumulated fluence caused a decrease in the surface patterning depth, in opposition to the other samples which followed the expected trend as it will be explained in the next section. After observation of this results, the problem was analyzed and the cause was found. Nevertheless, the time available to perform the tests was not enough to do a complete study of the samples and it will be part of future work on this subject.

The problem with the sample processing was related to the repetition rate of the equipment (how many pulses were produced in a determined time). To achieve the desired accumulated fluence with this value of pulse energy ( $10 \mu\text{J}$ ), the value of the repetition rate ( $f$ ) was increased above the maximum value allowed by the equipment ( $100 \text{ kHz}$ ). As the software did not give an indication of this excess in the parameter value, this problem was not detected during the structuring of the surface, but just after the surface characterization. After considering this parameter limitation, new samples with lowest values of repetition rate were produced, keeping the same parameters values for  $F_{\text{acc}}$  and  $n_{\text{acc}}$ .

In addition to the study of the influence of these parameters, another study of the efficiency of the patterned samples was carried out. The preparation and cleaning methods of the samples, before and after the patterning of the surface, were studied in previous work [42] and implemented in this case to achieve homogeneous and clean surfaces. Despite this, an attempt was made to clean a sample after structure formation by laser irradiation, where the sample was placed in an ethanol bath and exposed to ultrasound for between 5 and 10 minutes. After this process, the sample showed a visibly brighter and clearly modified surface compared to the sample without the ultrasound bath. For this reason, the influence of this process was also studied in this work, and samples with and without ultrasound bath (after patterning) were characterized by microscopy (topography), XRD (composition) and methylene blue degradation (photocatalytic activity). The results of this analysis will give some information about the stability and resistance of the oxidized surface when exposed to mechanical stresses due to ultrasound waves.



### 3.3. Characterization

#### 3.3.1. Confocal laser scanning microscopy (CLSM)

Characterization of the surface topography was performed by means of confocal laser scanning microscopy (CLSM) utilizing a LEXT OLS4100 3D Measuring Laser Microscope by Olympus. The parameters of interest were measured to characterize the morphology and topology of the treated surfaces. This equipment achieves a lateral and height resolutions of 0,12  $\mu\text{m}$  and 10 nm respectively [134]. The light in the laser mode is generated by a semiconductor laser with a wavelength of 405 nm. The measurements were done using the 50X and 20X objectives.

The CLSM is a combined optical imaging microscope that uses an array of optical lenses and spot scanning by a monochromatic laser beam. Capturing multiple two-dimensional images at different depths in a sample enables the reconstruction of three-dimensional structures within an object. This process is known as optical sectioning. CLSM expands the possibilities of simple optical microscopes while it does not require prior surface preparation and is not as limited in terms of scanning range as scanning electron microscopy (SEM). To characterize the topography of the structured surface the following parameters will be used according with the standard DIN EN 4288:

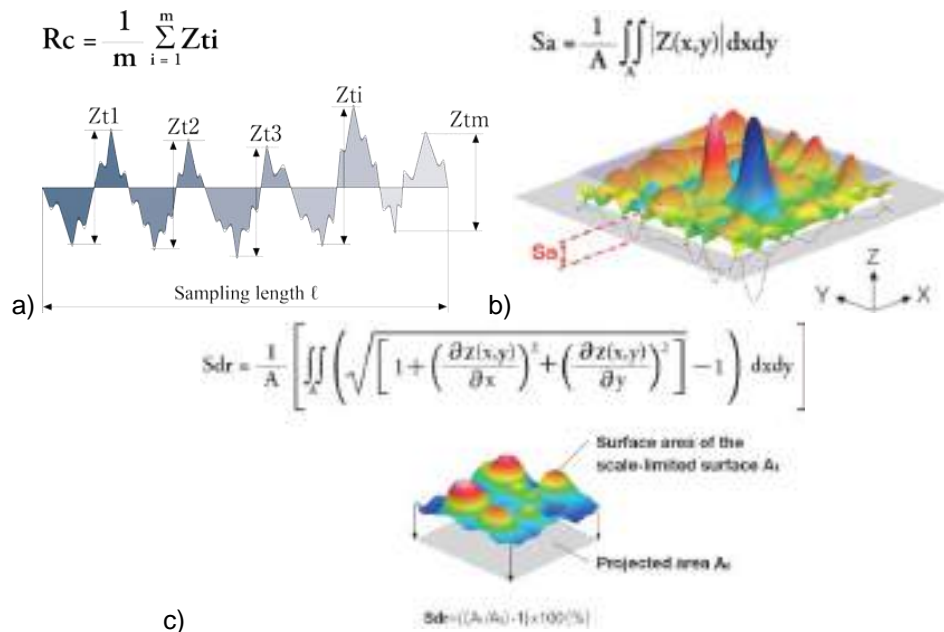


Figure 12 - Roughness parameter used to describe the surface structured patterns. a) Mean height ( $R_c$ ); b) Arithmetical mean height ( $S_a$ ); c) Roughness ratio (S-ratio)

- **Mean height ( $R_c$ ):** Represents the mean for the height  $Z_t$  (Figure 12a) of profile elements within the sampling length. This value gives the average height difference between valleys and peaks.
- **Arithmetical mean height ( $S_a$ ):** This parameter expands the profile (line roughness) parameter  $R_c$  two-dimensionally (Figure 12b). It represents the arithmetic mean of the ordinate  $Z(x, y)$  within the evaluation area.
- **Roughness ratio (S-ratio):** The roughness ratio is defined as the ratio between the actual and projected solid surface area (Figure 12c). Therefore, it is 1 for a completely smooth surface and  $>1$  for a rough one.

For the line-like pattern, the mean height is taken in the direction perpendicular to the structure. For the cross-like pattern, the measurement direction is at an angle of  $45^\circ$  with respect to the direction of the lines, so the mean height between the lowest and highest points is measured.

### 3.3.2. Methylene blue degradation

The aim of this measurement is to describe quantitatively the degradation capability of the oxidized surface by measuring the change in the absorption of light in the exposed solution and calculating the correspondent change in its solute concentration. After performing the patterning on the surface of the samples, they were placed in a sample holder with square units and submerged in a solution of methylene blue (MB) of known initial concentration. A commercial UV light chamber was used to irradiate the samples, which were exposed to this lamp at room temperature and using a petri dish to avoid changes in concentration due to evaporation. The UV lamp device has 4 fluorescent lamps with a total power of 36 W from Nailstar (model NS-01-UK&EU) and 365 nm of wavelength. This experimental set up was developed and studied in [42], for which the 2-hour exposure time used in other works was maintained.

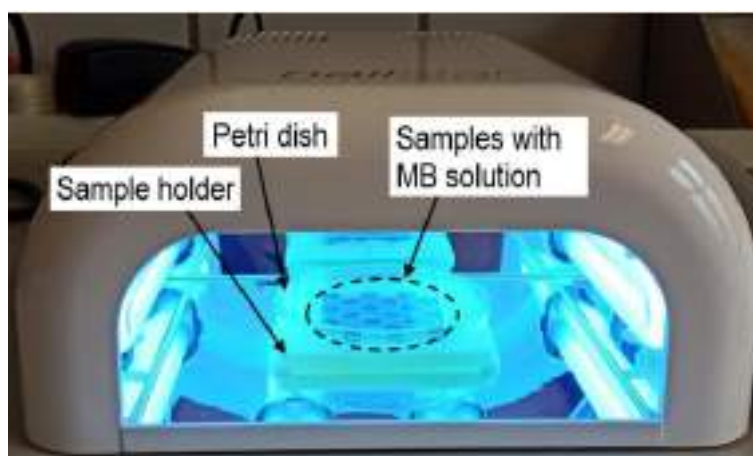


Figure 13 - Experimental set up implemented for performing the methylene blue degradation [42]

The UV/Vis/NIR spectra were recorded on a Perkin Elmer Lambda 750 spectrophotometer in a range of 600–700 nm (with acquisition steps of 4 nm) using disposable UV micro cuvettes from Brand with 10 mm of path length and a capacity from 70  $\mu\text{l}$  to 850  $\mu\text{l}$ . 125  $\mu\text{l}$  of a 50  $\mu\text{M}$  (initial concentration) MB were used to fill each unit of the plastic grid. After exposure for 120 minutes, 90  $\mu\text{l}$  of solution were extracted and poured on plastic transparent cuvettes. Finally, the samples were diluted with 160  $\mu\text{l}$  of deionized water (total volume inside the cuvette of 250  $\mu\text{l}$ ). The absorption value for the calculations was taken at 664 nm. The MB solution preparation and UV experiments were performed the day before the measurements to avoid undesirable aging effects. In addition, different solutions of known concentration were analyzed in the equipment, to correlate the characteristic absorbance values for the different concentration values, thus creating a calibration curve (concentrations of 5 to 50  $\mu\text{M}$  were used).

### 3.3.3. Scanning electron microscopy (SEM)

A scanning electron microscope uses a focused electron beam to depict the sample topography and chemistry. The electrons thereby originate from a tungsten or field emission cathode and are accelerated towards the sample surface by an acceleration voltage. The resulting electron beam is then focused with magnetic lenses and interacts with the sample material electrostatically (atom cores) or through collisions (electrons). Secondary electrons, backscattered electrons and characteristic X-ray are produced from the interaction of the primary electron beam with the sample.

For this work, a Helios NanoLab™ 600 FIB/SEM was used, equipped with a high-resolution electron column with a Field Emission Gun (FEG) electron source. It also provides with a Ga<sup>+</sup> ion source that can image and machine down to 5 nm resolution levels. The accelerating voltage was set to 5 kV for this work.

### 3.3.4. Focused ion beam (FIB)

The Ga<sup>+</sup> ion source of the Helios NanoLab™ 600 was used to steadily and precisely remove material from the surface to achieve a transversal cut of the sample. This section was analyzed after the removal of some μm, so the patterns can be observed with more accuracy and better resolution. The effects of laser irradiation on the material below the surface are also observed by analyzing the cross section of the surface.

### 3.3.5. Grazing incidence X-ray diffraction (GI-XRD)

X-ray diffraction is a non-destructive technique that gives information about the crystallographic structure, chemical composition, and physical properties of materials. This technique is based on the interaction between energetic photons and the atoms in a periodic lattice of the sample. The elastic scattering of a monochromatic and collimated X-ray beam causes an interference pattern by destructive and constructive interference. The positions of the interference maxima are described by the Bragg's law:

$$n\lambda = 2d \cdot \sin \theta \quad (25)$$

Here  $d$  is the spacing between diffracting planes,  $\theta$  is the angle between the incident beam and the normal to the reflecting lattice plane (called incident angle),  $n$  is any integer, and  $\lambda$  is the wavelength of the beam.

Grazing incidence X-ray diffraction is a scattering geometry technique combining the Bragg condition with the conditions for X-ray total external reflection from crystal surfaces. This provides superior characteristics of grazing-incidence diffraction as compared to the other diffraction schemes in the studies of thin surface layers, since the penetration depth of X-rays inside the slab is reduced by three orders of magnitude than the conventional Bragg diffraction. The signal comes typically from the first 1-10 μm material underneath the surface and in grazing-incidence diffraction it is reduced to 1-10 nm or even less.

To unravel the chemical nature of the thin oxide layer produced by the laser processing, measurements were performed by grazing-incidence X-Ray diffraction with a PANalytical X'Pert Pro MPD diffractometer with copper K<sub>α</sub> radiation, 40 kV and 40 mA. The incidence angle was set at 0.8° in a 2θ from 25° to 75° with a 0.05° step. To avoid the shadowing effect due to the pattern structure and to characterize both peaks and valleys, the samples were placed with the pattern direction parallel to the incident beam.

## 4. Results and analysis

As it was explained in the previous chapter, the topography of the surface of the samples was characterized by FIB-SEM images (top surface and transversal area), but also by CLSM (roughness parameters). The surface chemistry was studied using GI-XRD and the photocatalytic activity (effectivity of the surface treatment) was analyzed from the MB degradation experiment. This section shows some results which may be relevant for this study and the respective analysis is carried out. Additional results are shown on the Appendix for a more detailed comprehension.

### 4.1. Topography and morphology characterization

#### 4.1.1. Correlation between laser power and spot diameter

As it was explained in the last sections, the values of  $\Delta x$ ,  $\Delta y$  and operating power  $P$  (or pulse energy  $E_p$ ) are input values on the laser which can determine the final values of the accumulated fluence ( $F_{acc}$ ) and the number of pulses per point ( $n_{acc}$ ) (see equations (19) - (24)). The other parameter that must be known to calculate and set up the laser, is the spot diameter ( $d$ ). The size of the spot must be measured, so the other parameters can be calculated. For this reason, the study of the influence of the laser power  $P$  on the spot diameter was carried out for 4 different structures: 3 and 10  $\mu\text{m}$  periodicity for points and lines patterns (points pattern is achieved for the interference of four beams in this case, and line patterns are produced for the interaction of two beams, as it was explained in Section 2.1.6). For this work, only the correlation for line patterns with 10  $\mu\text{m}$  periodicity was used.

Different values of  $P$  between 0,5 and 4 Watts were used as input parameters to structure spots on the surface of titanium samples (the accumulated number of pulses was also checked and there was no influence of this parameter on the spot diameter, so all of the measurements were produced with 1000 pulses per point). The spots diameters were then measured using a Confocal Laser Scanning Microscope (CLSM). This microscope has an image analysis software which allows the user to measure distances between points and many other parameters. Using this tool, the spot diameter was measured twice for each spot (the shortest and the longest distance between external points) and these values were averaged. The spot images can be seen in Figure 14 and the measured spot diameters are shown in Appendix 1. After measuring the spot diameters (and consequently the spot area), the results were plotted against the power ( $P$  vs  $d$ ), and a polynomial regression was calculated (Appendix 1). This regression allows the future users of the laser the possibility of use the laser without the need of measure diameters again.

The resulting plot of  $P$  vs  $d$  on Appendix 1 shows that the spot diameter grows as the power value increases and it is not exactly a linear growth. The resulting curve shows that for low powers, the spot diameter varies significantly with small changes in power, while at higher power values (greater than 3 Watts), the value of the spot diameter is more stable. In addition, although the results are not shown in this work, it was also found that the number of pulses per point does not modify the spot diameter, so it only depends on the power value set in the equipment. From the knowledge of these values, the fluence of each pulse can be calculated, knowing the power, frequency and impact area, thus allowing the calculation of the accumulated fluence of several overlapping pulses.

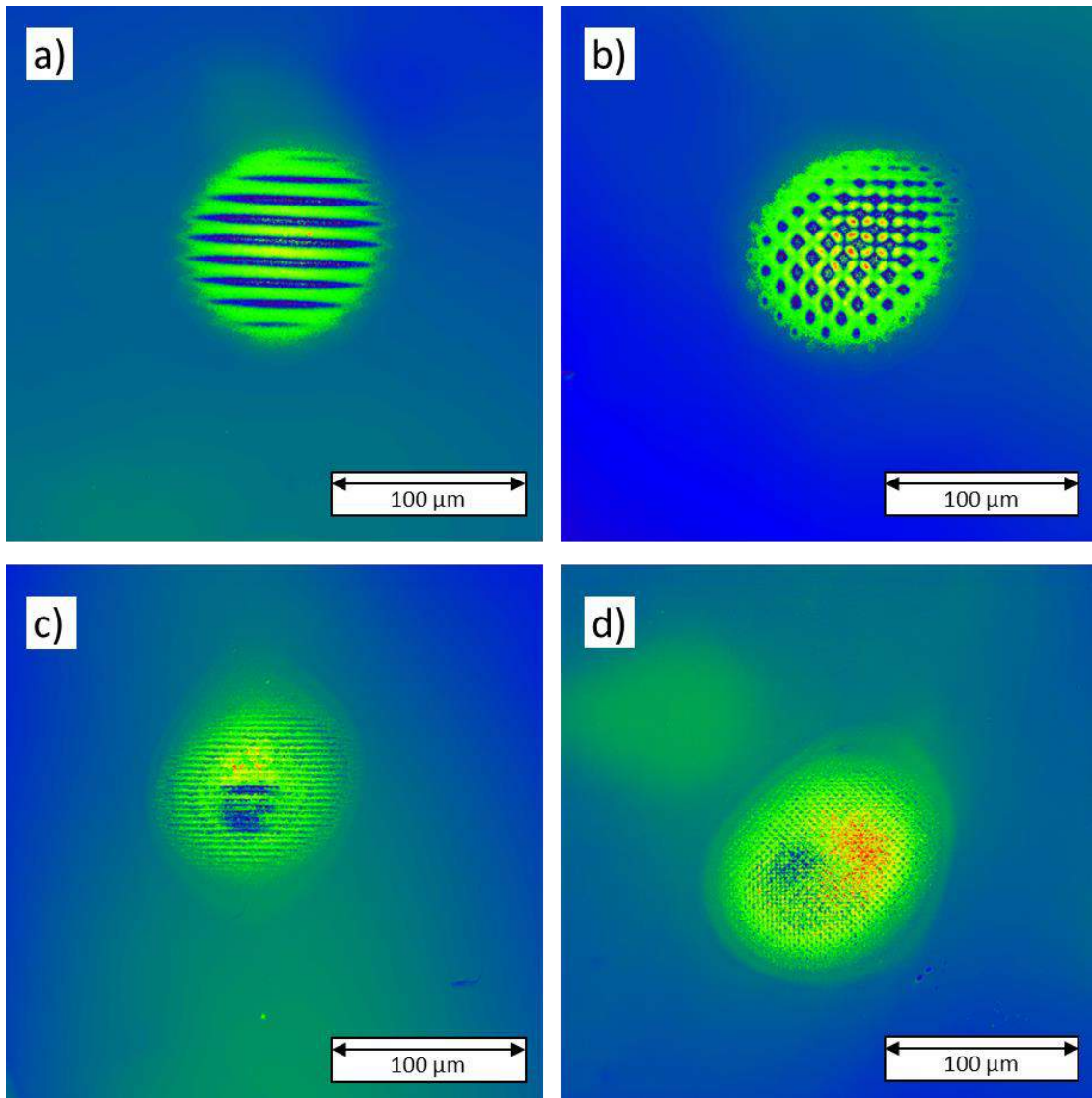


Figure 14 - Laser spots for 1000 pulses with a pulse energy of 10  $\mu\text{J}$  for a) 10  $\mu\text{m}$  lines; b) 10  $\mu\text{m}$  points; c) 3  $\mu\text{m}$  lines and d) 3  $\mu\text{m}$  points.

#### 4.1.2. SEM images

To get a first idea of how the surfaces look after the laser treatment and the consequent oxidation, SEM images of the top surface are shown in Figure 15 to Figure 18. Two images are presented for each sample, at two different magnifications, so that both a general and a detailed view of the surface can be obtained. 1200x and 5000x magnifications were used for line-like pattern images (Figure 15) and 1200x and 10000x magnification were used for cross-like pattern images (Figure 17).

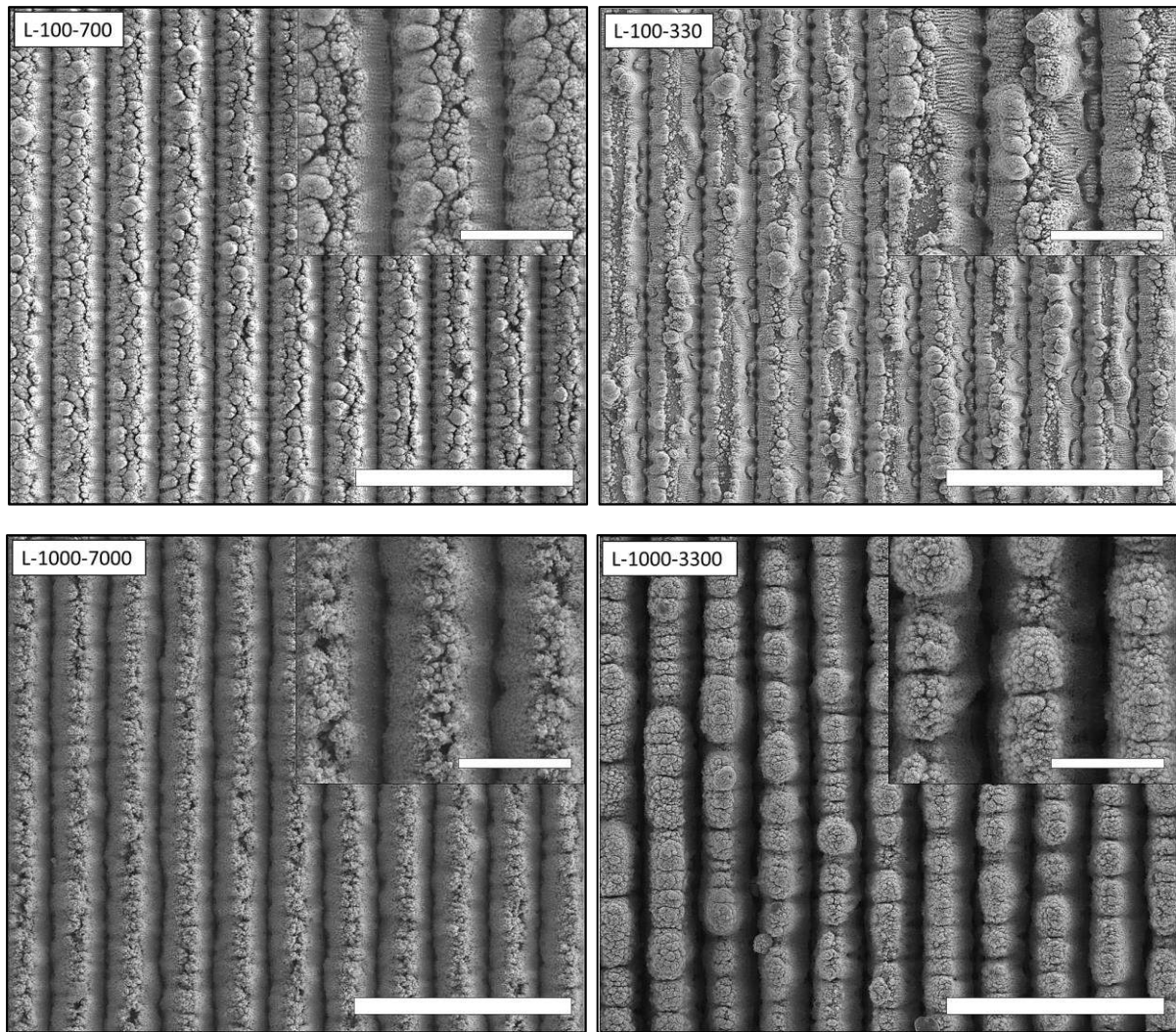


Figure 15 - SEM images of line-like pattern samples for 100 J/cm<sup>2</sup> (above) and 1000 J/cm<sup>2</sup> (below). White bars represent a 40 μm scale and a 10 μm scale for the main picture and the inset, respectively.

Line-like patterns, produced by the interference of two beams, present a clear periodic topography, as can be seen in Figure 15. Samples L-100-700 and L-100-330 are shown above and have the same value of  $F_{acc}$ , but different value of  $n_{acc}$ . Same case is for samples L-1000-700 and L-1000-330 shown below, but with higher value of  $F_{acc}$ . The morphology of the agglomerated oxides seems to be different. An important contrast between the samples on the left (more pulses with less energy) and on the right (a smaller number of pulses but with higher energy) can be observed, especially for the samples with higher accumulated fluence. Samples with higher value of  $n_{acc}$  show a more homogeneous distribution of particles, while samples with lower value of  $n_{acc}$  denote a more disorganized arrangement. Also, samples with higher values of  $F_{acc}$  show a higher concentration of redeposited particles and less distance between them, in comparison with samples with lower  $F_{acc}$ . This clearly denotes a big dependence on the morphology of the sample with the two parameters that were studied in this work: the accumulated fluence and the number of pulses per point.

In every case, a redeposition of the ablated material can be observed. It will be later observed with more detail, that the material is removed from the valleys and redeposited on the peaks, reaching a greater height difference between the lowest point of the valley and the highest point of the peak (in comparison with the distance between the valleys height and the original surface height). This was confirmed in the transversal area images produced by FIB. The redeposited material has a porous morphology and is randomly organized over the surface. Sub-micrometer particles are agglomerated and it is possible to think that the particles could be molten or evaporated during the ultrashort pulse, scattered on the titanium surface and redeposited as oxides.



Figure 16 shows a more detailed view of this morphology and the presence of LIPSS (laser-induced periodic surface structures) can be observed on the sides of the peaks. LIPSS are semi-periodic nanometer- and micrometer-scale structures and, as it was explained in Section 2.1.5, they can be found in materials processed with ultrashort pulse duration lasers. It can be determined in Figure 16 that LIPSS have a separation of around 500 to 1000 nm (they are not completely periodic, but semi-periodic lines). This semi-periodicity depends on the wavelength of the laser (532 nm for this work). The presence of LIPSS involves an additional roughness on the peaks of the samples, which involves an increase on the specific surface area. In addition to this, semi-periodic holes are observed in the valleys, parallel to the pattern direction. These holes have a separation distance of about 2  $\mu\text{m}$  and were observed in most of the samples (except for those where the depth was very high and the valleys surface could not be clearly observed by the SEM microscope). Nevertheless, the formation of these holes is not completely clear and a more detailed study must be carried out in the future work. These holes and the already mentioned LIPSS structures were also observed in other works with ultrashort pulse lasers on titanium surfaces [42].

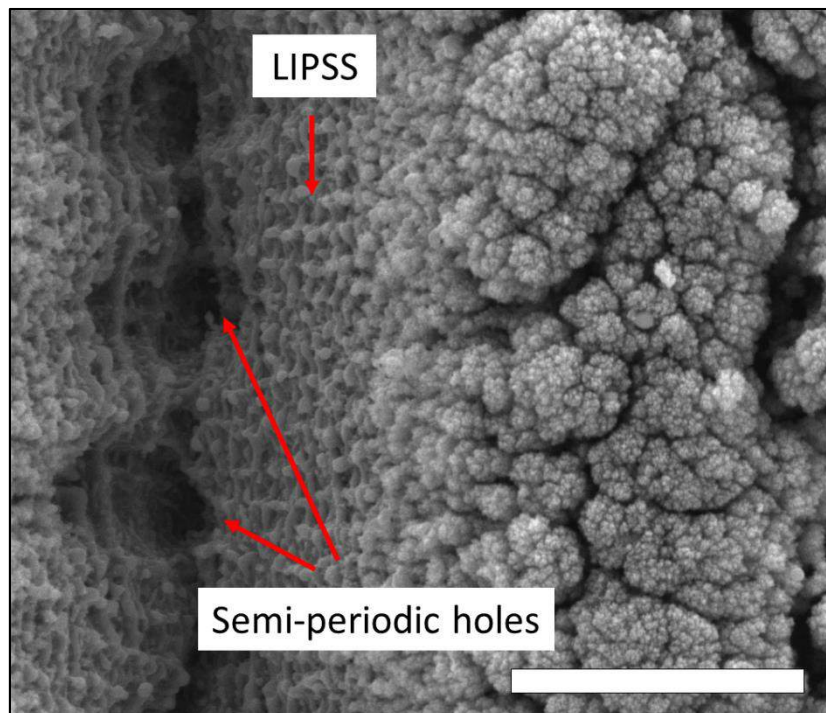


Figure 16 - SEM images of L-100-700 sample with a 15000x magnification. White bar represents a 3  $\mu\text{m}$  scale.

Figure 17 shows the surface of cross-like patterned samples with 100  $\text{J}/\text{cm}^2$  (C-100-700 for many weak pulses and C-100-330 for few stronger pulses) and 1000  $\text{J}/\text{cm}^2$  (C-1000-7000 for many weak pulses and C-1000-3300 for few stronger pulses). The agglomerated particles, resulting from the ablation and redeposition of material, are once again observed in the space between the valleys, as it was for the line structures. The morphology of this particle agglomeration is directly related with the accumulated fluence and the number of pulses per point as it can be seen for the 4 different samples in Figure 17. A complementary study of the chemistry composition of the surface is necessary for a deeper understanding of the different produced structures. As in the previous case of line structures, LIPSS structures can be observed in the zone between the valleys and the peaks. The morphology and geometry of the LIPSS looks like the ones observed in Figure 15 and Figure 16.

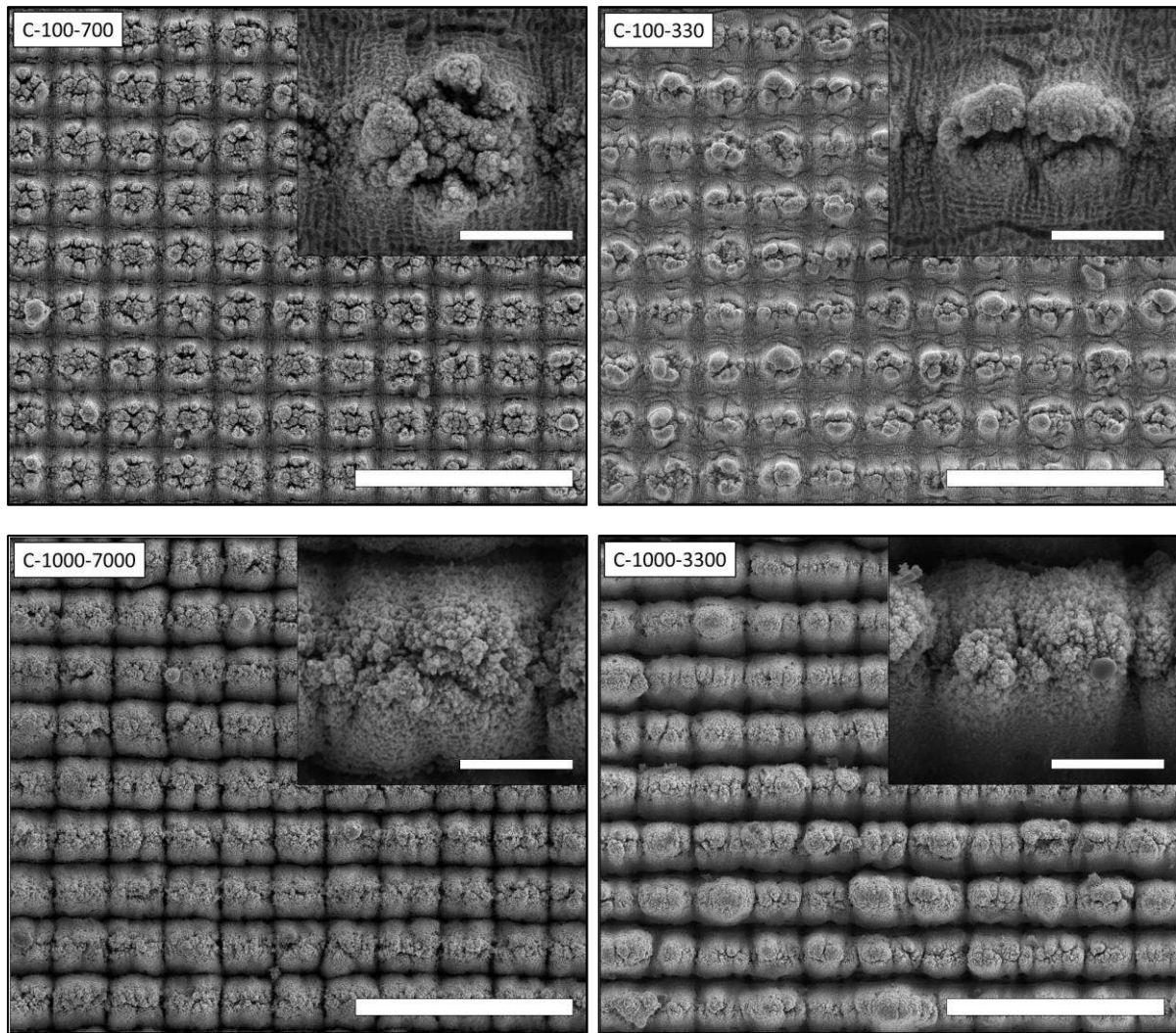


Figure 17 - SEM images of cross-like pattern samples for 100 J/cm<sup>2</sup> (above) and 1000 J/cm<sup>2</sup> (below). White bars represent a 40  $\mu\text{m}$  scale and a 5  $\mu\text{m}$  scale for the main picture and the inset, respectively.

The periodicity in both directions is also clear and easy to see. As it was already explained, the processing of these structures was done in two steps: first, a line-like pattern with 10  $\mu\text{m}$  periodicity but with half of the total fluence was structured; then in a second step, the same pattern was repeated with a 90° rotation, so the other half of the desired energy was irradiated. For the samples shown in Figure 17, the horizontal lines of the pattern are clearer than the vertical ones, as they correspond to the second patterning step. This is better seen in sample C-1000-3300. One important point to mention about this procedure is that the second step is done over an oxidized surface, and not over the pure, polished titanium surface. That means that the absorbance and optical properties are different and the interaction between the laser and the surface is different. It was explained in Section 2.1.1 that the interaction of the irradiated photons and the surface electrons and lattice is very dependent on the material structure and organization. Additionally, the last structured pattern is easier to identify for the samples with high accumulated fluence (C-1000-7000 and C-1000-3300), because the random redeposition of the material on the second step produces an accumulation of oxides over the first produced valleys. Finally, it is also important to note that the deepest points of the surface are the ones at the intersection of the two perpendicular valleys.

Figure 18 shows the surfaces with three different surface treatments. The first sample (top right) has a line-like pattern with 100 J/cm<sup>2</sup> and 700  $F_{\text{acc}}$  and  $n_{\text{acc}}$ , respectively, without any cleaning treatment after the patterning of the surface. The second sample is the same as the first one, but cleaned in an ethanol bath (ET) for around 5 to 10 minutes. The last sample (below) is the same as the first one but cleaned in an ethanol bath and exposed to ultrasound (US) for around 5 to 10 minutes. The images show clearly



that the ethanol has no apparent interaction with the surface oxide and does not affect the topography or the morphology of the oxides. Nevertheless, there is a big effect of the ultrasound waves on the surface structure. It can be observed that most of the oxide particles were removed from the surface and the original titanium surface is exposed with just a few remaining particles. This gives important information about the stability of the surface and can be a important point to analyze in detail in the future works of this topic. In the next sections, the chemical characterization will also be used to complement the study of the effect of the ultrasound exposition of the samples.

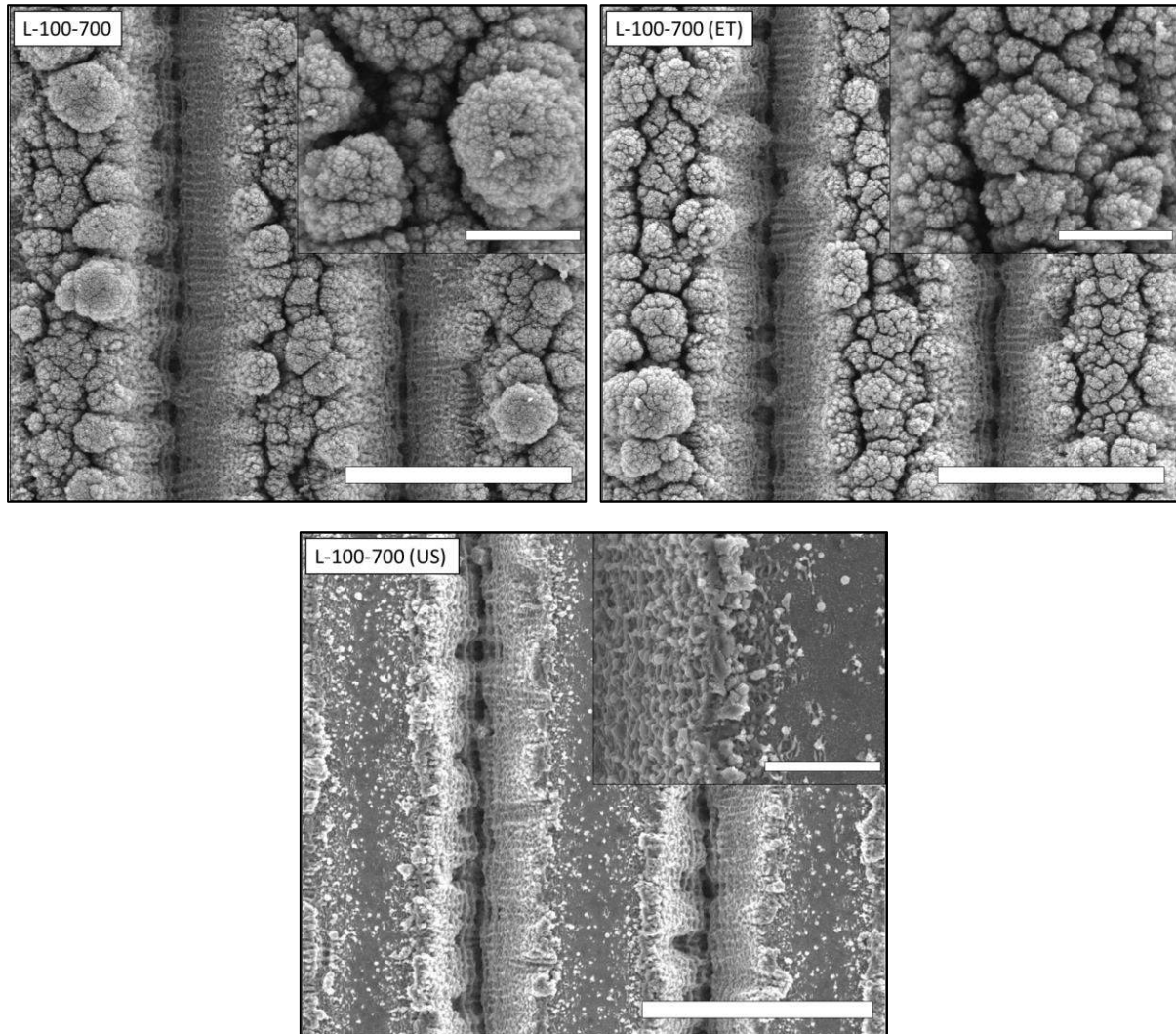


Figure 18 - SEM images for L-100-700 sample with three different conditions: uncleaned (left above); cleaned with ethanol (ET) without ultrasound (right above); and cleaned with ultrasound (US) in an ethanol bath (below). White bars represent a 10  $\mu\text{m}$  scale and a 2  $\mu\text{m}$  scale for the main picture and the inset, respectively.

#### 4.1.3. FIB transversal images

The surface properties of materials depend strongly on the specific area of the surface. This is why laser structuring is used to increase the surface area by targeted ablation of material (and in this case also to produce the oxidation of the titanium surface). The aim of this increase in the specific area is to enhance the efficiency of the surface, for the same volume of material. With a technique like DLIP, a periodic micrometer topography can be achieved and Figure 19 shows the result of the ablation process on line-like structures from 100  $\text{J}/\text{cm}^2$  (left above) to 1000  $\text{J}/\text{cm}^2$  (right below). Each cut was prepared in a way that at least three peaks could be observed. Distance measurements were added to the images to illustrate the pattern depth for different values of the accumulated fluence. It can be observed for the

four images that the peaks show a relatively large variation in height between the three peaks shown. In sample L-750-2475, for example, two peaks were measured from the bottom of the valleys to the top of the peak, and they show values of 16,61 and 19,92  $\mu\text{m}$ . As a result of this variation and the small sample size of three peaks per pattern, the depth of the patterns with an  $F_{\text{acc}}$  of 500, 750 and 1000  $\text{J}/\text{cm}^2$  cannot be distinguished. Instead, it is assumed that a situation is achieved and the depth does not increase further. For this work, the statistical study of the distribution of heights was carried out by CLSM and will be explained in the next section.

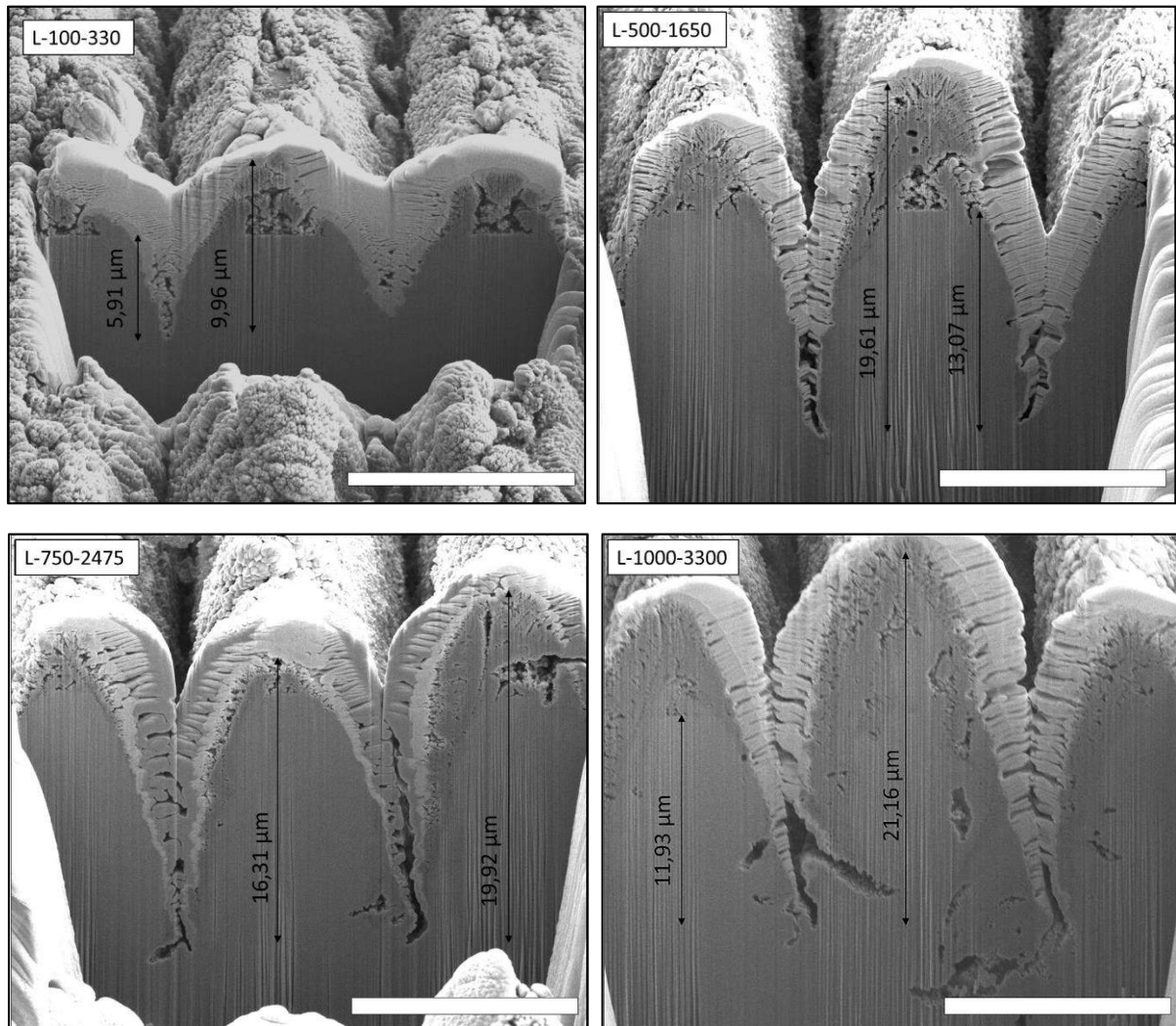


Figure 19 - SEM images of the transversal area of line-like pattern samples for 100, 500, 750 and 1000  $\text{J}/\text{cm}^2$ . White bars represent a 10  $\mu\text{m}$  scale.

Evidently, the variation of the accumulated fluence results in a change of the pattern depth, but also a different morphology of the valleys can be seen. Sample L-1000-3300 shows some damaged area under the surface, which can be associate to the combination of a high accumulated fluence and the high values of pressure and temperature accumulated below the surface. Picosecond lasers are considered USP lasers as they can ablate the surface material with less thermal increase and melting of the surface than other pulsed lasers. Nevertheless, they can show some temperature-dependent effects for high values of accumulated fluence (or pulse fluence) and these effects are reduced with the decrease of the pulse duration as discussed in Section 2.1.3. Many works have been published to compare the difference of pico- and femtosecond lasers for different materials [135–139].

Picosecond laser ablation is characterized by ejection of molten or evaporated material, which carry most of the ablated mass away from the ablation site, and then is solidified or condensed on the surface

[138]. The ejected material forms a porous structure of agglomerate particles that can be easily recognized and differentiated from the original not-oxidized titanium surface, as can be observed in Figure 19. This redeposited oxide particles generate a peak of material, increasing the distance between the deepest point at the valleys and the highest point of the surface. This increase in the pattern depth generates the increase of the specific area and in the next section, the surface roughness will be characterized quantitatively by surface roughness parameters.

#### 4.1.4. Roughness parameters

As explained in Section 3.3.1, the surface topography of a sample can be characterized by roughness parameters. The mean height ( $R_c$ ) represents the mean for the height of profile elements within the sampling length. This value gives the average height difference between valleys and peaks. The arithmetical mean height ( $S_a$ ) is a parameter that expands the profile parameter  $R_c$  (line roughness) two-dimensionally. Roughness ratio (S-ratio) is defined as the ratio between the actual and projected solid surface area. Therefore, it is 1 for a completely smooth surface and  $>1$  for a rough one.

Figure 20 and Figure 21 show the already presented surface roughness parameters  $R_c$  (mean height),  $S_a$  (arithmetical mean height) and S-ratio (roughness ratio), for line- and cross-like structures, respectively. For the case of line-like patterns, the mean height is taken in the direction perpendicular to the structure and the measurement is independent of the position of the measurement line. This way, the results consider the distance between the highest and deepest point of the surface. For the cross-like patterns, the surface has a periodical pattern in two directions, so the measurement for  $R_c$  was done with an angle of  $45^\circ$  with respect to the two line-directions, going through the points where the valleys intersect in both directions (deepest point of the surface).

For line-like patterns, it can be seen in Figure 20 that  $R_c$  and  $S_a$  have a similar tendency, where an increase of these values can be noted from samples with  $100 \text{ J/cm}^2$  to  $500 \text{ J/cm}^2$ . After this value of  $F_{acc}$ , it does not seem to be an important increase and these parameters achieve a saturation point, where an increase on  $F_{acc}$  does not involve a higher value of  $R_c$  and  $S_a$ . This behavior is not found in the value of S-ratio, where a constant and linear increase can be seen. Nevertheless, the mean height ( $R_c$ ) was compared with the measurements on the FIB images in Figure 19 (Section 4.1.3) and a big difference in these results can be noted. While the FIB-SEM images of the transversal area of samples L-500-1650, L-750-2475 and L-1000-3300 show a distance from the lowest to the highest point of the surface of between 16 and  $21 \mu\text{m}$ , the measurements achieved by CLSM are around  $6 \mu\text{m}$ . This means that the capability of the laser scanning microscope is not sufficient for these samples although the strongest magnification should achieve a sufficient resolution. However, the steep valleys cause a loss of signal as a result of light trapping so that the microscope cannot gain sufficient signal from the valleys and therefore cannot determine the pattern depth correctly.

For the three analyzed roughness parameters in Figure 20, it can be observed that the samples with fewer but stronger pulses (red curves) have higher values for the three parameters ( $R_c$ ,  $S_a$  and S-ratio) than samples with more but weaker pulses (black curves). This means that structures patterned with higher values of energy pulse exhibit higher values of surface roughness. Although the increase is not so strong, the number of pulses have a bigger influence on the surface topography modification than the value of the accumulated fluence (for  $F_{acc}$  between 500 and  $1000 \text{ J/cm}^2$ ). Nevertheless, this cannot be affirmed for  $F_{acc}$  between 100 and  $500 \text{ J/cm}^2$ , where the value of  $F_{acc}$  seems to be more significant than the value of  $n_{acc}$ . This can be contrasted with previous work [42], where titanium samples were patterned with 3 and  $10 \mu\text{m}$  periodicity but with lowest values of accumulated fluence (40 to  $150 \text{ J/cm}^2$ ). In the aforementioned work, the accumulated fluence was considered the most significant value when the topography of the surface was studied. It is important to remark that the range of parameters ( $F_{acc}$  and  $n_{acc}$ ) used was not the same.

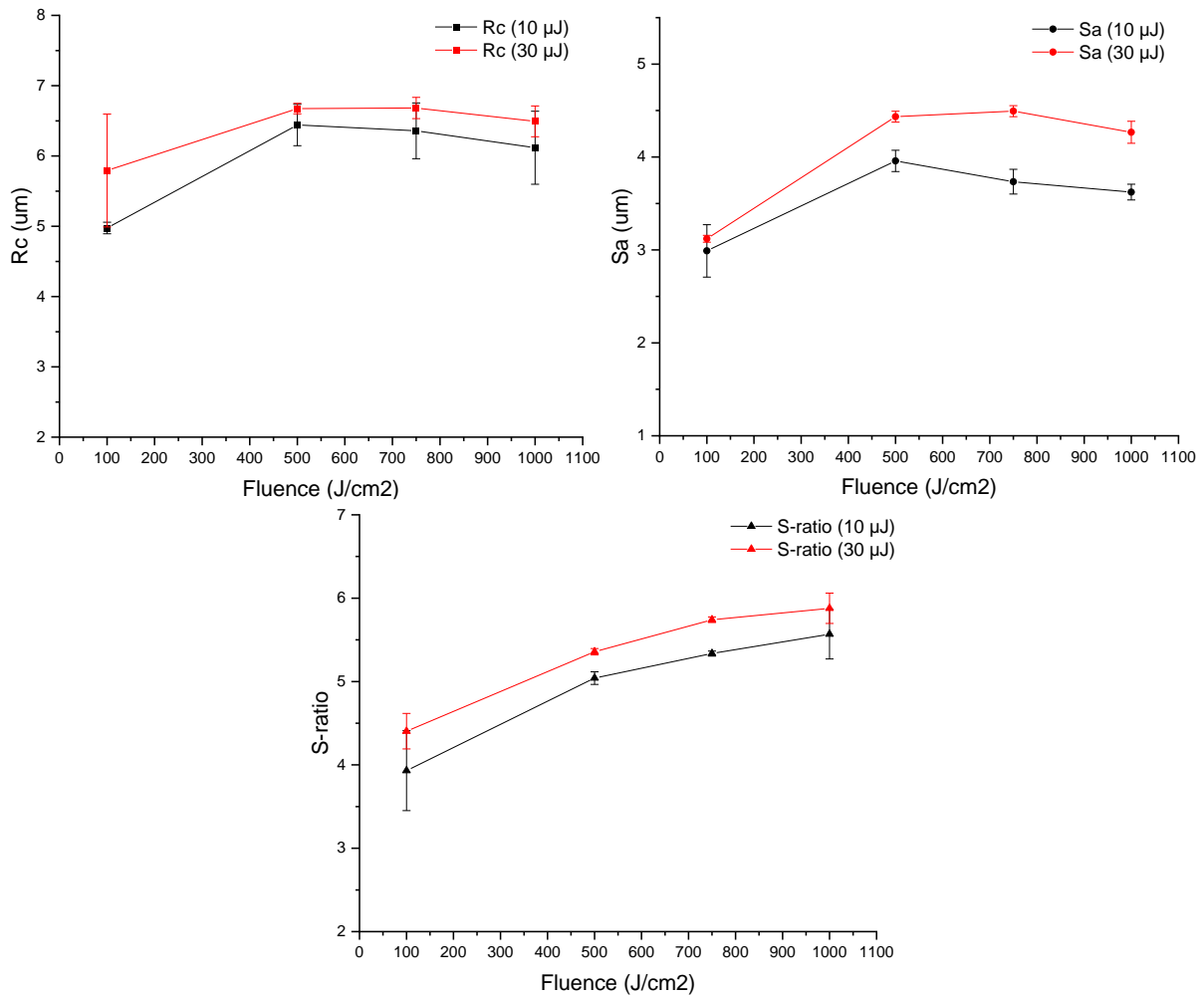


Figure 20 - Roughness parameters  $R_c$ ,  $S_a$  and S-ratio for line-like structures with a pulse energy of  $10 \mu\text{J}$  (black) and  $30 \mu\text{J}$  (red) measured by CLSM

The same tendency, observed for line-like patterns, can be seen in Figure 21 for cross-like patterns, Structures with less but stronger pulses (red curves) have, for same value of  $F_{acc}$ , higher values of  $R_c$ ,  $S_a$  and S-ratio than structures with more but weaker pulses (black curves). For cross-like samples, this influence of the  $n_{acc}$  is clearer than for line-like samples. In the case of  $S_a$  and S-ratio, this influence of the  $n_{acc}$  corresponds to samples with at least  $500 \text{ J/cm}^2$ , as no difference in these values is observed for the samples with  $100 \text{ J/cm}^2$ . Besides, this difference between samples with less and more pulses (red and black curves, respectively) increases with the value of  $F_{acc}$ . Finally, as it was the case for line-like patterns, S-ratio seem to be the only parameter that shows an increase for higher values of  $F_{acc}$ , while this cannot be clarified for  $R_c$  and  $S_a$ .

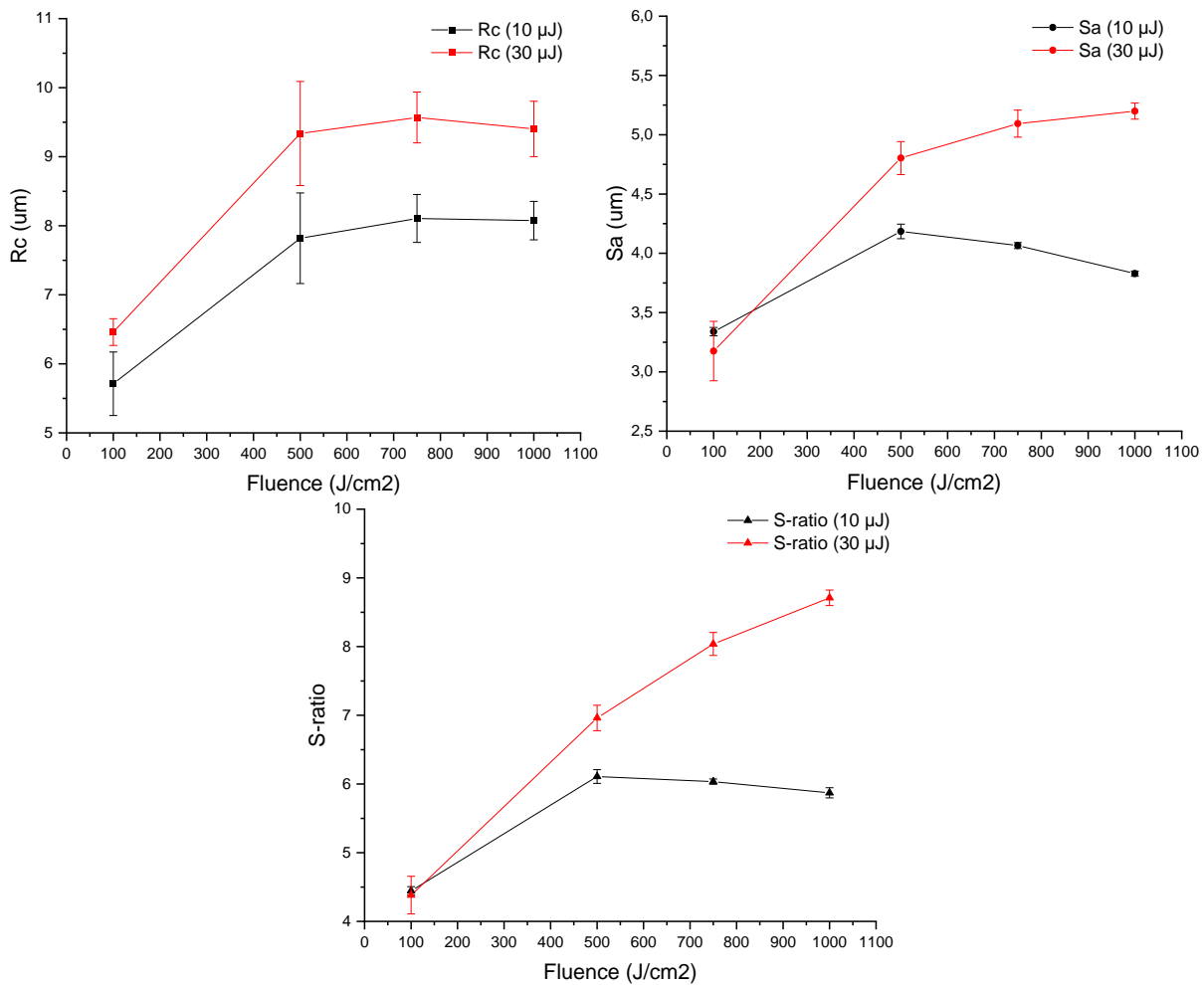


Figure 21 - Roughness parameters  $R_c$ ,  $S_a$  and  $S$ -ratio for cross-like structures with a pulse energy of  $10 \mu\text{J}$  (black) and  $30 \mu\text{J}$  (red) measured by CLSM

## 4.2. Methylene blue degradation

The absorbance values measured by the UV/Vis spectra were correlated to the concentration of MB on the solution, so the change in the concentration of the solution after two hours of UV exposure can be used as a quantitative value to characterize the efficiency of this technique. With the help of the calibration curve explained in Section 3.3.2, constructed by measuring absorbance values at known concentrations, the final concentration ( $C$ ) of the solutions was compared with the reference concentration ( $C_0$ ) of the solutions for pure titanium samples which were also exposed to UV light in the same conditions, but without any laser oxidation. This way, the absence of photocatalytic activity of pure titanium could be checked. The ratio of these two values was calculated and shown as  $C/C_0$ . Figure 22 and Figure 23 show the measured values of  $C/C_0$  ratios for line-like samples and cross-like samples, respectively. Purple bars represent lower energy pulses and orange bars represent higher energy pulses.

For the UV/Vis measurements, plastic cuvettes were used to contain the solutions while the absorbance was measured, as it was explained in Section 3.3.2. The results of the first measurements presented a significant variation between the three samples with same parameters. After analyzing the reasons, it was detected that different cuvettes showed different results for the same solution, although the device measures the absorbance spectrum using a cuvette with water as a reference (same cuvette for all measurements). As a solution, each cuvette absorbance spectrum was measured without solution and used as reference for the resulting spectrum with the solution. Additionally, some measurements were

repeated to make sure the values were correctly measured and, in some cases, some solutions corresponding to same parameters were measured in the same cuvette to eliminate error sources. Despite these considerations, the results did not present high repeatability, as can be seen from some of the error bars in the charts.

The change in the solutions concentration for line-like samples is shown in Figure 22. The results exhibit a very low value of final concentration for samples between 500 and 1000 J/cm<sup>2</sup> of  $F_{acc}$ , specially for sample L-500-1650 where the reduction in the MB concentration was higher than 60%. This could mean that accumulated fluences of 750 or 1000 J/cm<sup>2</sup> are not necessary to achieve highly efficient patterned surfaces. These values show an improvement in comparison to previous work [42], where values of  $C/C_0$  between 0,5 and 0,65 were observed for 10  $\mu\text{m}$  periodicity patterns and  $F_{acc}$  between 70 and 725 J/cm<sup>2</sup>, also using picosecond laser with DLIP. 3  $\mu\text{m}$  periodicity samples were also produced in [42] and the change in the concentration was seen to be between 50% and 85%. The characterization of the photocatalytic activity of samples patterned with less energy pulses (L-100-700, L-500-3500, L-750-5250 and L-1000-3300) will be part of future work to determine the influence of the number of pulses per point for line-like structures.

The photocatalytic activity of this samples can be correlated with the roughness parameters shown in previous section. Higher values of roughness parameters involve higher specific surface area and then, higher real area of interaction between surface and solution. Figure 20 shows the  $S_a$  and S-ratio values of samples L-100-330, L-500-1650, L-750-2475 and L-1000-3300 (red curve). These parameters are directly related with the specific area of the sample as it was explained in Section 3.3.1. These results show an increase of the roughness of the surface when  $F_{acc}$  is increased from 100 to 500 J/cm<sup>2</sup> ( $S_a$  increased from 3  $\mu\text{m}$  to 4,5  $\mu\text{m}$  and S-ratio from 4,4 to 5,4). This increase in the specific surface area is in concordance to the increase of the photocatalytic activity showed in Figure 22. It will be explained later that the crystalline nature of the samples has also a big influence on these results. When the  $F_{acc}$  value was between 500 and 1000 J/cm<sup>2</sup>, there was not a significant change in the roughness surface and this is also in concordance with the MB results, as samples L-500-1650, L-750-2475 and L-1000-3300 exhibit a similar value of  $C/C_0$ .

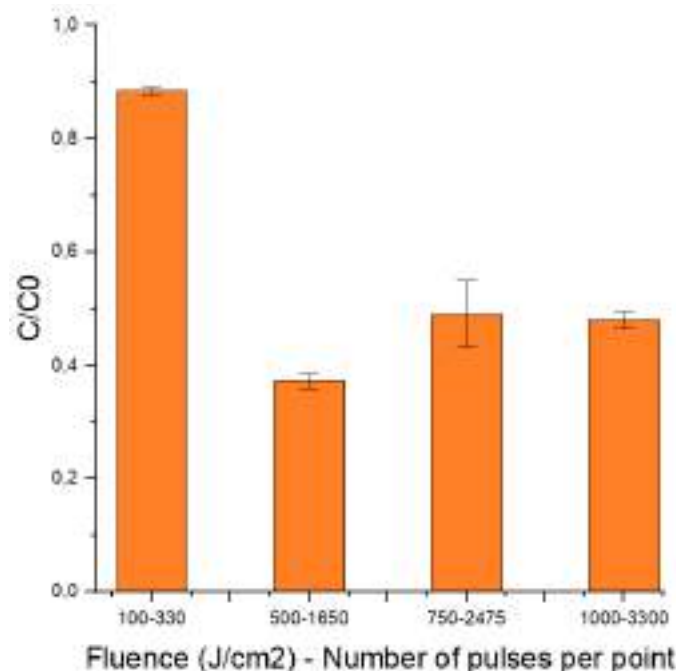


Figure 22 –  $C/C_0$  ratio for line-like samples (higher energy pulses).

Cross-like patterned samples, with both high and low number of pulses per point, were analyzed and the results are shown in Figure 23, where the change in the concentration of the MB solution was measured for samples between 100 and 1000 J/cm<sup>2</sup> of  $F_{acc}$ . The particularity of these samples is not

only their topographical morphology (cross pattern) but the fact that they were structured in two steps, so the second step was done over an already patterned surface. This is interesting to take into account because the results of these samples, for the same laser parameters, are slightly different from the ones shown in Figure 22, but with the same tendency. It can be seen that the  $C/C_0$  ratio decreased for higher values of  $F_{acc}$ , while for the case of line-like samples it was not seen after 500 J/cm<sup>2</sup> of  $F_{acc}$ . Samples L-750-2475 and L-1000-3300 show an equal (or even higher) value of the  $C/C_0$  ratio to sample L-500-1650 (Figure 22), while samples C-750-2475 and C-1000-3300 show a lower value of the  $C/C_0$  ratio to sample C-500-1650. In addition, sample C-1000-3300 shows even higher photocatalytic activity than sample L-1000-3300 (same parameters but different pattern). In fact, sample C-1000-3300 shows the best performance of this set of experiments, with a change in the MB concentration higher than 70%.

The combination of parameters for samples L-100-330 and C-100-330 ( $F_{acc} = 100$  J/cm<sup>2</sup> and  $n_{acc} = 330$ ) shows the worst performance, with a degradation value of 5% for both cases. Nevertheless, much better results can be observed for sample L-100-700, which is a sample with the same value of  $F_{acc}$ , but a higher number of pulses (and consequently pulses with less energy) than the already mentioned samples. Just taking into account cross-like patterned samples in Figure 23, the results do not express a clear tendency while comparing samples with lower or higher values of  $n_{acc}$ . For instance, samples C-100-700 and C-500-3500 show more degradation capability than samples C-100-330 and C-500-1650, respectively. That can give an idea of a higher photocatalytic activity of samples prepared with a bigger number of pulses, for the same value of accumulated fluence. But this is not the case when samples C-750-5250 and C-1000-7000 are compared with samples C-750-2475 and C-1000-3300. Here, the tendency is inverse, and samples with a lower value of  $n_{acc}$  show better results (i.e., comparison of samples C-1000-7000 and C-1000-3300).

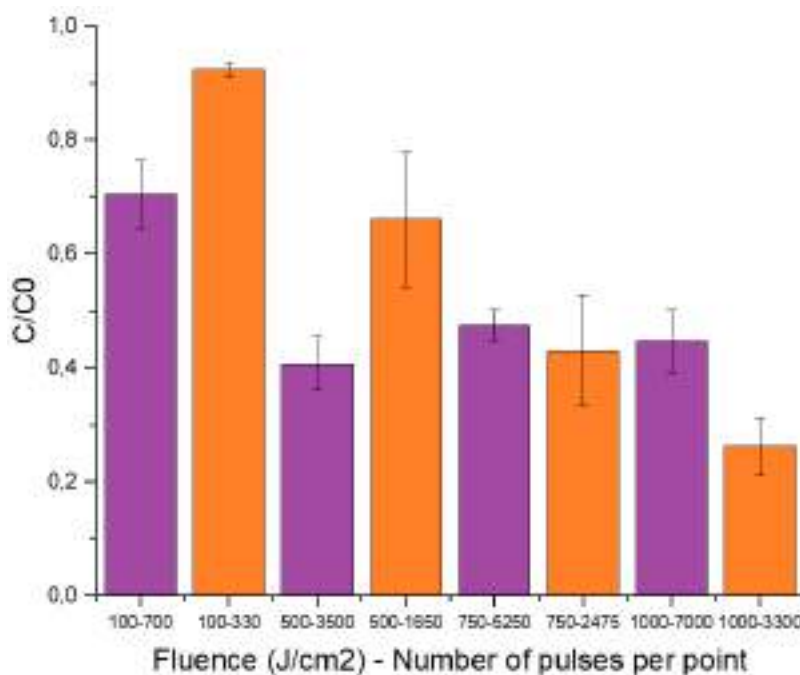


Figure 23 –  $C/C_0$  ratio for cross-like samples (lower energy pulses in purple and higher energy pulses in orange).

These differences can be explained when comparing the results of the MB degradation with the roughness parameters measured with CLSM. As it was the case for line-like samples, there is correlation between the increased specific surface area and the activity of the samples. Samples with weaker pulses (purple bars in Figure 23) showed an increase in the photocatalytic activity when  $F_{acc}$  was increased from 100 to 500 J/cm<sup>2</sup>, but no significant increase was measured when  $F_{acc}$  was between 500 and 1000 J/cm<sup>2</sup>. When comparing with the roughness parameters  $S_a$  and S-ratio (black lines in Figure 21), the surface roughness was also increased when  $F_{acc}$  was increased from 100 to 500 J/cm<sup>2</sup> and no increase was seen above 500 J/cm<sup>2</sup>. Same tendency was observed for samples with stronger pulses and the comparison between CLSM measurements (red lines in Figure 21) and degradation results



(orange bars in Figure 23) shows that the increase of the roughness parameters involved enhanced photocatalytic properties. The correlation between topography and activity indicates that the photocatalytic activity increase when the specific surface area is larger, as it was the case for line-like samples.

The comparison between the same sample before and after exposure to ultrasound under an ethanol bath was carried out and the results of the MB degradation capability are plotted in Figure 24. Sample L-500-1650 (line-like pattern) was characterized in these two different conditions and the photocatalytic activity of the surface showed a big change, going from around 0,4 to 0,75 of the  $C/C_0$  ratio. This lower value of degradation capability is related to the oxides removed from the surface during the treatment. This is an important fact because the stability of the surface should be taken into account when thinking about the repeatability of the results in the future. The additional chemical characterization will be shown in the next section.

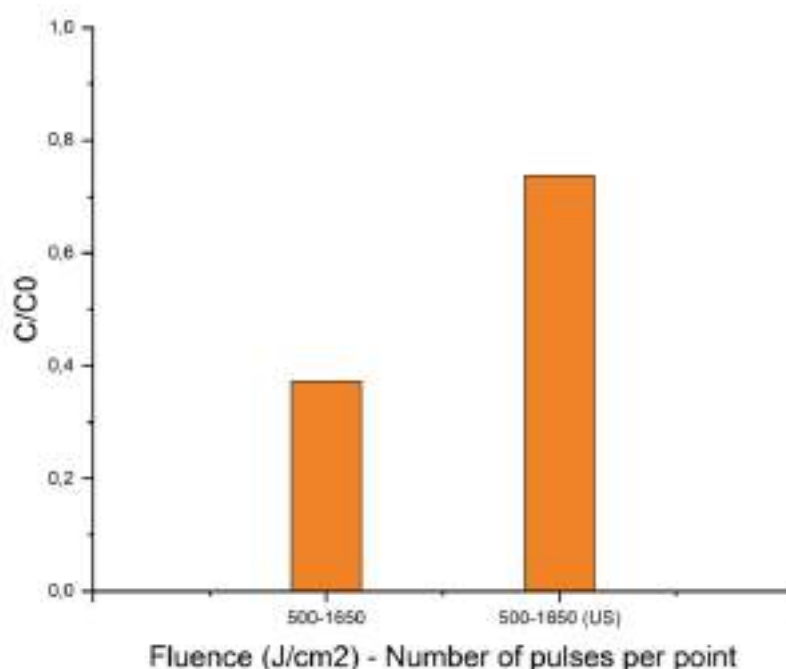


Figure 24 -  $C/C_0$  ratio for sample L-500-1650 before and after ultrasound (US) treatment.

### 4.3. Grazing incidence X-ray diffraction (GI-XRD)

XRD analysis is a versatile technique for crystallographic characterization of samples with long-range order and for this work, the present phases of titanium and its oxides were analyzed by grazing incidence X-ray diffraction. The aim of this study is to correlate the laser parameters with the found phases on the sample surface. Line- and cross-like patterns were measured and the resulting graphs are plotted in Figure 25 (line patterns with a small number of pulses per point) and Figure 26 (cross pattern with a big and small number of pulses per point). Additionally, the comparison of the chemical composition between samples before and after the cleaning process with ultrasound is shown in Figure 27 to understand the effects of this treatment. All measurements were produced in the same angle range of  $2\theta$  ( $20^\circ - 70^\circ$ ), with a  $0.05^\circ/\text{step}$  and  $50 \text{ s}/\text{step}$  setup. Samples were oriented with the valleys parallel to the X-ray incidence, so both valleys and peaks could be measured and the shadowing effect of the peaks could be avoided. On each produced graph, vertical lines at specific  $2\theta$  angle values were placed, to denote the most important peaks of the phases found in the plots and to facilitate a clear analysis and comparison.

To have a better understanding of the formation of the different oxides and their relation with the laser parameters, the present phases are summarized in Table 5, where the relative amount of each phase



is represented by a scale from X to XXX to differentiate between samples with a low-, medium- and high-quantity of a specific phase, or “-” for no presence of the correspondent phase. The following phases (with their respective crystal structure and XRD chart source) were found:

- $\alpha$ -Titanium: hexagonal (ICDD: 00-071-0859)
- R-Rutile ( $\text{TiO}_2$ ): tetragonal (ICDD: 01-072-7374)
- A-Anatase ( $\text{TiO}_2$ ): tetragonal (ICDD: 01-075-2545)
- H-Hongquite (TiO): cubic (ICDD: 01-073-8760)
- T-Tistarite ( $\text{Ti}_2\text{O}_3$ ): rhombohedral (ICDD: 04-005-4652)

Line-like patterns were measured using one single  $5 \times 5 \text{ mm}^2$  sample for each scan and results for samples with a pulse energy of  $30 \mu\text{J}$  (samples L-100-700, L-500-1650, L-750-2475 and L-1000-3300) are shown in Figure 25 and summarized in Table 5. One of the most interesting things about this result is the evolution of the anatase and rutile phases with the variation of the accumulated fluence from  $100 \text{ J/cm}^2$  (below) to  $500 \text{ J/cm}^2$  (above). These polymorphs of  $\text{TiO}_2$  are, as it was described in Section 2.2.1, the phases with the highest photocatalytic activity, and the coexistence of both of them can have synergistic effects, depending on their morphology. In this case, there is no presence of this rutile or anatase for sample L-100-330, but for samples above  $500 \text{ J/cm}^2$ , the characteristic peaks can be found at around  $27^\circ$  and  $25^\circ$ , respectively. The rutile peaks at  $\sim 41^\circ$  and  $54^\circ$  also show how the increase of the accumulated fluence generates a major presence of rutile on the oxidized surface. Nevertheless, when the value of  $F_{\text{acc}}$  was increased above  $500 \text{ J/cm}^2$ , no changes on the anatase and rutile peaks were seen. When  $F_{\text{acc}}$  is higher than  $500 \text{ J/cm}^2$ , the generation of anatase and rutile was independent of the  $F_{\text{acc}}$  value. These results are in agreement with the ones observed in Figure 22, where the MB degradation (i.e., the photocatalytic activity) was strongly increased when  $F_{\text{acc}}$  went from 100 to  $500 \text{ J/cm}^2$  and no relevant difference was observed for the degradation capability of samples L-500-1650, L-750-2475 and L-1000-3300. The confirmed presence of rutile and anatase explains the observed degradation capacity of the oxidized surface, as was expected based on previous works [42,107–109,112].

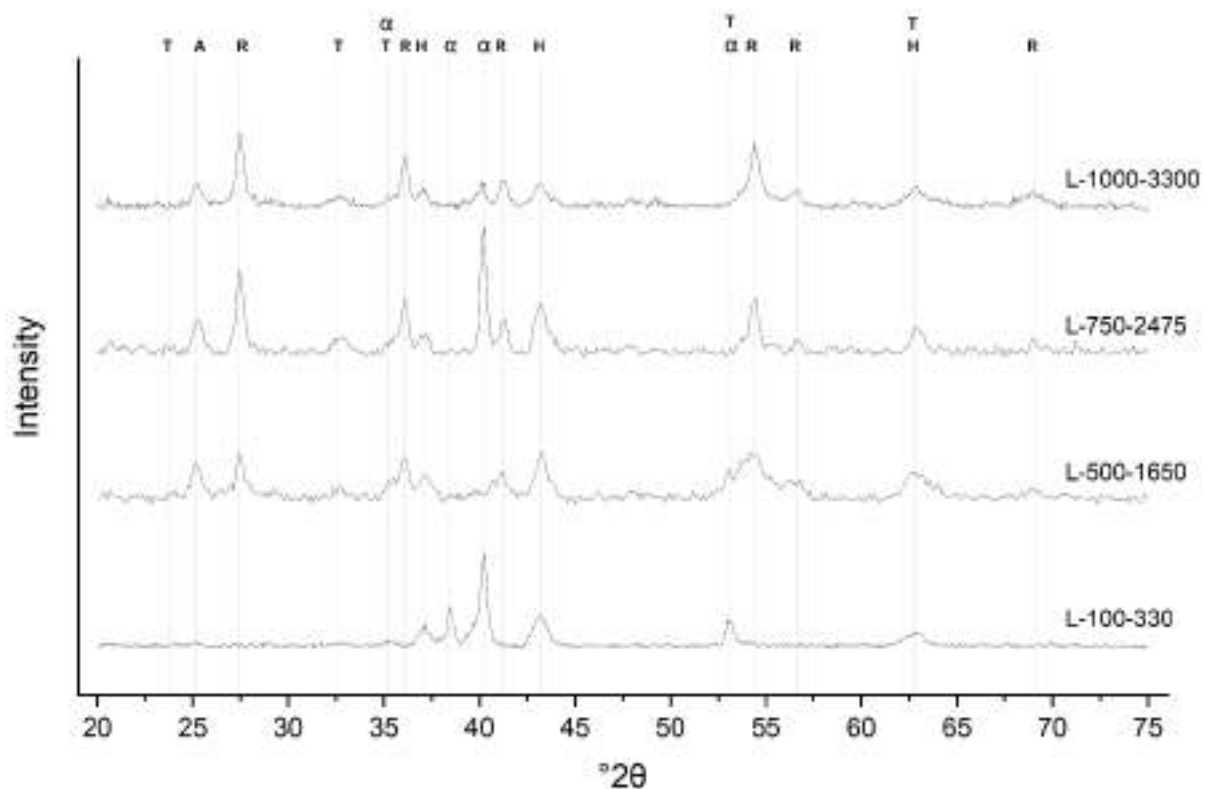


Figure 25 - XRD for line-like structures patterned with energy pulse of  $30 \mu\text{J}$  (low number of pulses per point).

Another important factor is the presence of TiO and Ti<sub>2</sub>O<sub>3</sub> (or in their mineral names hongquite and tistarite, respectively). TiO characteristic peaks are approximately located at 37°, 43° and 63° and the most important Ti<sub>2</sub>O<sub>3</sub> peaks can be found at around 24°, 33°, 35°, and 53° (this last two are also shared with  $\alpha$ -titanium). The dependence of these phases on the different values of accumulated fluence was summarized in Table 5 and can be observed in the different curves of Figure 25. TiO is present for all samples but the sample L-1000-3300 (highest fluence value) has a lower height on the characteristic peaks. Ti<sub>2</sub>O<sub>3</sub> peaks are difficult to analyze because of their superposition with the  $\alpha$ -Ti peaks (35° and 53°). Nevertheless, the small peak at ~32,5° can give the idea that the presence of Ti<sub>2</sub>O<sub>3</sub> can be seen for above 500 J/cm<sup>2</sup>, as the peak is not observed for sample L-100-330. Both, TiO and Ti<sub>2</sub>O<sub>3</sub> were observed in previous work for laser structured titanium [132]. Although the presence of Ti<sub>2</sub>O<sub>3</sub> and TiO<sub>2</sub> was found to be an interesting combination to enhance photocatalytic properties in previous work [115], the presence of tistarite cannot be directly related to the MB degradation results, and a more detailed study should be carried out for a better understanding of the synergistic effects.

Cross-like patterns were measured using an arrangement of four 5x5 mm<sup>2</sup> samples, which give a total of 20x20 mm<sup>2</sup> measure area, and a stronger signal could be reached. To do so, the samples were mounted on plasticine and leveled with a flat tool and slight pressure. Samples with different n<sub>acc</sub> for the same F<sub>acc</sub> were measured and the results can be compared. The XRD graphs for samples C-100-700, C-500-3500, C-750-5250 and C-1000-7000 and C-100-330, C-500-1650, C-750-2475 and C-1000-3300, are shown in Figure 26 (and the present phases are summarized in Table 5 for all samples).

Because the cross-like samples were analyzed over a plasticine structure, the resulting peaks of plasticine should not be considered on the analysis. To do so, the plasticine used for the measurements was analyzed individually to find out which peaks correspond to its structure. The resulting chart can be found in the Appendix 2, where the high peaks at around 29°, 47° and 48° can be found (plasticine peaks are denoted in Figure 26 with a gray "P", so they can be avoided while analyzing the chart).

Cross-like samples in Figure 26 show the same tendency as line-like samples when the F<sub>acc</sub> increase from 100 to 500 J/cm<sup>2</sup>. The presence of rutile and anatase (mainly denoted for their main peaks at 27.5° and 25°, respectively) is not observed in samples with F<sub>acc</sub> of 100 J/cm<sup>2</sup> (C-100-700 and C-100-330) but it can be seen in samples with 500, 750 and 1000 J/cm<sup>2</sup> of F<sub>acc</sub>. Two other peaks of rutile (at 41.5° and 54°) confirm that this phase can be found in samples with an F<sub>acc</sub> higher than 500 J/cm<sup>2</sup>. The absence of rutile and anatase for samples with F<sub>acc</sub> of 100 J/cm<sup>2</sup> can be correlated with the lower values of activity measured in MB experiment and shown in Figure 23.

For samples with a higher n<sub>acc</sub> but lower pulse energy (C-100-700, C-500-3500, C-750-5250 and C-1000-7000), the amount of rutile was high but invariant for F<sub>acc</sub> between 500 and 1000 J/cm<sup>2</sup>. On the other hand, the amount of anatase decreased in this samples when F<sub>acc</sub> was increased from 500 to 1000 J/cm<sup>2</sup>. These two tendencies are shown in Table 5. When comparing these results with the results measured for the photocatalytic activity in Figure 23, it can be seen that samples C-500-3500, C-750-5250 and C-1000-7000 are approximately equally active (C/C<sub>0</sub> value is between 0,4 and 0,47). As the amount of rutile is the same for this samples, it can be thought that this phase has a bigger influence on the activity of the samples than anatase, as no relevant difference on the activity was seen when the anatase phase was decreased for higher values of F<sub>acc</sub>. A more precise technique to characterize the photocatalytic activity can give more information about the difference between the samples and the influence of the anatase phase.

For samples generated with lower n<sub>acc</sub> and higher pulse energy (C-100-330, C-500-1650, C-750-2475 and C-1000-3300), the amount of both anatase and rutile increased when F<sub>acc</sub> was raised from 500 to 1000 J/cm<sup>2</sup>, as it can be seen in Table 5. The result of the increase of these phases is the improvement of the degradation capability of this samples, shown in Figure 23. Sample C-500-1650 exhibits a degradation capability of around 44%, while for sample C-750-2475 this value was 67% and for sample C-1000-3300 was 74%.

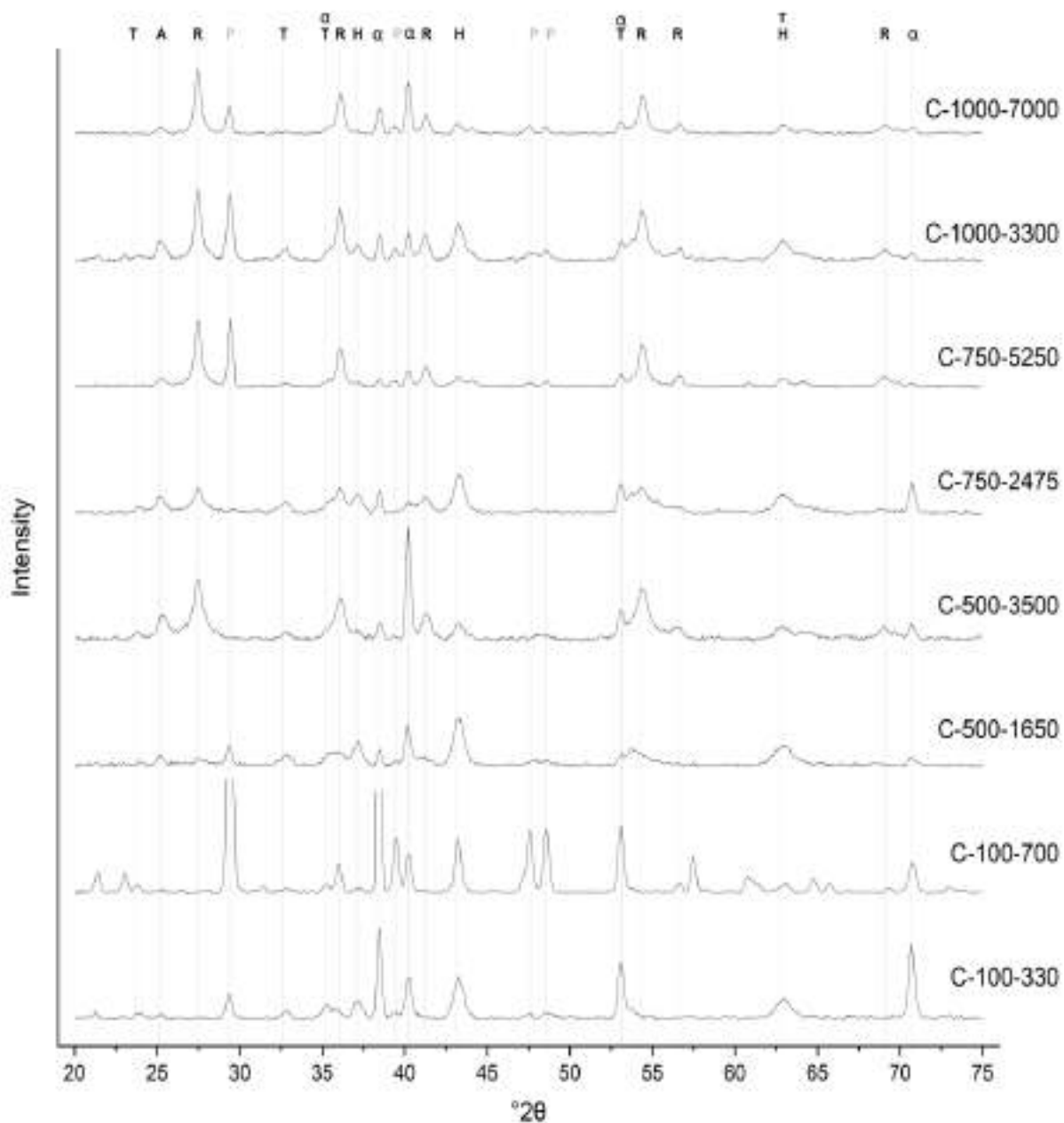


Figure 26 - XRD for cross-like structures patterned with energy pulse of 10 and 30  $\mu\text{J}$  (high and low number of pulses per point, respectively).

When comparing cross-like samples with line-like samples, the dependence of the presence of rutile and anatase with the  $F_{\text{acc}}$  is different. For line-like samples structured with a pulse energy 30  $\mu\text{J}$ , no significant difference in the amounts of these phases was found when  $F_{\text{acc}}$  was between 500 and 1000  $\text{J}/\text{cm}^2$ , while an increment of both phases was seen when  $F_{\text{acc}}$  was increased from 500 to 1000  $\text{J}/\text{cm}^2$ . This differences in the composition between the two different structures (line and cross) are also correlated with the differences seen between Figure 22 and Figure 23 on the activity of the samples. For example, sample L-500-1650 shows a degradation capability of around 63%, while for sample C-500-1650 this value is just of 44%. The sample with line-like pattern shows in Table 5 a higher quantity of anatase and rutile than the sample with cross-like pattern, even though the laser parameters are the

same. Here, the role of the kind of structure shows again a difference in the resulting composition of the samples and, thereby, on the photocatalytic activity of them.

TiO and Ti<sub>2</sub>O<sub>3</sub> were also found in cross-like samples, as it was the case for line-like samples. Table 5 shows how the increase in the value of F<sub>acc</sub> involves a smaller amount of these two phases, both for samples with big and small n<sub>acc</sub>, even showing no presence of Ti<sub>2</sub>O<sub>3</sub> in sample C-1000-7000. It is important to denote the difference between samples with big n<sub>acc</sub>, where just a small amount of TiO was found, with samples with small n<sub>acc</sub>, where a bigger proportion of this phase is observed. This is a clear example of how n<sub>acc</sub> influences the oxide formation on titanium samples when patterned with picosecond laser. Finally, an interesting result is the absence of the tistarite phase for sample L-100-330, while this phase is highly present in sample C-100-330 (same laser parameters but different structure). Due to the difference in the type of structure and the orientation of the X-ray beams for the GI-XRD technique (incidence angle of 0.8°), the comparison between like-line and cross-like samples is harder to understand and complementary crystallographic measurement techniques should be use in the future.

Another important analysis was carried out to understand the oxide formation on patterned titanium samples. The influence of a surface cleaning treatment, in this case ultrasound in ethanol bath, was studied and the chemical composition of the surface was correlated with the MB degradation results for sample L-500-1650. It was seen in SEM characterization that the porous oxide particles agglomerated on the peaks are removed after US exposure (see Figure 18). Additionally, the MB degradation test exposed the lost in the photocatalytic activity of the titanium surface after the treatment. The composition of the remanent oxide layer after the US exposure for sample L-500-1650 can be seen in Figure 27 and compared with the original surface.

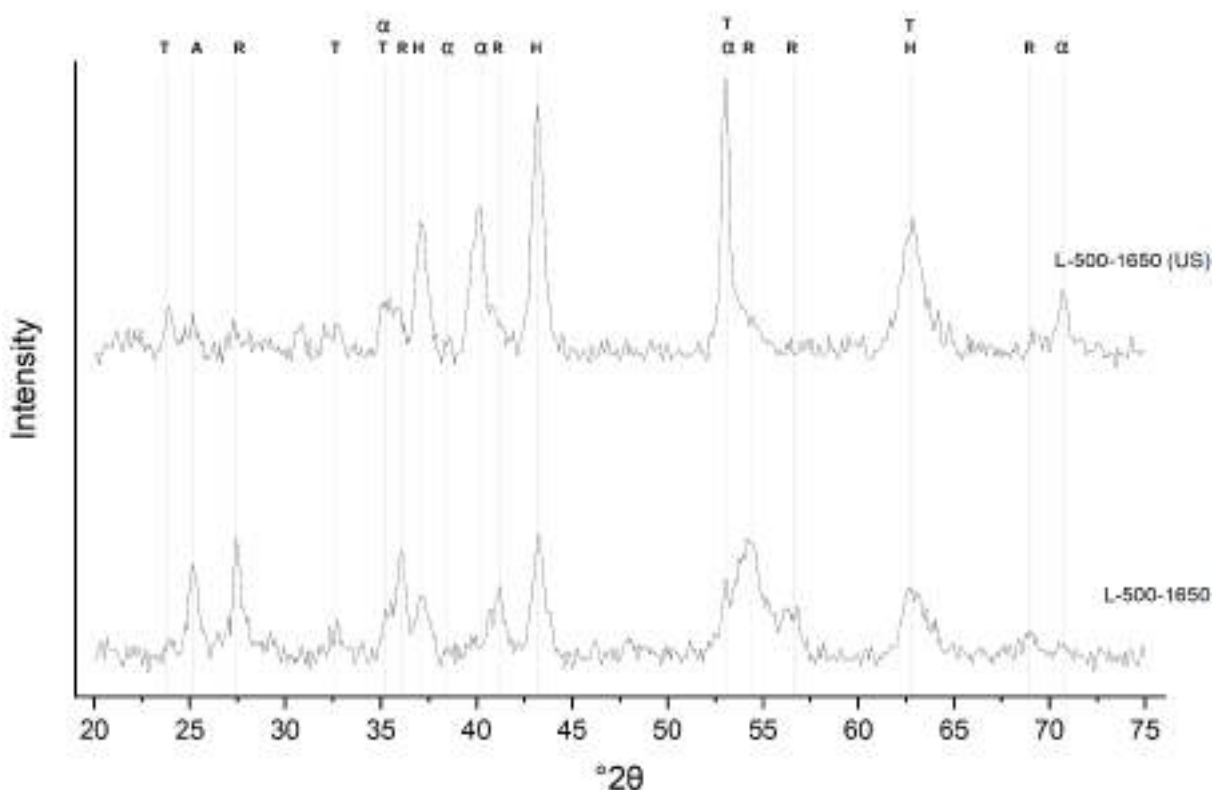


Figure 27 - XRD for L-500-1650 samples after ultrasound (US) cleaning in ethanol (above) and without cleaning (below).

Figure 27 shows a higher signal of  $\alpha$ -titanium phase for sample L-500-1650 (US), as it can be mainly seen on the peaks at 40° and 53°. Also, a greater amount of titanium monoxide (hongquite) is observed in this sample, as the peaks at 37° and 43° are higher than the ones for the sample before US exposure. Same case happens for the tistarite phase (Ti<sub>2</sub>O<sub>3</sub>) as it can be seen in peaks at 24°, 33.5° and 53° (this

last one is shared with the  $\alpha$ -titanium phase, so there is some overlap of both phases at this position). This is not the case for rutile (27.5°, 41° and 57°) and anatase (25°) peaks, which were removed from the sample surface because of this cleaning treatment and explain the results of the MB degradation test. Table 5 sums up all these results and the elimination of the active phases (rutile and anatase) is shown, involving a loss in the photocatalytic activity, as shown in Figure 24.

Because of these results, some interesting conclusions about the effect of ultrasound can be made. The remanent presence of the tistarite and hongquite phases after the application of ultrasound is proof that these phases are closer to the surface, while the rutile and anatase phases are present in the outermost layers and are more easily removed. TiO and Ti<sub>2</sub>O<sub>3</sub> are phases poor in oxygen, compared to the phases of titanium dioxide, rutile and anatase, which have a higher proportion of oxygen. This is important because some three-dimension understanding of the oxide layer is possible and can be a starting point for a future and more detailed study of this topic. To sum up, ultrasound cleaning of the patterned titanium samples under an ethanol bath generates the removal of the superficial oxides (mainly rutile and anatase), which seem to have low stability, resulting in a lower degradation efficiency of the MB solution.

General conclusions of XRD results can be summarized after this analysis. First of all, all samples show a relevant amount of rutile and anatase (photocatalytic active phases) when F<sub>acc</sub> was higher than 500 J/cm<sup>2</sup>. Samples with F<sub>acc</sub> of 100 J/cm<sup>2</sup> did not show presence of these phases and, consequently, lower values of photocatalytic activity were measured. The presence of these phases between 500 and 1000 J/cm<sup>2</sup> depended on the kind of structure and the number of pulses per point. Samples with higher quantity of rutile and anatase, like C-500-3500 and C-1000-3300, showed the best values of degradation efficiency (60% and 65%, respectively). The presence of TiO and Ti<sub>2</sub>O<sub>3</sub> was also confirmed with XRD and samples structured with less but stronger pulses showed a greater presence of these two phases, especially for TiO. Additionally, TiO was mostly generated in low fluence samples, like C-100-330 or L-100-330. Finally, the photocatalytic efficiency of the different oxides was confirmed by studying the differences of a sample before and after ultrasound bath, where the cleaning treatment removed the superficial and more active oxides, leaving only some TiO and Ti<sub>2</sub>O<sub>3</sub> and decreasing the degradation capability around 50% (Figure 24).

Sample	( $\alpha$ ) $\alpha$ -Titanium	(R) Rutile TiO <sub>2</sub>	(A) Anatase TiO <sub>2</sub>	(H) Hongquite TiO	(T) Tistarite Ti <sub>2</sub> O <sub>3</sub>
L-100-330	XX	-	-	XX	-
L-500-1650	X	XX	XX	XX	X
L-750-2475	XXX	XXX	XX	XX	X
L-1000-3300	XX	XXX	XX	X	X
C-100-700	XXX	-	-	XX	X
C-500-3500	XXX	XXX	XXX	X	X
C-750-5250	XX	XXX	XX	X	X
C-1000-7000	XX	XXX	X	X	-
C-100-330	XXX	-	-	XXX	XXX
C-500-1650	XXX	X	X	XXX	X
C-750-2475	XX	XX	XX	XXX	X
C-1000-3300	XX	XXX	XXX	XX	X
L-500-1650	X	XX	XX	XX	X
L-500-1650 (US)	XX	X	X	XXX	XXX

Table 5 - Present phases in characterized samples by XRD (- for "no presence", X for "low quantity", XX for "medium quantity" and XXX for "high quantity")

## 5. Conclusions

Surface modification by laser oxidation of pure titanium samples was successfully achieved by picosecond laser DLIP. This technique produced periodic patterns of 10  $\mu\text{m}$  periodicity and a complex titanium oxide layer on the surface. This oxide layer was produced by the laser interaction of the beams with the titanium surface, with pulses in the order of picoseconds (ultrashort pulses). The formation of valleys is explained as the result of laser ablation, where different thermal phenomena occur on the surface (melting and evaporation of matter). On the other side, peaks are generated due to the redeposition of ablated material and a porous and agglomerated structure of oxide particles is formed between valleys. The influence of two laser parameters (accumulated fluence and number of pulses per point) on the final surface properties was studied in this work, and the correlation between topological, chemical and photocatalytic properties was carried out. Two different morphologies (line- and cross-like pattern) were produced for the same values of  $F_{\text{acc}}$  and  $n_{\text{acc}}$ . All samples were produced using the interference of two coherent beams, which allows for a line-like pattern with a periodic distance between intensity peaks or maxima.

The structures were observed in SEM microscopy images, and a focused ion beam was used to image the transversal area by cutting into the material. Samples with higher value of  $n_{\text{acc}}$  show a more homogeneous distribution of particles, while samples with lower value of  $n_{\text{acc}}$  denote more disorganized arrangement of particles. Also, samples with higher values of  $F_{\text{acc}}$  show a higher concentration of redeposited particles and less distance between them, in comparison with samples with lower  $F_{\text{acc}}$ . This clearly denotes a big dependence on the morphology of the sample with the laser parameters. In addition, the use of the picosecond pulses with DLIP allowed the generation of LIPSS, which involve submicron semi-periodic lines on the peaks of the samples.

The effect of different cleaning treatments was studied and some results can be taken from the experiments. Samples cleaned with ethanol and without any external stimulation did not show any difference in the topography, as it was confirmed by SEM images. On the contrary, samples cleaned with ethanol in ultrasound showed a high removal of the oxides particles, confirmed by SEM images and XRD results. The photocatalytic activity of this modified samples was markedly decreased, as the specific surface area was reduced and the phases with high photocatalytic activity were mostly removed.

The FIB images of the transversal area of the samples allowed a better understanding of the modification of the surface, as the peaks and valleys cuts could be observed for line-like samples. The distance between valleys and peaks was found between 10 and 20  $\mu\text{m}$ . The arrangement of the redeposited particles was observed and the many defects and a high porosity were found.

The surface roughness parameters showed mostly an increase of the  $R_c$ ,  $S_a$  and S-ratio of the samples when the value of  $F_{\text{acc}}$  was increased. For line- and cross-like samples,  $F_{\text{acc}}$  was seen as the most influential parameter for lower values of  $F_{\text{acc}}$ . On the contrary, for higher values of  $F_{\text{acc}}$ , the roughness parameters do not increase when  $F_{\text{acc}}$  is increased and  $n_{\text{acc}}$  is the most important parameter. In some cases, no increase of the surface roughness was seen when the  $F_{\text{acc}}$  was increased above a saturation value. This was the case, for example, of the mean height  $R_c$  for line- and cross-like patterns above 500  $\text{J}/\text{cm}^2$  of  $F_{\text{acc}}$ . Nevertheless, the mean height values observed in CLSM measurements were considerably lower than those values measured in the FIB images. The CLSM technique was not able to measure such high values of depth and the surface roughness parameters are not completely in concordance with the real topography.

High values of photocatalytic activity were found for many samples, in comparison with previous work. Line-like samples showed a degradation value higher than 60% for a sample irradiated with 500  $\text{J}/\text{cm}^2$  and 1650 pulses per point. Cross-like patterned samples achieved degradation values between 50% and 60% for  $F_{\text{acc}}$  of 500 and 750  $\text{J}/\text{cm}^2$ , while a degradation value greater than 70% was observed for a sample treated with 1000  $\text{J}/\text{cm}^2$  and 3300 pulses per point. In addition, the increase in the photocatalytic activity corresponds to higher values of surface roughness, which means a larger specific area, as it was confirmed when comparing  $S_a$  and S-ratio values measured by CLSM with  $C/C_0$  results measured by MB degradation experiment, for both line- and cross-like patterns.

Although the photocatalytic activity of the samples could be measured quantitatively, the repeatability of the characterization technique and the precision of the results must be optimized to obtain more reliable results. Electrochemical characterization and photocurrents measurements can be presented as complementary techniques to measure the true capacity of generation of electron-hole pairs and chemical interaction with the medium.

For a better understanding of the photocatalytic activity results described above, crystallographic characterization of the surface of the samples was carried out by GI-XRD and the present phases of titanium and its oxides were analyzed. According to the bibliography, the presence of rutile and anatase was expected for samples with high photocatalytic properties, and this was confirmed by the XRD results. Both, line- and cross-like samples exhibited a high presence of rutile and anatase when the accumulated fluence was greater than 500 J/cm<sup>2</sup>. When comparing the influence of  $n_{acc}$  for cross-like samples, it was seen that the change this parameter has a big influence on the oxide formation. The most interesting case was sample structured 500 J/cm<sup>2</sup>, where a low quantity of rutile and anatase was seen when using 1650 pulses per point, while the same  $F_{acc}$  was used but with  $n_{acc}$  of 3500 and a high amount of these oxides was found. This generated an important improvement of the photocatalytic activity of 25%.

The influence of the exposure of the sample surface to ultrasound was also analyzed to understand the stability of the oxide layer produced by laser patterning. The results showed that the superficial layer of oxides that was removed by ultrasonic cleaning in ethanol was mainly composed of rutile and anatase titanium dioxides. The loss of these two high photocatalytic active phases generated a significant change in the results of the MB degradation, leading to lower degradation capability after treatment, as mainly TiO and Ti<sub>2</sub>O<sub>3</sub> were found in the remanent layer.

After analyzing all samples,  $F_{acc}$  was observed to have a high influence on the surface properties (topography, chemistry, photocatalytic activity) when its value was increased from 100 to 500 J/cm<sup>2</sup>. For these values of  $F_{acc}$ , the value of  $n_{acc}$  and the kind of structure (lines or cross) did not show to be very influent on the final properties of the surface. This increase in the  $F_{acc}$  involved the formation of rutile and anatase and the surface roughness was also increased. The larger amount of photocatalytic active phases and the increase in the specific surface area (generated by the increase of the roughness) improved significantly the photocatalytic activity of the samples (both line- and cross-like patterned). Increments between 20% and 50% of the degradation efficiency were measured.

On the other hand, the influence of the structure and number of pulses per point ( $n_{acc}$ ) was higher when the value of  $F_{acc}$  was between 500 and 1000 J/cm<sup>2</sup>. For cross-like samples, the change in  $n_{acc}$  generated an increase in the roughness parameters and the generation of the anatase phase was also influenced, achieving important things in the photocatalytic activity of the samples. For line-like samples, the changes were also seen but it was slight in comparison. For this range of accumulated fluence,  $n_{acc}$  and the kind of structure used seem to play an important role on the resulting properties, while the change of  $F_{acc}$  did not show such an influence in the results of the experiments.

Some considerations for future work on this topic can be mentioned after the analysis of the results. XRD technique gave a lot of information about the generated phases and allowed the correlation of these results with the photocatalytic activity of the patterned samples. The complementation of this technique with other crystallographic techniques (XPS for instance) can involve a better and more precise understanding, and for this reason should be taken into account in future work. EDS on FIB cuts can give a more precise information about the location of the different oxides generated on the peaks and the valleys, by measuring the presence of oxygen and titanium atoms. TEM analysis with EBSD can give a better spatial resolution for the analysis of the structures and techniques like Raman and XPS can give for information about the 2D distribution of the oxides with a relative high precision.

This laser technology has a great potential for industrial applications in surface modification and the medical devices industry is one of the possible areas of application. One of the most important things to take into account in the next steps is the stability and repeatability of the samples. Stability is related to the above explained modification of the surface when a cleaning treatment by ultrasound under an ethanol bath is carried out. This change in the surface properties (loss of photocatalytic activity) should be avoided when highly active surfaces are developed. The optimal parameter setup should achieve

the highest possible stability. On the other side, repeatability is an essential factor when a laboratory scale process is scaled-up to an industrial process. Very precise analytical measurement and testing techniques should be used to assure more accurate results.

Finally, only 10  $\mu\text{m}$  periodicity samples were produced for this work and this parameter has a very important role when antibacterial applications are developed, as the bacteria size should be taken into account. Processing and testing of different periodicities and topographies (in addition to those analyzed in this work) can bring very interesting results. For the case of antibacterial applications, bacteria growth and degradation tests should be carried out for a better understanding of the relation between photocatalytic and antibacterial properties of titanium oxides.



## Bibliography

- [1] K.N. Kim, S.M. Lee, A. Mishra, G.Y. Yeom, Atmospheric pressure plasmas for surface modification of flexible and printed electronic devices: A review, *Thin Solid Films*. 598 (2016) 315–334. <https://doi.org/10.1016/J.TSF.2015.05.035>.
- [2] L. Miozzo, A. Yassar, G. Horowitz, Surface engineering for high performance organic electronic devices: the chemical approach, *J Mater Chem*. 20 (2010) 2513–2538. <https://doi.org/10.1039/B922385A>.
- [3] S. Ouyang, Y. Xie, D. Wang, D. Zhu, X. Xu, T. Tan, H.H. Fong, Surface patterning of PEDOT, *J Nanomater*. 2015 (2015). <https://doi.org/10.1155/2015/603148>.
- [4] I. Sotiri, J.C. Overton, A. Waterhouse, C. Howell, Immobilized liquid layers: A new approach to anti-adhesion surfaces for medical applications., <https://doi.org/10.1177/1535370216640942>. 241 (2016) 909–918. <https://doi.org/10.1177/1535370216640942>.
- [5] Y. Ikada, Surface modification of polymers for medical applications, *Biomaterials*. 15 (1994) 725–736. [https://doi.org/10.1016/0142-9612\(94\)90025-6](https://doi.org/10.1016/0142-9612(94)90025-6).
- [6] Y. Ikada, Surface modification of polymers for medical applications, *Biomaterials*. 15 (1994) 725–736. [https://doi.org/10.1016/0142-9612\(94\)90025-6](https://doi.org/10.1016/0142-9612(94)90025-6).
- [7] M.E. Beniakar, A.G. Sarigiannidis, P.E. Kakosimos, A.G. Kladas, Multiobjective evolutionary optimization of a surface mounted pm actuator with fractional slot winding for aerospace applications, *IEEE Trans Magn*. 50 (2014) 665–668. <https://doi.org/10.1109/TMAG.2013.2285497>.
- [8] A. Diaz, Surface texture characterization and optimization of metal additive manufacturing-produced components for aerospace applications, *Additive Manufacturing for the Aerospace Industry*. (2019) 341–374. <https://doi.org/10.1016/B978-0-12-814062-8.00018-2>.
- [9] W. Kaysser, Surface Modifications in Aerospace Applications, <http://dx.doi.org/10.1179/026708401101517926>. 17 (2013) 305–312. <https://doi.org/10.1179/026708401101517926>.
- [10] Z.A. Uwais, M.A. Hussein, M.A. Samad, N. Al-Aqeeli, Surface Modification of Metallic Biomaterials for Better Tribological Properties: A Review, *Arabian Journal for Science and Engineering* 2017 42:11. 42 (2017) 4493–4512. <https://doi.org/10.1007/S13369-017-2624-X>.
- [11] F. Findik, Latest progress on tribological properties of industrial materials, *Mater Des*. 57 (2014) 218–244. <https://doi.org/10.1016/J.MATDES.2013.12.028>.
- [12] H. Dong, T. Bell, State-of-the-art overview: ion beam surface modification of polymers towards improving tribological properties, *Surf Coat Technol*. 111 (1999) 29–40. [https://doi.org/10.1016/S0257-8972\(98\)00698-7](https://doi.org/10.1016/S0257-8972(98)00698-7).
- [13] Introduction to Reactor Design Fundamentals for Ideal Systems, Modeling of Chemical Kinetics and Reactor Design. (2001) 260–423. <https://doi.org/10.1016/B978-088415481-5/50007-3>.
- [14] A. Ziogas, G. Kolb, M. O'Connell, A. Attour, F. Lapique, M. Matlosz, S. Rode, Electrochemical microstructured reactors: Design and application in organic synthesis, *J Appl Electrochem*. 39 (2009) 2297–2313. <https://doi.org/10.1007/S10800-009-9939-6/FIGURES/16>.
- [15] Z. Dong, C. Delacour, K.M. Carogher, A.P. Udepurkar, S. Kuhn, Continuous Ultrasonic Reactors: Design, Mechanism and Application, *Materials* 2020, Vol. 13, Page 344. 13 (2020) 344. <https://doi.org/10.3390/MA13020344>.
- [16] D.S. Gnanamuthu, Laser Surface Treatment, *Optical Engineering*. 19 (1980) 783–792. <https://doi.org/10.1117/12.7972604>.

- [17] M.A. Montealegre, G. Castro, P. Rey, J.L. Arias, P. Vázquez, M. González, Surface treatments by laser technology, *Contemp Mater.* (2010). <https://doi.org/10.5767/anurs.cmat.100101.en.019M>.
- [18] L. Hao, J. Lawrence, *Laser Surface Treatment of Bio-Implant Materials*, John Wiley & Sons Ltd. (2005).
- [19] M. Özcan, C. Hämmerle, Titanium as a reconstruction and implant material in dentistry: Advantages and pitfalls, *Materials*. 5 (2012) 1528–1545. <https://doi.org/10.3390/MA5091528>.
- [20] A. Jemat, M.J. Ghazali, M. Razali, Y. Otsuka, Surface modifications and their effects on titanium dental implants, *Biomed Res Int*. 2015 (2015). <https://doi.org/10.1155/2015/791725>.
- [21] C. Yan Guo, A.T.H. Tang, J.P. Matinlinna, Insights into surface treatment methods of titanium dental implants, *J Adhes Sci Technol*. 26 (2012) 189–205. <https://doi.org/10.1163/016942411X569390>.
- [22] S. Roehling, K.A. Schlegel, H. Woelfler, M. Gahlert, Zirconia compared to titanium dental implants in preclinical studies—A systematic review and meta-analysis, *Clin Oral Implants Res*. 30 (2019) 365–395. <https://doi.org/10.1111/CLR.13425>.
- [23] T. Tsumura, N. Kojitani, I. Izumi, N. Iwashita, M. Toyoda, M. Inagaki, Carbon coating of anatase-type TiO<sub>2</sub> and photoactivity, *J Mater Chem*. 12 (2002) 1391–1396. <https://doi.org/10.1039/B201942F>.
- [24] T. Torimoto, S. Ito, S. Kuwabata, H. Yoneyama, Effects of Adsorbents Used as Supports for Titanium Dioxide Loading on Photocatalytic Degradation of Propylamide, *Environ Sci Technol*. 30 (1996) 1275–1281. <https://doi.org/10.1021/ES950483K>.
- [25] C. Minero, F. Catozzo, E. Pelizzetti, Role of adsorption in photocatalyzed reactions of organic molecules in aqueous titania suspensions, *Langmuir*. 8 (2002) 481–486. <https://doi.org/10.1021/LA00038A029>.
- [26] L. Zang, W. Macyk, C. Lange, W.F. Maier, C. Antonius, D. Meissner, H. Kisch, Visible-Light Detoxification and Charge Generation by Transition Metal Chloride Modified Titania, (n.d.). [https://doi.org/10.1002/\(SICI\)1521-3765\(20000117\)6:2](https://doi.org/10.1002/(SICI)1521-3765(20000117)6:2).
- [27] Y. Zhang, Z.R. Tang, X. Fu, Y.J. Xu, TiO<sub>2</sub>-graphene nanocomposites for gas-phase photocatalytic degradation of volatile aromatic pollutant: Is TiO<sub>2</sub>-graphene truly different from other TiO<sub>2</sub>-carbon composite materials?, *ACS Nano*. 4 (2010) 7303–7314. [https://doi.org/10.1021/NN1024219/SUPPL\\_FILE/NN1024219\\_SI\\_001.PDF](https://doi.org/10.1021/NN1024219/SUPPL_FILE/NN1024219_SI_001.PDF).
- [28] H. Irie, Y. Watanabe, K. Hashimoto, Carbon-doped Anatase TiO<sub>2</sub> Powders as a Visible-light Sensitive Photocatalyst, <Http://Dx.Doi.Org/10.1246/Cl.2003.772>. 32 (2003) 772–773. <https://doi.org/10.1246/CL.2003.772>.
- [29] R. Nakamura, T. Tanaka, Y. Nakato, Mechanism for Visible Light Responses in Anodic Photocurrents at N-Doped TiO<sub>2</sub> Film Electrodes, *Journal of Physical Chemistry B*. 108 (2004) 10617–10620. <https://doi.org/10.1021/JP048112Q>.
- [30] S. Sakthivel, H. Kisch, Daylight Photocatalysis by Carbon-Modified Titanium Dioxide, *Angewandte Chemie International Edition*. 42 (2003) 4908–4911. <https://doi.org/10.1002/ANIE.200351577>.
- [31] D.W. Müller, T. Fox, P.G. Grützmacher, S. Suarez, F. Mücklich, Applying Ultrashort Pulsed Direct Laser Interference Patterning for Functional Surfaces, *Sci Rep*. 10 (2020). <https://doi.org/10.1038/s41598-020-60592-4>.
- [32] M.S. Brown, C.B. Arnold, *Fundamentals of Laser-Material Interaction and Application to Multiscale Surface Modification*, Springer Series in Materials Science. 135 (2010) 91–120. [https://doi.org/10.1007/978-3-642-10523-4\\_4](https://doi.org/10.1007/978-3-642-10523-4_4).

- [33] L. Skowronski, Optical Properties of Titanium in the Regime of the Limited Light Penetration, *Materials*. 13 (2020). <https://doi.org/10.3390/MA13040952>.
- [34] S. Nolte, F. Schrepel, F. Dausinger, *Ultrashort Pulse Laser Technology*, Springer International Publishing, Cham, 2016. <https://doi.org/10.1007/978-3-319-17659-8>.
- [35] J.-Claude. Diels, W. Rudolph, *Ultrashort laser pulse phenomena : fundamentals, techniques, and applications on a femtosecond time scale*, Elsevier. (2006) 652.
- [36] C. Dorman, Picosecond Micromachining Update unique fiber-based laser technology delivers high pulse energy and average power, *Laser Tech.* (2008).
- [37] S.I. Anisimov, B. Rethfeld, Theory of ultrashort laser pulse interaction with a metal, <https://doi.org/10.1117/12.271674>. 3093 (1997) 192–203. <https://doi.org/10.1117/12.271674>.
- [38] M. Winkler, *Non-equilibrium chalcogen concentrations in silicon: Physical structure, electronic transport, and photovoltaic potential*, 2010.
- [39] C.W. Siders, A. Cavalleri, K. Sokolowski-Tinten, C. Tóth, T. Guo, M. Kammler, M. Horn Von Hoegen, K.R. Wilson, D. von der Linde, C.P.J. Barty, Detection of nonthermal melting by ultrafast x-ray diffraction, *Science* (1979). 286 (1999) 1340–1342. <https://doi.org/10.1126/SCIENCE.286.5443.1340>.
- [40] K.H. Leitz, B. Redlingshöer, Y. Reg, A. Otto, M. Schmidt, Metal ablation with short and ultrashort laser pulses, *Phys Procedia*. 12 (2011) 230–238. <https://doi.org/10.1016/J.PHPRO.2011.03.128>.
- [41] K.C. Phillips, H.H. Gandhi, E. Mazur, S.K. Sundaram, Ultrafast laser processing of materials: a review, *Adv Opt Photonics*. (2015). <https://doi.org/10.1364/AOP.7.000684>.
- [42] P.M. Delfino, *Investigation of the photocatalytic activity of laser patterned titanium*, Universität des Saarlandes, 2021.
- [43] G. Račiukaitis, P. Gečys, Picosecond-Laser Structuring of Thin Films for CIGS Solar Cells, 5th International Congress on Laser Advanced Materials Processing . (2010). <https://doi.org/10.2961/jlmm.2010.01.0003>.
- [44] D.C. Wu, M.P. Goldman, H. Wat, H.H.L. Chan, A Systematic Review of Picosecond Laser in Dermatology: Evidence and Recommendations, *Lasers Surg Med*. 53 (2021) 9–49. <https://doi.org/10.1002/LSM.23244>.
- [45] R. Weichenhain, J. Jandeleit, A. Horn, E.W. Kreutz, R. Poprawe, Drilling of ceramics and polymers by diode pumped solid state lasers, *International Congress on Applications of Lasers & Electro-Optics*. 1997 (2018) B73. <https://doi.org/10.2351/1.5059639>.
- [46] M.H. Niemz, Cavity Preparation with the Nd:YLF Picosecond Laser, *J Dent Res*. 74 (1995) 1194–1199. <https://doi.org/10.1177/00220345950740050801>.
- [47] T. Okada, N. Malaga, W. Baumann, A. Siemiarczuk, Picosecond Laser Spectroscopy of 4-(9-Anthryl)-A,W-dimethylaniline and Related Compounds, *J. Phys. Chem.* 91 (1987) 4490–4495. <https://pubs.acs.org/sharingguidelines> (accessed January 6, 2022).
- [48] J. Bonse, S. v. Kirner, J. Krüger, Laser-Induced Periodic Surface Structures (LIPSS), *Handbook of Laser Micro- and Nano-Engineering*. (2021) 1–59. [https://doi.org/10.1007/978-3-319-69537-2\\_17-2](https://doi.org/10.1007/978-3-319-69537-2_17-2).
- [49] A. Rosenfeld, J. Krüger, J. Bonse, S. Höhm, Laser-induced periodic surface structures on titanium upon single- and two-color femtosecond double-pulse irradiation, *Optics Express*, Vol. 23, Issue 20, Pp. 25959–25971. 23 (2015) 25959–25971. <https://doi.org/10.1364/OE.23.025959>.
- [50] T. Kunze, A.F. Lasagni, Direct laser interference patterning: from fundamentals to industrial applications, *Lasers in Manufacturing Conference*. (2017).

- [51] A. Lasagni, *Advanced Design of Periodical Structures by Laser Interference Metallurgy in the Micro/Nano Scale on Macroscopic Areas*, Universität des Saarlandes, 2007.
- [52] Y. Zheng, Z. An, P. Smyrek, H.J. Seifert, T. Kunze, V. Lang, A.-F. Lasagni, W. Pfleging, Direct laser interference patterning and ultrafast laser-induced micro/nano structuring of current collectors for lithium-ion batteries, *Laser-Based Micro- and Nanoprocessing X*. 9736 (2016) 97361B. <https://doi.org/10.1117/12.2220111>.
- [53] S. Alamri, A.I. Aguilar-Morales, A.F. Lasagni, Controlling the wettability of polycarbonate substrates by producing hierarchical structures using Direct Laser Interference Patterning, *Eur Polym J*. 99 (2018) 27–37. <https://doi.org/10.1016/J.EURPOLYMJ.2017.12.001>.
- [54] D. Huerta-Murillo, A.I. Aguilar-Morales, S. Alamri, J.T. Cardoso, R. Jagdheesh, A.F. Lasagni, J.L. Ocaña, Fabrication of multi-scale periodic surface structures on Ti-6Al-4V by direct laser writing and direct laser interference patterning for modified wettability applications, *OptLE*. 98 (2017) 134–142. <https://doi.org/10.1016/J.OPTLASENG.2017.06.017>.
- [55] D. Guenther, J. Valle, S. Burgui, C. Gil, C. Solano, A. Toledo-Arana, R. Helbig, C. Werner, I. Lasa, A.F. Lasagni, Direct laser interference patterning for decreased bacterial attachment, *Laser-Based Micro- and Nanoprocessing X*. 9736 (2016) 973611. <https://doi.org/10.1117/12.2216065>.
- [56] Y. Lan, Y. Lu, Z. Ren, Mini review on photocatalysis of titanium dioxide nanoparticles and their solar applications, *Nano Energy*. 2 (2013) 1031–1045. <https://doi.org/10.1016/J.NANOEN.2013.04.002>.
- [57] S.G. Kumar, K.S.R.K. Rao, Comparison of modification strategies towards enhanced charge carrier separation and photocatalytic degradation activity of metal oxide semiconductors (TiO<sub>2</sub>, WO<sub>3</sub> and ZnO), *Appl Surf Sci*. 391 (2017) 124–148. <https://doi.org/10.1016/J.APSUSC.2016.07.081>.
- [58] H. Okamoto, O-Ti (Oxygen-Titanium), *J Phase Equilibria Diffus*. 32 (2011) 473–474. <https://doi.org/10.1007/S11669-011-9935-5/TABLES/1>.
- [59] D.C. Lynch, D.E. Bullard, Phase equilibria in the titanium-oxygen system, *Metallurgical and Materials Transactions B* 1997 28:3. 28 (1997) 447–453. <https://doi.org/10.1007/S11663-997-0111-6>.
- [60] P. Waldner, G. Eriksson, Thermodynamic modelling of the system titanium-oxygen, *Calphad*. 23 (1999) 189–218. [https://doi.org/10.1016/S0364-5916\(99\)00025-5](https://doi.org/10.1016/S0364-5916(99)00025-5).
- [61] S. Andersson, B. Collén, U. Kuylenstierna, A. Magnéli, A. Magnéli, H. Pestmalis, S. Åsbrink, PHASE ANALYSIS STUDIES ON THE TITANIUM-OXYGEN SYSTEM, *Acta Chemica Scandinavica (Denmark)* Divided into *Acta Chem. Scand.*, Ser. A and Ser. B. Vol: 11 (1957) 1641–1652. <https://doi.org/10.3891/ACTA.CHEM.SCAND.11-1641>.
- [62] M. Cancarevic, M. Zinkevich, F. Aldinger, Thermodynamic description of the Ti-O system using the associate model for the liquid phase, *CALPHAD*. 31 (2007) 330–342. <https://doi.org/10.1016/J.CALPHAD.2007.01.009>.
- [63] Y. Li, Y. Yang, X. Shu, D. Wan, N. Wei, X. Yu, M.B.H. Breese, T. Venkatesan, J.M. Xue, Y. Liu, S. Li, T. Wu, J. Chen, From Titanium Sesquioxide to Titanium Dioxide: Oxidation-Induced Structural, Phase, and Property Evolution, *Chemistry of Materials*. 30 (2018) 4383–4392. [https://doi.org/10.1021/ACS.CHEMMATER.8B01739/SUPPL\\_FILE/CM8B01739\\_SI\\_001.PDF](https://doi.org/10.1021/ACS.CHEMMATER.8B01739/SUPPL_FILE/CM8B01739_SI_001.PDF).
- [64] S. Bartkowski, M. Neumann, E. Kurmaev, V. Fedorenko, S. Shamin, V. Cherkashenko, S. Nemnonov, Electronic structure of titanium monoxide, *Phys Rev B Condens Matter Mater Phys*. 56 (1997) 10656–10667. <https://doi.org/10.1103/PHYSREVB.56.10656>.
- [65] M.D. Banus, T.B. Reed, A.J. Strauss, Electrical and magnetic properties of TiO and VO, *Phys Rev B*. 5 (1972) 2775–2784. <https://doi.org/10.1103/PHYSREVB.5.2775>.

- [66] S.P. Denker, Electronic Properties of Titanium Monoxide, *J Appl Phys.* 37 (2004) 142. <https://doi.org/10.1063/1.1707796>.
- [67] L. Hao, J. Lawrence, *Laser Surface Treatment of Bio-Implant Materials*, John Wiley & Sons Ltd. (2005). [www.wiley.com](http://www.wiley.com) (accessed January 6, 2022).
- [68] M.J. Yaszemski, R.G. Payne, W.C. Hayes, R. Langer, A.G. Mikos, Evolution of bone transplantation: molecular, cellular and tissue strategies to engineer human bone, *Biomaterials.* 17 (1996) 175–185. [https://doi.org/10.1016/0142-9612\(96\)85762-0](https://doi.org/10.1016/0142-9612(96)85762-0).
- [69] R.J. Friedman, J. Black, J.O. Galante, J.J. Jacobs, H.B. Skinner, Current concepts in orthopaedic biomaterials and implant fixation, *Journal of Bone and Joint Surgery.* 75 (1993) 1086–1109. <https://doi.org/10.2106/00004623-199412000-00018>.
- [70] G.W. Hastings, F.A. Mahmud, *Intelligent Orthopaedic Materials*, *J Intell Mater Syst Struct.* 4 (2016) 452–456. <https://doi.org/10.1177/1045389X9300400402>.
- [71] X. Liu, P.K. Chu, C. Ding, Surface modification of titanium, titanium alloys, and related materials for biomedical applications, *Materials Science and Engineering R: Reports.* 47 (2004) 49–121. <https://doi.org/10.1016/J.MSER.2004.11.001>.
- [72] K.Y. Hung, S.C. Lo, C.S. Shih, Y.C. Yang, H.P. Feng, Y.C. Lin, Titanium surface modified by hydroxyapatite coating for dental implants, *Surf Coat Technol.* 231 (2013) 337–345. <https://doi.org/10.1016/J.SURFCOAT.2012.03.037>.
- [73] G. Wang, J. Li, K. Lv, W. Zhang, X. Ding, G. Yang, X. Liu, X. Jiang, Surface thermal oxidation on titanium implants to enhance osteogenic activity and in vivo osseointegration, *Sci Rep.* 6 (2016). <https://doi.org/10.1038/srep31769>.
- [74] G. Peto, A. Karacs, Z. Pászti, L. Guczi, T. Divinyi, A. Joób, Surface treatment of screw shaped titanium dental implants by high intensity laser pulses, *Appl Surf Sci.* 186 (2002) 7–13. [https://doi.org/10.1016/S0169-4332\(01\)00769-3](https://doi.org/10.1016/S0169-4332(01)00769-3).
- [75] F. Villermaux, M. Tabrizian, L. Yahia, M. Meunier, D.L. Piron, Excimer laser treatment of NiTi shape memory alloy biomaterials, *Appl Surf Sci.* 109–110 (1997) 62–66. [https://doi.org/10.1016/S0169-4332\(96\)00619-8](https://doi.org/10.1016/S0169-4332(96)00619-8).
- [76] R. Vilar, A. Almeida, Laser surface treatment of biomedical alloys, *Laser Surface Modification of Biomaterials: Techniques and Applications.* (2016) 35–75. <https://doi.org/10.1016/B978-0-08-100883-6.00002-2>.
- [77] B. van Hooreweder, Y. Apers, K. Lietaert, J.P. Kruth, Improving the fatigue performance of porous metallic biomaterials produced by Selective Laser Melting, *Acta Biomater.* 47 (2017) 193–202. <https://doi.org/10.1016/J.ACTBIO.2016.10.005>.
- [78] L. Hao, J. Lawrence, Y.F. Phua, K.S. Chian, G.C. Lim, H.Y. Zheng, Enhanced human osteoblast cell adhesion and proliferation on 316 LS stainless steel by means of CO<sub>2</sub> laser surface treatment, *J Biomed Mater Res B Appl Biomater.* 73B (2005) 148–156. <https://doi.org/10.1002/JBM.B.30194>.
- [79] W.M. Steen, *Laser Material Processing*, *Laser Material Processing.* (2003). <https://doi.org/10.1007/978-1-4471-3752-8>.
- [80] V. Rodríguez-González, C. Terashima, A. Fujishima, Applications of photocatalytic titanium dioxide-based nanomaterials in sustainable agriculture, *Journal of Photochemistry and Photobiology C: Photochemistry Reviews.* 40 (2019) 49–67. <https://doi.org/10.1016/J.JPHOTOCHEMREV.2019.06.001>.
- [81] G. Sberveglieri, E. Comini, G. Faglia, M.Z. Atashbar, W. Wlodarski, Titanium dioxide thin films prepared for alcohol microsensor applications, *Sens Actuators B Chem.* 66 (2000) 139–141. [https://doi.org/10.1016/S0925-4005\(00\)00328-2](https://doi.org/10.1016/S0925-4005(00)00328-2).

- [82] R. Saleh, N. Putra, R.E. Wibowo, W.N. Septiadi, S.P. Prakoso, Titanium dioxide nanofluids for heat transfer applications, *Exp Therm Fluid Sci.* 52 (2014) 19–29. <https://doi.org/10.1016/J.EXPTHERMFLUSCI.2013.08.018>.
- [83] W. Kangwansupamonkon, V. Lauruengtana, S. Surassmo, U. Ruktanonchai, Antibacterial effect of apatite-coated titanium dioxide for textiles applications, *Nanomedicine.* 5 (2009) 240–249. <https://doi.org/10.1016/J.NANO.2008.09.004>.
- [84] K.P. Gopinath, N.V. Madhav, A. Krishnan, R. Malolan, G. Rangarajan, Present applications of titanium dioxide for the photocatalytic removal of pollutants from water: A review, *J Environ Manage.* 270 (2020) 110906. <https://doi.org/10.1016/J.JENVMAN.2020.110906>.
- [85] C.C. Chen, H.W. Chung, C.H. Chen, H.P. Lu, C.M. Lan, S.F. Chen, L. Luo, C.S. Hong, E.W.G. Diau, Fabrication and characterization of anodic titanium oxide nanotube arrays of controlled length for highly efficient dye-sensitized solar cells, *Journal of Physical Chemistry C.* 112 (2008) 19151–19157. [https://doi.org/10.1021/JP806281R/SUPPL\\_FILE/JP806281R\\_SI\\_001.PDF](https://doi.org/10.1021/JP806281R/SUPPL_FILE/JP806281R_SI_001.PDF).
- [86] Z. Youssef, R. Vanderesse, L. Colombeau, F. Baros, T. Roques-Carmes, C. Frochot, H. Wahab, J. Toufaily, T. Hamieh, S. Acherar, A.M. Gazzali, The application of titanium dioxide, zinc oxide, fullerene, and graphene nanoparticles in photodynamic therapy, *Cancer Nanotechnology* 2017 8:1. 8 (2017) 1–62. <https://doi.org/10.1186/S12645-017-0032-2>.
- [87] N.P. Shetti, S.D. Bukkitgar, K.R. Reddy, C.V. Reddy, T.M. Aminabhavi, Nanostructured titanium oxide hybrids-based electrochemical biosensors for healthcare applications, *Colloids Surf B Biointerfaces.* 178 (2019) 385–394. <https://doi.org/10.1016/J.COLSURFB.2019.03.013>.
- [88] Catalysis - an overview | ScienceDirect Topics, (n.d.). <https://www.sciencedirect.com/topics/materials-science/catalysis> (accessed January 14, 2022).
- [89] Photocatalysis - Latest research and news | Nature, (n.d.). <https://www.nature.com/subjects/photocatalysis> (accessed January 14, 2022).
- [90] R. Ameta, M.S. Solanki, S. Benjamin, S.C. Ameta, Photocatalysis, *Advanced Oxidation Processes for Wastewater Treatment: Emerging Green Chemical Technology.* (2018) 135–175. <https://doi.org/10.1016/B978-0-12-810499-6.00006-1>.
- [91] J.M. Herrmann, Heterogeneous photocatalysis: Fundamentals and applications to the removal of various types of aqueous pollutants, *Catal Today.* 53 (1999) 115–129. [https://doi.org/10.1016/S0920-5861\(99\)00107-8](https://doi.org/10.1016/S0920-5861(99)00107-8).
- [92] J.M. Herrmann, Heterogeneous photocatalysis: State of the art and present applications, *Top Catal.* 34 (2005) 49–65. <https://doi.org/10.1007/S11244-005-3788-2>.
- [93] A. Fujishima, T.N. Rao, D.A. Tryk, Titanium dioxide photocatalysis, *Journal of Photochemistry and Photobiology C: Photochemistry Reviews.* 1 (2000) 1–21. [https://doi.org/10.1016/S1389-5567\(00\)00002-2](https://doi.org/10.1016/S1389-5567(00)00002-2).
- [94] P. Magalhães, L. Andrade, O.C. Nunes, A. Mendes, TITANIUM DIOXIDE PHOTOCATALYSIS: FUNDAMENTALS AND APPLICATION ON PHOTOINACTIVATION, (2017).
- [95] O. Carp, C.L. Huisman, A. Reller, Photoinduced reactivity of titanium dioxide, *Progress in Solid State Chemistry.* 32 (2004) 33–177. <https://doi.org/10.1016/j.progsolidstchem.2004.08.001>.
- [96] C. Yogi, K. Kojima, N. Wada, H. Tokumoto, T. Takai, T. Mizoguchi, H. Tamiaki, Photocatalytic degradation of methylene blue by TiO<sub>2</sub> film and Au particles-TiO<sub>2</sub> composite film, *Thin Solid Films.* 516 (2008) 5881–5884. <https://doi.org/10.1016/J.TSF.2007.10.050>.
- [97] C.H. Wu, J.M. Chern, Kinetics of Photocatalytic Decomposition of Methylene Blue, *Ind Eng Chem Res.* 45 (2006) 6450–6457. <https://doi.org/10.1021/IE0602759>.

- [98] S. Lakshmi, R. Renganathan, S. Fujita, Study on TiO<sub>2</sub>-mediated photocatalytic degradation of methylene blue, *J Photochem Photobiol A Chem.* 88 (1995) 163–167. [https://doi.org/10.1016/1010-6030\(94\)04030-6](https://doi.org/10.1016/1010-6030(94)04030-6).
- [99] A. Houas, H. Lachheb, M. Ksibi, E. Elaloui, C. Guillard, J.M. Herrmann, Photocatalytic degradation pathway of methylene blue in water, *Appl Catal B.* 31 (2001) 145–157. [https://doi.org/10.1016/S0926-3373\(00\)00276-9](https://doi.org/10.1016/S0926-3373(00)00276-9).
- [100] F.L. Toma, S. Alamri, B. Leupolt, T. Kunze, M. Barbosa, Functionalization of Suspension Sprayed HVOF TiO<sub>2</sub> Coatings by Direct Laser Interference Patterning, *Journal of Thermal Spray Technology.* 30 (2021) 1159–1173. <https://doi.org/10.1007/s11666-021-01181-3>.
- [101] H. Nakajima, T. Mori, Q. Shen, T. Toyoda, Photoluminescence study of mixtures of anatase and rutile TiO<sub>2</sub> nanoparticles: Influence of charge transfer between the nanoparticles on their photoluminescence excitation bands, *Chem Phys Lett.* 409 (2005) 81–84. <https://doi.org/10.1016/J.CPLETT.2005.04.093>.
- [102] Y. Nosaka, A.Y. Nosaka, Generation and Detection of Reactive Oxygen Species in Photocatalysis, *Chem Rev.* 117 (2017) 11302–11336. <https://doi.org/10.1021/ACS.CHEMREV.7B00161>.
- [103] S.G. Kumar, L.G. Devi, Review on Modified TiO<sub>2</sub> Photocatalysis under UV/Visible Light: Selected Results and Related Mechanisms on Interfacial Charge Carrier Transfer Dynamics, *Journal of Physical Chemistry A.* 115 (2011) 13211–13241. <https://doi.org/10.1021/JP204364A>.
- [104] W. Wang, Z. Wang, J. Liu, Z. Luo, S.L. Suib, P. He, G. Ding, Z. Zhang, L. Sun, Single-step One-pot Synthesis of TiO<sub>2</sub> Nanosheets Doped with Sulfur on Reduced Graphene Oxide with Enhanced Photocatalytic Activity, *Scientific Reports* 2017 7:1. 7 (2017) 1–9. <https://doi.org/10.1038/srep46610>.
- [105] D.O. Scanlon, C.W. Dunnill, J. Buckeridge, S.A. Shevlin, A.J. Logsdail, S.M. Woodley, C.R.A. Catlow, M.J. Powell, R.G. Palgrave, I.P. Parkin, G.W. Watson, T.W. Keal, P. Sherwood, A. Walsh, A.A. Sokol, Band alignment of rutile and anatase TiO<sub>2</sub>, *Nature Materials* 2013 12:9. 12 (2013) 798–801. <https://doi.org/10.1038/nmat3697>.
- [106] M.A. Henderson, A surface science perspective on TiO<sub>2</sub> photocatalysis, *Surf Sci Rep.* 66 (2011) 185–297. <https://doi.org/10.1016/J.SURFREP.2011.01.001>.
- [107] W.N. Zhao, S.C. Zhu, Y.F. Li, Z.P. Liu, Three-phase junction for modulating electron–hole migration in anatase–rutile photocatalysts, *Chem Sci.* 6 (2015) 3483–3494. <https://doi.org/10.1039/C5SC00621J>.
- [108] T. Kawahara, Y. Konishi, H. Tada, N. Tohge, J. Nishii, S. Ito, A Patterned TiO<sub>2</sub> (Anatase)/TiO<sub>2</sub> (Rutile) Bilayer-Type Photocatalyst: Effect of the Anatase/Rutile Junction on the Photocatalytic Activity, 2002. [https://doi.org/10.1002/1521-3773\(20020802\)41:15<2811::AID-ANIE2811>3.0.CO;2](https://doi.org/10.1002/1521-3773(20020802)41:15<2811::AID-ANIE2811>3.0.CO;2).
- [109] T. Miyagi, M. Kamei, T. Mitsuhashi, T. Ishigaki, A. Yamazaki, Charge separation at the rutile/anatase interface: A dominant factor of photocatalytic activity, *Chem Phys Lett.* 390 (2004) 399–402. <https://doi.org/10.1016/J.CPLETT.2004.04.042>.
- [110] Y. Nosaka, A.Y. Nosaka, Reconsideration of Intrinsic Band Alignments within Anatase and Rutile TiO<sub>2</sub>, *Journal of Physical Chemistry Letters.* 7 (2016) 431–434. [https://doi.org/10.1021/ACS.JPCLETT.5B02804/SUPPL\\_FILE/JZ5B02804\\_SI\\_001.PDF](https://doi.org/10.1021/ACS.JPCLETT.5B02804/SUPPL_FILE/JZ5B02804_SI_001.PDF).
- [111] D. Zhang, S. Dong, Challenges in band alignment between semiconducting materials: A case of rutile and anatase TiO<sub>2</sub>, *Progress in Natural Science: Materials International.* 29 (2019) 277–284. <https://doi.org/10.1016/J.PNSC.2019.03.012>.
- [112] K.C. Ko, S.T. Bromley, J.Y. Lee, F. Illas, Size-Dependent Level Alignment between Rutile and Anatase TiO<sub>2</sub> Nanoparticles: Implications for Photocatalysis, *Journal of Physical Chemistry*

- [113] H. Liu, W. Yang, Y. Ma, J. Yao, Extended visible light response of binary TiO<sub>2</sub>-Ti<sub>2</sub>O<sub>3</sub> photocatalyst prepared by a photo-assisted sol-gel method, *Appl Catal A Gen.* 299 (2006) 218–223. <https://doi.org/10.1016/J.APCATA.2005.10.041>.
- [114] M. Tian, M. Mahjouri-Samani, K. Wang, A.A. Poretzky, D.B. Geohegan, W.D. Tennyson, N. Cross, C.M. Rouleau, T.A. Zawodzinski, G. Duscher, G. Eres, Black Anatase Formation by Annealing of Amorphous Nanoparticles and the Role of the Ti<sub>2</sub>O<sub>3</sub> Shell in Self-Organized Crystallization by Particle Attachment, *ACS Appl Mater Interfaces.* 9 (2017) 22018–22025. [https://doi.org/10.1021/ACSAMI.7B02764/SUPPL\\_FILE/AM7B02764\\_SI\\_001.PDF](https://doi.org/10.1021/ACSAMI.7B02764/SUPPL_FILE/AM7B02764_SI_001.PDF).
- [115] M. Xu, A. Zada, R. Yan, H. Li, N. Sun, Y. Qu, Ti<sub>2</sub>O<sub>3</sub>/TiO<sub>2</sub> heterophase junctions with enhanced charge separation and spatially separated active sites for photocatalytic CO<sub>2</sub> reduction, *Physical Chemistry Chemical Physics.* 22 (2020) 4526–4532. <https://doi.org/10.1039/C9CP05147C>.
- [116] R. Dagherir, P. Drogui, D. Robert, Modified TiO<sub>2</sub> for environmental photocatalytic applications: A review, *Ind Eng Chem Res.* 52 (2013) 3581–3599. <https://doi.org/10.1021/IE303468T>.
- [117] S. Rehman, R. Ullah, A.M. Butt, N.D. Gohar, Strategies of making TiO<sub>2</sub> and ZnO visible light active, *J Hazard Mater.* 170 (2009) 560–569. <https://doi.org/10.1016/J.JHAZMAT.2009.05.064>.
- [118] A. Fujishima, K. Honda, Electrochemical Photolysis of Water at a Semiconductor Electrode, *Nature* 1972 238:5358. 238 (1972) 37–38. <https://doi.org/10.1038/238037a0>.
- [119] T. Inoue, A. Fujishima, S. Konishi, K. Honda, Photoelectrocatalytic reduction of carbon dioxide in aqueous suspensions of semiconductor powders, *Nature* 1979 277:5698. 277 (1979) 637–638. <https://doi.org/10.1038/277637a0>.
- [120] L. Caballero, K.A. Whitehead, N.S. Allen, J. Verran, Inactivation of *Escherichia coli* on immobilized TiO<sub>2</sub> using fluorescent light, *J Photochem Photobiol A Chem.* 202 (2009) 92–98. <https://doi.org/10.1016/J.JPHOTOCHEM.2008.11.005>.
- [121] R. Cai, K. Hashimoto, K. Itoh, Y. Kubota, A. Fujishima, Photokilling of Malignant Cells with Ultrafine TiO<sub>2</sub> Powder, <http://Dx.Doi.Org/10.1246/Bcsj.64.1268>. 64 (2006) 1268–1273. <https://doi.org/10.1246/BCSJ.64.1268>.
- [122] T. Matsunaga, R. Tomoda, T. Nakajima, H. Wake, Photoelectrochemical sterilization of microbial cells by semiconductor powders, *FEMS Microbiol Lett.* 29 (1985) 211–214. <https://doi.org/10.1111/J.1574-6968.1985.TB00864.X>.
- [123] C. McCullagh, J.M.C. Robertson, D.W. Bahnemann, P.K.J. Robertson, The application of TiO<sub>2</sub> photocatalysis for disinfection of water contaminated with pathogenic micro-organisms: a review, *Research on Chemical Intermediates* 2007 33:3. 33 (2007) 359–375. <https://doi.org/10.1163/156856707779238775>.
- [124] J.R. Peller, R.L. Whitman, S. Griffith, P. Harris, C. Peller, J. Scalzitti, TiO<sub>2</sub> as a photocatalyst for control of the aquatic invasive alga, *Cladophora*, under natural and artificial light, *J Photochem Photobiol A Chem.* 186 (2007) 212–217. <https://doi.org/10.1016/J.JPHOTOCHEM.2006.08.009>.
- [125] K. Sunada, Y. Kikuchi, K. Hashimoto, A. Fujishima, Bactericidal and Detoxification Effects of TiO<sub>2</sub> Thin Film Photocatalysts, *Environ Sci Technol.* 32 (1998) 726–728. <https://doi.org/10.1021/ES970860O>.
- [126] K. Sunada, T. Watanabe, K. Hashimoto, Studies on photokilling of bacteria on TiO<sub>2</sub> thin film, *J Photochem Photobiol A Chem.* 156 (2003) 227–233. [https://doi.org/10.1016/S1010-6030\(02\)00434-3](https://doi.org/10.1016/S1010-6030(02)00434-3).



- [127] K. Sunada, T. Watanabe, K. Hashimoto, Bactericidal Activity of Copper-Deposited TiO<sub>2</sub> Thin Film under Weak UV Light Illumination, *Environ Sci Technol.* 37 (2003) 4785–4789. <https://doi.org/10.1021/ES034106G>.
- [128] E.J. Wolfrum, J. Huang, D.M. Blake, P.C. Maness, Z. Huang, J. Fiest, W.A. Jacoby, Photocatalytic Oxidation of Bacteria, Bacterial and Fungal Spores, and Model Biofilm Components to Carbon Dioxide on Titanium Dioxide-Coated Surfaces, *Environ Sci Technol.* 36 (2002) 3412–3419. <https://doi.org/10.1021/ES011423J>.
- [129] T. Fox, *Handbook Picosecond DLIP*, 2020.
- [130] A. Pérez Del Pino, P. Serra, J.L. Morenza, Coloring of titanium by pulsed laser processing in air, *Thin Solid Films.* 415 (2002) 201–205. [https://doi.org/10.1016/S0040-6090\(02\)00632-6](https://doi.org/10.1016/S0040-6090(02)00632-6).
- [131] A. Pérez Del Pino, P. Serra, J.L. Morenza, Oxidation of titanium through Nd:YAG laser irradiation, *Appl Surf Sci.* 197–198 (2002) 887–890. [https://doi.org/10.1016/S0169-4332\(02\)00447-6](https://doi.org/10.1016/S0169-4332(02)00447-6).
- [132] A. Pérez del Pino, J.M. Fernández-Pradas, P. Serra, J.L. Morenza, Coloring of titanium through laser oxidation: comparative study with anodizing, *Surf Coat Technol.* 187 (2004) 106–112. <https://doi.org/10.1016/J.SURFCOAT.2004.02.001>.
- [133] W. García Herrera, *Ultra-Short Pulsed Direct Laser Interference Patterning of Titanium Surfaces for Functional Anti-bacterial Effect*, Universität des Saarlandes, 2020.
- [134] 3D Measuring Laser Microscope OLS4100 Bringing Answers to the Surface, (n.d.).
- [135] P. Rohwetter, J. Yu, G. Méjean, K. Stelmazczyk, E. Salmon, J. Kasparian, J.P. Wolf, L. Wöste, Remote LIBS with ultrashort pulses: characteristics in picosecond and femtosecond regimes, *J Anal At Spectrom.* 19 (2004) 437–444. <https://doi.org/10.1039/B316343A>.
- [136] S. Amoruso, G. Ausanio, A.C. Barone, R. Bruzzese, L. Gragnaniello, M. Vitiello, X. Wang, Ultrashort laser ablation of solid matter in vacuum: a comparison between the picosecond and femtosecond regimes, *Journal of Physics B: Atomic, Molecular and Optical Physics.* 38 (2005) L329. <https://doi.org/10.1088/0953-4075/38/20/L01>.
- [137] A. Hamad, L. Li, Z. Liu, A comparison of the characteristics of nanosecond, picosecond and femtosecond lasers generated Ag, TiO<sub>2</sub> and Au nanoparticles in deionised water, *Appl Phys A Mater Sci Process.* 120 (2015) 1247–1260. <https://doi.org/10.1007/S00339-015-9326-6/FIGURES/9>.
- [138] M.E. Shaheen, J.E. Gagnon, B.J. Fryer, Laser ablation of iron: A comparison between femtosecond and picosecond laser pulses, *J Appl Phys.* 114 (2013) 083110. <https://doi.org/10.1063/1.4819804>.
- [139] J. Lopez, F. Deloison, A. Lidolff, M. Delaigue, C. Hönninger, E. Mottay, Comparison of Picosecond and Femtosecond Laser Ablation for Surface Engraving of Metals and Semiconductors, *Key Eng Mater.* 496 (2012) 61–66. <https://doi.org/10.4028/WWW.SCIENTIFIC.NET/KEM.496.61>.

## List of Figures

Figure 1 - Morphological characteristics of different types of LIPSS (LSFL & HSFL) on titanium after irradiation by ultrashort laser pulses ( $\tau = 50$ fs) at 800 nm (IR) and 400 nm (UV) wavelengths [49].	7
Figure 2 - Calculated intensity distribution for (a) two-beam interference (d), (b) three-beam interference assuming symmetrical configuration (e), and (c) four-beam interference under the conditions shown in (f) [51].	8
Figure 3 - Crystallographic structure of (a) rutile and (b) anatase. Titanium atoms (white) and oxygen atoms (red) form $\text{TiO}_6$ polyhedra in the lattices [56].	9
Figure 4 - Ti-O phase diagram calculated by Cancravic et. al. [64].	10
Figure 5 - Enlargement of Figure 4 from 58 to 68 at %O.	10
Figure 6 - Schematic illustration of the general mechanism of the heterogeneous photocatalytic process.	14
Figure 7 - Photocatalytic degradation pathway of MB [101].	16
Figure 8 - a) SEM micrograph and b) X-ray emission image for Ag from the same boundary region between anatase and rutile after photoreductive deposition of Ag. The dashed line marks the boundary [110].	17
Figure 9 - Schematic structure of the Picosecond Laser generation [42].	20
Figure 10 - DLIP laser beam setup [42].	20
Figure 11 - Overlap of laser spots to achieve homogenous coverage. The total number of pulses that interact with the blue dot is defined by the spot diameter and the step sizes $\Delta x$ and $\Delta y$ [42].	21
Figure 12 - Roughness parameter used to describe the surface structured patterns.	24
Figure 13 - Experimental set up implemented for performing the methylene blue degradation [42].	25
Figure 14 - Laser spots for 1000 pulses with a pulse energy of 10 $\mu\text{J}$ for a) 10 $\mu\text{m}$ lines; b) 10 $\mu\text{m}$ points; c) 3 $\mu\text{m}$ lines and d) 3 $\mu\text{m}$ points.	28
Figure 15 - SEM images of line-like pattern samples for 100 $\text{J}/\text{cm}^2$ (above) and 1000 $\text{J}/\text{cm}^2$ (below). White bars represent a 40 $\mu\text{m}$ scale and a 10 $\mu\text{m}$ scale for the main picture and the inset, respectively.	29
Figure 16 - SEM images of L-100-700 sample with a 15000x magnification. White bar represents a 3 $\mu\text{m}$ scale.	30
Figure 17 - SEM images of cross-like pattern samples for 100 $\text{J}/\text{cm}^2$ (above) and 1000 $\text{J}/\text{cm}^2$ (below). White bars represent a 40 $\mu\text{m}$ scale and a 5 $\mu\text{m}$ scale for the main picture and the inset, respectively.	31
Figure 18 - SEM images for L-100-700 sample with three different conditions: uncleaned (left above); cleaned with ethanol (ET) without ultrasound (right above); and cleaned with ultrasound (US) in an ethanol bath (below). White bars represent a 10 $\mu\text{m}$ scale and a 2 $\mu\text{m}$ scale for the main picture and the inset, respectively.	32
Figure 19 - SEM images of the transversal area of line-like pattern samples for 100, 500, 750 and 1000 $\text{J}/\text{cm}^2$ . White bars represent a 10 $\mu\text{m}$ scale.	33
Figure 20 - Roughness parameters $R_c$ , $S_a$ and S-ratio for line-like structures with a pulse energy of 10 $\mu\text{J}$ (black) and 30 $\mu\text{J}$ (red) measured by CLSM.	35
Figure 21 - Roughness parameters $R_c$ , $S_a$ and S-ratio for cross-like structures with a pulse energy of 10 $\mu\text{J}$ (black) and 30 $\mu\text{J}$ (red) measured by CLSM.	36
Figure 22 - $C/C_0$ ratio for line-like samples (higher energy pulses).	37
Figure 23 - $C/C_0$ ratio for cross-like samples (lower energy pulses in purple and higher energy pulses in orange).	38
Figure 24 - $C/C_0$ ratio for sample L-500-1650 before and after ultrasound (US) treatment.	39
Figure 25 - XRD for line-like structures patterned with energy pulse of 30 $\mu\text{J}$ (low number of pulses per point).	40
Figure 26 - XRD for cross-like structures patterned with energy pulse of 10 and 30 $\mu\text{J}$ (high and low number of pulses per point, respectively).	42
Figure 27 - XRD for L-500-1650 samples after ultrasound (US) cleaning in ethanol (above).	43

## Appendix

### Appendix 1 – Spot diameter measurements and polynomial regression

Structure	10 $\mu\text{m}$ Lines pattern					
Power (W)	0,6	1	2	3	3,5	4
$d_1(\mu\text{m})$	81,95	94,25	108,25	114,4	115,95	120,9
$d_2(\mu\text{m})$	81,2	95,2	107,85	114,6	116,2	119,95
$d_3(\mu\text{m})$	81,2	93,85	106,75	114	115,95	118,45
$d_{ave}(\mu\text{m})$	<b>81,45</b>	<b>94,43</b>	<b>107,62</b>	<b>114,33</b>	<b>116,03</b>	<b>119,77</b>
Area (cm <sup>2</sup> )	<b>5,21.10<sup>-5</sup></b>	<b>7.10<sup>-5</sup></b>	<b>9,1.10<sup>-5</sup></b>	<b>1,04.10<sup>-4</sup></b>	<b>1,05.10<sup>-4</sup></b>	<b>1,13.10<sup>-4</sup></b>

Structure	10 $\mu\text{m}$ Points pattern					
Power (W)	0,5	1	2	3	3,5	4
$d_1(\mu\text{m})$	93	100,65	109,85	107,85	115,7	122,05
$d_2(\mu\text{m})$	93,65	100,65	108,15	108,25	117,85	119,1
$d_3(\mu\text{m})$	91,9	103,15	110,75	113,8	116,85	121,8
$d_{ave}(\mu\text{m})$	<b>92,85</b>	<b>101,48</b>	<b>109,58</b>	<b>109,97</b>	<b>116,80</b>	<b>120,98</b>
Area (cm <sup>2</sup> )	<b>6,77.10<sup>-5</sup></b>	<b>8,09.10<sup>-5</sup></b>	<b>9,43.10<sup>-5</sup></b>	<b>9,5.10<sup>-5</sup></b>	<b>1,07.10<sup>-4</sup></b>	<b>1,15.10<sup>-4</sup></b>

Structure	3 $\mu\text{m}$ Lines pattern					
Power (W)	0,5	1	2	3	3,5	4
$d_1(\mu\text{m})$	86,25	83,45	86,95	94,45	100,05	103,1
$d_2(\mu\text{m})$	86,15	82,25	84,85	96,4	103,45	102,95
$d_3(\mu\text{m})$	85,75	83,1	86,15	93,8	100,85	104
$d_{ave}(\mu\text{m})$	<b>86,05</b>	<b>82,93</b>	<b>85,98</b>	<b>94,88</b>	<b>101,45</b>	<b>103,35</b>
Area (cm <sup>2</sup> )	<b>5,82.10<sup>-5</sup></b>	<b>5,4.10<sup>-5</sup></b>	<b>5,81.10<sup>-5</sup></b>	<b>7,07.10<sup>-5</sup></b>	<b>8,08.10<sup>-5</sup></b>	<b>8,39.10<sup>-5</sup></b>

Structure	3 $\mu\text{m}$ Points pattern					
Power (W)	0,5	1	2	3	3,5	4
$d_1(\mu\text{m})$	85,7	94,85	108,7	103,75	103,1	107,65
$d_2(\mu\text{m})$	82,25	95	102,3	105,1	104,8	110,3
$d_3(\mu\text{m})$	82,6	95,85	105,35	103,95	101,95	106,6
$d_{ave}(\mu\text{m})$	<b>83,52</b>	<b>95,23</b>	<b>105,45</b>	<b>104,27</b>	<b>103,28</b>	<b>108,18</b>
Area (cm <sup>2</sup> )	<b>5,48.10<sup>-5</sup></b>	<b>7,12.10<sup>-5</sup></b>	<b>8,73.10<sup>-5</sup></b>	<b>8,54.10<sup>-5</sup></b>	<b>8,38.10<sup>-5</sup></b>	<b>9,19.10<sup>-5</sup></b>

Table A. 1 - Spot diameter measurements for lines and points patterns with 10 and 3  $\mu\text{m}$  periodicity

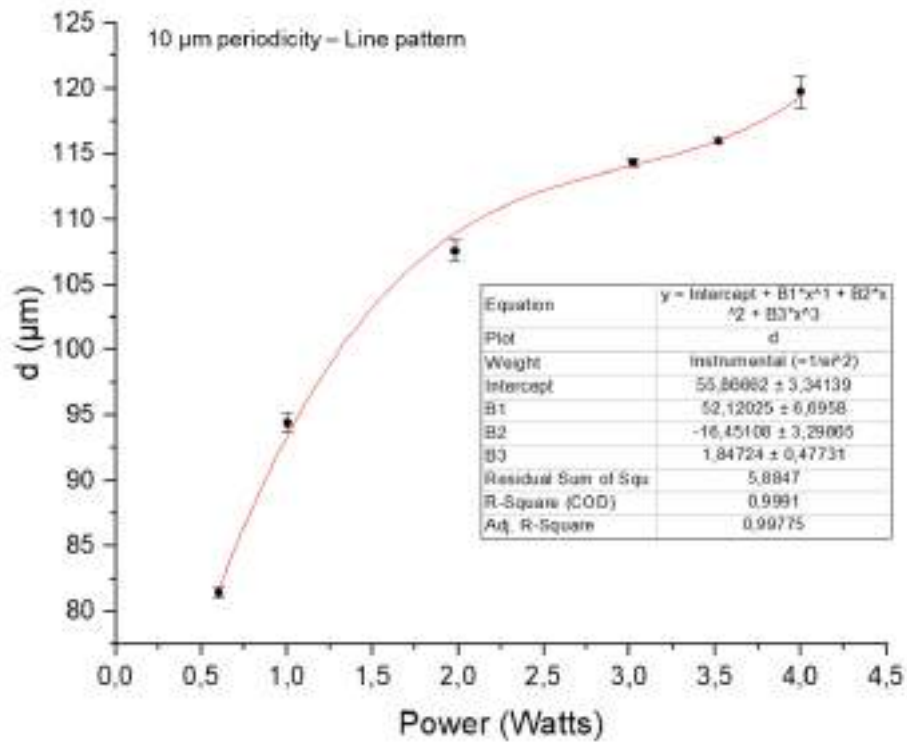


Figura A. 1 – Polynomial regression for 10  $\mu\text{m}$  periodicity line-like pattern between 0,5 and 4 Watts

## Appendix 2 – Additional XRD charts

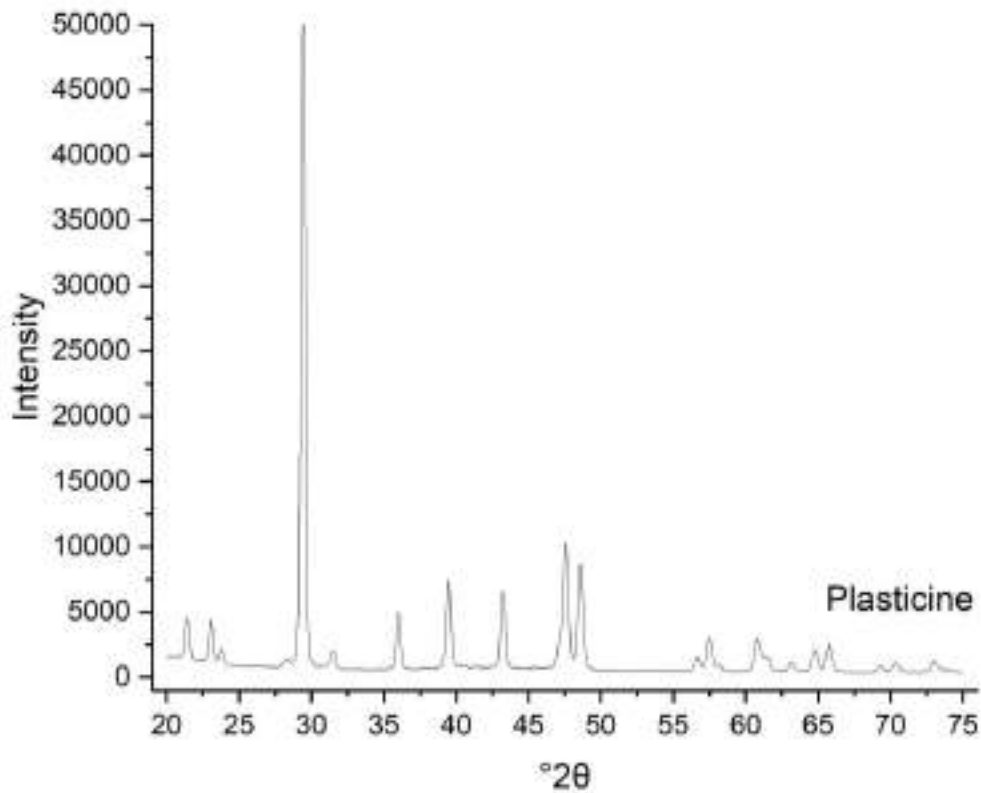


Figura A. 2 - XRD for plasticine used in cross-like samples measurements